A STUDY OF CENTRIFUGAL BUOYANCY AND PARTICULATE DEPOSITION IN A TWO PASS RIBBED DUCT FOR THE INTERNAL COOLING PASSAGES OF A TURBINE BLADE

Cody Dowd

Thesis submitted to the faculty of the Virginia Polytechnic Institute and State University in partial fulfillment of the requirements for the degree of

Master of Science

in

Mechanical Engineering

Danesh K. Tafti – Chair

Clinton L. Dancey

Francine Battaglia

April 29, 2016

Blacksburg, Virginia, USA

Keywords: Computational Fluid Dynamics (CFD), Large Eddy Simulation (LES), Turbine Heat Transfer, Coriolis Force, Centrifugal Buoyancy, Coefficient of Restitution, Particulate Transport, Particle Deposition

Scholarly Abstract

A Study of Centrifugal Buoyancy and Particulate Deposition in a Two Pass Ribbed Duct for the Internal Cooling Passages of a Turbine Blade

Cody Dowd

In this thesis, the ribbed ducts of the internal cooling passage in turbine blading are investigated to demonstrate the effects of high speed rotation. Rotation coupled with high temperature operating conditions alters the mean flow, turbulence, and heat transfer augmentation due to Coriolis and centrifugal buoyancy forces that arises from density stratification in the domain. Gas turbine engines operate in particle laden environments (sand, volcanic ash), and particulate matter ingested by the engine can make their way into the blade internal cooling passages over thousands of operating hours. These particulates can deposit on the walls of these cooling passages and degrade performance of the turbine blade. Large-Eddy Simulations (LES) with temperature dependent properties is used for turbulent flow and heat transfer in the ribbed cooling passages and Lagrangian tracking is used to calculate the particle trajectories together with a wall deposition model. The conditions used are Re=100,000, Rotation number, Ro = 0.0 and 0.2, and centrifugal Buoyancy parameters of Bo=0, 0.5, and 1.0.

First, the independent effects of Coriolis and centrifugal buoyancy forces are investigated, with a focus on the additional augmentation obtained in heat transfer with the addition of centrifugal buoyancy. Coriolis forces are known to augment heat transfer at the trailing wall and attenuate the same at the leading wall. Phenomenological arguments stated that centrifugal buoyancy augments the effects of Coriolis forces in outward flow in the first pass while opposing the effect of Coriolis forces during inward flow in the second pass. In this study, it was found that in the first pass, centrifugal buoyancy had a greater effect in augmenting heat transfer at the trailing wall than in attenuating heat transfer at the leading wall. On the contrary, it aided heat transfer in the second half of the first pass at the leading wall by energizing the flow near the wall. Also, contrary to phenomenological arguments, inclusion of centrifugal buoyancy augmented heat transfer over Coriolis forces alone on both the leading and trailing walls of the second pass.

Sand ingestion is then investigated, by injecting 200,000 particles in the size range of 0.5-175μm with 65% of the particles below 10 μm. Three duct wall temperatures are investigated, 950, 1000 and 1050 ºC with an inlet temperature of flow and particles at 527 ºC . The impingement, deposition levels, and impact characteristics are recorded as the particles move through the domain. It was found that the Coriolis force greatly increases deposition. This was made prevalent in the first pass, as 84% of the deposits in the domain occurred in the first pass for the rotating case, whereas only 27% of deposits occurred in the first pass for the stationary case with the majority of deposits occurring in the bend region. This was due to an increased interaction with the trailing wall in the rotating case whereas particles in the stationary case were allowed to remain in the mean flow and gain momentum, thus making rebounding from a wall during collision more likely than deposition. In contrast, the variation of wall temperatures caused little to no change in deposition levels. This was concluded to be a result of the high Reynolds number used in the flow. At high Reynolds numbers, the particles have a short residence times in the internal cooling circuit not allowing the flow and particles to heat up to the wall temperature. Overall, 87% of the injected particles deposited in the rotating duct whereas 58% deposited in the stationary duct.

Public Abstract

A Study of Centrifugal Buoyancy and Particulate Deposition in a Two Pass Ribbed Duct for the Internal Cooling Passages of a Turbine Blade

Cody Dowd

The gas-turbine industry is continuously evolving as the demand for increased efficiency and reduced emissions grows. This research is focused on making the turbine blading of gas-turbine engines able to operate more effectively in higher temperature applications or in particle laden environments. Specifically, the internal cooling passages of the turbine blade are investigated in this work, as these cooling passages are responsible for dissipating the high heat surrounding the blading and are critical to effective and low emission operation. This blading is also under the effects of high speed rotation which can cause different dynamics when combined with high temperature applications. It is common for gas-turbine engines to operate in particle laden environments, fine particulate matter can make its way into these internal cooling channels and degrade performance. Performance degradation occurs due to particle-wall collision effects, such as erosion, blocking of film-cooling holes and deposition.

The results of this research have shown that there are different heat transfer dynamics throughout the domain with the inclusion of rotating forces when compared to a stationary domain. In high temperature applications different rotating forces can be considered and it is shown that these additional forces have significant impact on local heat transfer. In this particular investigation it was shown that rotating forces greatly increase levels of deposition in the domain due to an increased interaction with the channel walls.

Numerical investigation is used as a tool to investigate these cooling passages to give detailed local heat transfer and flow analysis. With numerical analysis it is also possible to track the movement of individual particles throughout the domain. This research was conducted due to the experimental complexity and high cost of obtaining similar data, for either heat transfer or particle deposition results. To the authors knowledge this research is one of the first extensive numerical investigations (Large-Eddy Simulations) using complex geometry at high Reynolds number with a variable property formulation of the governing equations.

Dedicated to Mom and Dad

Acknowledgements

I would like to express my sincerest gratitude to my advisor, Dr. Danesh Tafti for his excellent guidance, patience, motivation and continuous support throughout my Masters study. For the past two years, he has provided insightful discussion and has been a great source of knowledge to me. His ability to always make himself available for questions about research is beyond appreciated. Without his guidance and persistent support, this dissertation would not have been possible.

I would also like to thank Dr. Clinton Dancey and Dr. Francine Battaglia for taking the time from their busy schedules to be on my committee and for reviewing my work.

I would also like to thank all of my colleagues in the lab throughout the past two years – Amit, Husam, Hamid, Long, Keyur, Adam, Peter, Steven, Susheel, and Dr. Kuahai Yu, who have shared their knowledge and helpful discussion about my research. I would also like to thank the support provided by the Advanced Research Computing community here at Virginia Tech.

Finally I would like to thank my family and friends, who have supported me through the struggles of graduate school. Their love and support throughout this time have made the difference.

Table of Contents

List of Figures

List of Tables

Chapter 1

Introduction

Gas turbine nozzle vanes and blades used in the aircraft propulsion and power generation are under constant development to increase performance and efficiency. To achieve higher thermal efficiency and power output, the turbine blades must operate at higher temperatures - temperatures above the range at which the blade would lose structural integrity. Therefore it is necessary to cool the vanes and blades in the high pressure stage of the turbine. A common cooling technique in modern turbines is the use of internal cooling passages within the turbine blades [1]. These cooling passages are commonly ribbed ducts to augment heat transfer. Because the cooling air is bled off from the compressed stream, it reduces the overall aerodynamic efficiency of the turbine. Therefore, accurate prediction of the heat transfer in the cooling passages is necessary to minimize the loss in aerodynamic efficiency by minimizing the bled air and at the same time keeping the turbine blade operating within acceptable temperature ranges. The flow within these cooling passages is at high Reynolds number, is highly turbulent, and experiences high rotational velocities. The rotation gives rise to additional Coriolis and centrifugal forces which modify the turbulent structure of the flow and affect heat transfer. Proper prediction of the flow within the blades is also necessary to correctly position film cooling holes and identify areas that may potentially develop hot spots in the metal temperature. If the melting temperature of the metal is exceeded, the blade can warp and reduce efficiency. As the turbine and compressor effectiveness are coupled, reduction in the extraction of work by the turbine blading can reduce the amount of work the compressor can add to the flow. This can lead to stalling of the compressor and eventual failure of the engine.

Turbine internal cooling passages are often constructed in a multiple pass configuration, meaning that the cooling fluid enters the base of the blade from the disk, is directed outwards from the axis of rotation to the tip and re-directed inward after traversing a U-bend. With rotation and centrifugal forces, the outward and inward flow exhibit different characteristics, combined with the effect of the U-bend on the flow and heat transfer. For this reason, it is necessary to investigate internal cooling geometries with multiple passes. In addition, it is difficult to experimentally measure the hydrodynamic and heat transfer

characteristics simultaneously under rotating conditions and numerical simulations offer the only viable tool for detailed simultaneous characterization of the flow and heat transfer. Numerical experiments can also separate out physical mechanisms to study them in isolation such as the effect of Coriolis forces versus combining them with centrifugal buoyancy effects.

Gas turbines often have to operate in particle laden environments, which leads to particulate ingestion and can lower efficiency or even cause failure. These particle laden environments arise when aircraft are operating in ground proximity, flying through dust/sand storms, and through volcanic clouds at high altitudes. The particles, which are on the order of 10's of microns, can lead to erosion, deposition and corrosion in different parts of the turbine exposed to the external flow. As cooling air is bled from the compressor, particulates can become entrained in the flow and enter the internal cooling circuit of blades.

Particulate impact and deposition therefore, must be considered within these cooling passages. The flow in the ribbed multi-pass flow is dominated by separated and secondary flows coupled with strong turning in the U-bend, which makes particulates more susceptible to deposition as they impinge on the walls more often. The deposition of particles in the cooling passages can lead to decreased heat transfer from the heated metal to the cooling fluid, as there is now another conductive layer for the heat to pass through. Eventually this can lead to hot spots where the blade can warp or even fail. These particulates can also clog film cooling holes and further degrade the cooling performance on the exterior of the blade.

The detailed study of particulate interaction and deposition in turbine cooling channels at high temperatures has yet to be extensively studied experimentally for small particle diameters. Experimental techniques for measurement of particulate motion and deposition levels within a rotating geometry have high levels of uncertainty. Numerical prediction, on the other hand, offers an investigation method which can better predict particle motion and model collisions to predict deposition.

The objective of the current investigation is to first investigate the independent effects that the Coriolis and centrifugal buoyancy forces will have on heat transfer prediction in a two pass ribbed duct geometry under rotating and stationary conditions at a Reynolds number of 100,000; secondly, to investigate sand impingement and deposition in the same two pass ribbed duct geometry under rotating

effects and different wall temperature conditions. Large-Eddy Simulations (LES) are used to accurately predict the complex turbulent flow field. A constant density and a variable property formulation are used to study the independent effects of the Coriolis force and centrifugal buoyancy force, respectively. To accommodate for high Reynolds number flow, turbulent wall functions are used. For the particulate investigation, the sand particles are treated in the Lagrangian frame of reference. For modeling the particle-wall collision, a two model formulation is used which takes into account the change in particle properties due to particle temperature, and a coefficient of restitution model that takes into account incoming velocity and angle. To the best of the author's knowledge, LES at Re=100,000 for a full two-pass duct has not been attempted before, nor has an investigation of particle deposition in the same geometry.

This thesis is organized as follows:

- Chapter 2: presents the governing equations with variable properties and relevant terms for fully developed flow calculations. Briefly discussed, is the framework for wall modeled LES. Nusselt number calculation methods are then discussed for constant heat flux and constant wall temperature boundary conditions. Finally, the particle equations of motion are presented.
- Chapter 3: wall modeled LES is performed on flow developing in a U-Bend rib duct at a $Re = 100{,}000$, for a stationary and rotating case with $Ro = 0.2$ and with varying centrifugal buoyancy parameters (Bo = 0.0, 0.5, 1.0). Flow characteristics and heat transfer augmentation levels are compared with the experimental work of Iacovides [2, 3]. Results demonstrate the independent effects of Coriolis and centrifugal buoyancy forces on heat transfer and hydrodynamic levels.
- Chapter 4: wall modeled LES is performed on a fully developed U-Bend rib duct at a $Re = 100{,}000$, for a stationary and rotating case with $Ro = 0.2$ and $Bo = 0.5$. Particles that are injected into the domain have their motion, impact, and deposition predictions recorded. Three different wall temperatures are investigated (950°C, 1000°C, 1050°C) for a variety of particle sizes (0.5 – 175 microns).

- Chapter 5: summarizes the thesis and gives concluding remarks
- Appendix A: Nomenclature
- Appendix B: Fully Developed Flow and Heat Transfer Validation – with particulate motion/collision results for single ribbed pitch for both stationary and rotating conditions. Reynolds number of 20,000 and rotation number of 1.0 is used. Experimental work of Rau et al. [37] is used for validation of hydrodynamic and heat transfer stationary predictions.
- Appendix C: Additional Validation of Numerical Model for Full U-Bend Geometry
- Appendix D: Additional Particle-Wall Prediction Results

Chapter 2

Numerical Methodology

All calculations are preformed using the Generalized Incompressible Direct and Large Eddy Simulation of Turbulence (GenIDLEST), an in-house source code. The code uses a finite-volume formulation with body-fitted multi-block grids on a collocated grid. The code is second-order accurate in space. For time integration, a semi-implicit method is used with an Adams-Bashforth and Crank-Nicolson time marching scheme for the convective and diffusive terms, respectively. The details of the frame work and methodology used in GenIDLEST can be found in Tafti [4]. This chapter details the relevant governing equations for both developing flow as well as the fully-developed assumption [5], the framework for wall modeled LES [6], Nusselt number calculation, and particle equation of motion [7].

2.1 Governing Equations

The governing equations used are for unsteady incompressible viscous flow with variable properties, (mass, momentum, and energy). The superscript * is used to denote dimensional variables throughout this thesis. The equations are shown with variable fluid properties and the equations are cast in non-dimensional form by using the following parametrization:

$$\rho = \frac{\rho^*}{\rho^*_{ref}} \qquad \mu = \frac{\mu^*}{\mu^*_{ref}} \qquad \kappa = \frac{\kappa^*}{\kappa^*_{ref}} \qquad c_p = \frac{c_p^*}{c_{p_{ref}}^*} \qquad \vec{x} = \frac{\vec{x}^*}{L^*_{ref}} \qquad \vec{u} = \frac{\vec{u}^*}{U^*_{ref}} \qquad t = \frac{t^* U^*_{ref}}{L^*_{ref}}$$

$$p = \frac{p^* - p^*_{ref}}{\rho^*_{ref} {U^*_{ref}}^2} \qquad \theta = \frac{T^* - T^*_{ref}}{T_0^*}$$

The reference temperature, T^*_{ref} and pressure, p^*_{ref} are used for calculating all the reference property values, and T_0^* is the non-dimensionalizing temperature scale. The dynamic viscosity and thermal conductivity variations with temperature are represented using Sutherland's law for gases [8]. The non-dimensional equations are written as:

Continuity:

$$\frac{\partial \rho}{\partial t} + \vec{\nabla} \cdot (\rho \vec{u}) = 0, \qquad \textbf{(2.1)}$$

Momentum:

$$\frac{\partial(\rho\vec{u})}{\partial t} + \vec{\nabla}\cdot(\rho\vec{u}\vec{u}) = -\vec{\nabla}p + \frac{1}{Re}\vec{\nabla}\cdot\left[(\mu+\mu_t)\left(\vec{\nabla}\vec{u} + \vec{\nabla}\vec{u}^T\right) - \frac{2}{3}\mu(\vec{\nabla}\cdot\vec{u})\vec{\boldsymbol{I}}\right] - 2\rho\overrightarrow{Ro}\times\vec{u} - \rho\overrightarrow{Ro}\times\left(\overrightarrow{Ro}\times\overrightarrow{r_1}\right) \quad \textbf{(2.2)}$$

Energy:

$$\frac{\partial(\rho\theta)}{\partial t} + \vec{\nabla}\cdot(\rho\vec{u}\theta) = \frac{1}{Re\,Pr}\vec{\nabla}\cdot(\kappa\vec{\nabla}\theta), \quad \textbf{(2.3)}$$

Equations of State:

$$\rho = \frac{\rho^*_{ref}{U^*_{ref}}^2 p + p^*_{ref}}{R^*\rho^*_{ref}\left(\theta T^*_0 + T^*_{ref}\right)}, \quad \textbf{(2.4)}$$

The non-dimensional rotation number parameter $\left(\overrightarrow{Ro}\right)$ is defined as

$$\overrightarrow{Ro} = Ro\vec{k}, \qquad Ro = \frac{\omega^*_z L^*_{ref}}{U^*_{ref}},$$

where, ω^*_z is the rotational speed (rad/s) and $\vec{k}$ is the unit vector in the z-direction. The buoyancy parameter is defined as

$$Bo = \frac{\Delta\rho^*}{\rho^*}Ro^2\left(\frac{\overrightarrow{r_1^*}}{L^*_{ref}}\right).$$

The other non-dimensional variables are defined by:

$$Re = \frac{\rho^*_{ref}U^*_{ref}L^*_{ref}}{\mu^*_{ref}}, \qquad Pr = \frac{\mu^*_{ref}{c_p}^*_{ref}}{\kappa^*_{ref}},$$

which, specify the Reynolds and Prandlt number, respectively. Included in the momentum definition, the Coriolis and centrifugal buoyancy forces are modeled as source terms in the non-inertial rotating frame of reference. In the present context $L^*_{ref} = D^*_h$ and $U^*_{ref} = U^*_{in}$ for developing flow. For application in generalized coordinates, equations (2.1-2.3) are mapped from physical coordinates $(\vec{x})$ to logical/computational coordinates $\left(\vec{\xi}\right)$ by a boundary conforming transformation $\vec{x} = \vec{x}\left(\vec{\xi}\right)$. Details of non-dimensionalization and coordinate transformation for turbulent heat transfer analysis in complex geometries is shown in Tafti [5].

2.2 Modified Equations for Fully-Developed Flow and Heat Transfer

To simplify large repetitive geometries, a periodic boundary condition can be used under a fully developed assumption in the streamwise direction, which results in considerable computational simplification. The periodic boundary condition is applied for results presented in Appendix B for validation, where constant properties are assumed. The governing equations presented in this section will represent periodic flow with Coriolis forces - no centrifugal buoyancy will be applicable due to the constant property assumption. Periodic boundary conditions balance the form and friction losses with an input mean pressure gradient. The total pressure is expressed in terms of a mean pressure gradient and a fluctuating or periodic component of pressure. This formulation was developed for steady flow by Patankar et al. [9] for both constant heat flux and constant wall temperature boundary conditions. Similar to pressure, the temperature field is similarly decomposed into a mean temperature field and fluctuating temperature. The detailed procedure can be found in Tafti [5], and the formulation is outlined here briefly.

It is first necessary to define a friction velocity $u_\tau^* = \sqrt{\tau_{w_{eq}}^* / \rho^*}$, which is used as a characteristic velocity scale to non-dimensionalize the governing equations. Assuming fully developed flow, a mean momentum balance in the streamwise direction (defined as *x* here) gives:

$$u_{ref}^* = u_\tau^* = \sqrt{\tau_{w_{eq}}^* / \rho^*} = \sqrt{(-\Delta p_x^* / L_x^*)(D_h^* / 4\rho^*)} \tag{2.5}$$

where, $\tau_{w_{eq}}^*$ is an equivalent mean wall shear stress which includes the form losses in the domain, Δp_x^* is the mean pressure drop in the streamwise direction, L_x^* is the periodic domain length in the streamwise direction, D_h^* is the hydraulic diameter, and ρ^* is the fluid density. The characteristic temperature scale which is used in non-dimensionalization is given by $T_0^* = q_w^{*"} D_h^* / \kappa^*$, where $q_w^{*"}$ is the constant heat flux per unit area applied to the wall boundaries, and D_h^* is the hydraulic diameter. Applying a periodic condition in the streamwise direction requires that the mean temperature and pressure gradients are isolated from the fluctuation periodic component as shown below:

$$P^*(\vec{x}, t) = P_{ref}^* - \beta^* x^* + p^*(\vec{x}, t) \tag{2.6}$$

$$T^*(\vec{x},t) = T^*_{ref} + \gamma x^* + \varphi^*(\vec{x},t) \quad \textbf{(2.7)}$$

where, β^* is the mean streamwise pressure gradient: $-\Delta p^*_x / L^*_x$, p^* is the periodic pressure fluctuations, γ^* is the mean streamwise temperature gradient, and φ^* is the periodic temperature fluctuation. Non-dimensionalization of Equations 2.6 and 2.7 leads to the following:

$$P(\vec{x},t) = -\beta x + p(\vec{x},t) \quad \textbf{(2.8)}$$

$$T(\vec{x},t) = \gamma x + \theta(\vec{x},t) \quad \textbf{(2.9)}$$

where $\beta = 4/D_h$and $\gamma = \Omega_s/(Re \cdot Pr \cdot Q_x \cdot L_x)$ and defining Ω_s as the non-dimensional heat transfer surface area, Q_s as the *x*-direction flow rate, and L_x is the computational domain length. Rewriting the governing equations to reflect the periodic condition, the continuity equation remains unchanged, the momentum and energy equations are represented as in index notation for simplicity with inclusion of the Coriolis term,

Momentum:

$$\frac{\partial u_i}{\partial t} + \frac{\partial (u_j u_i)}{\partial x_j} = -\frac{\partial p}{\partial x_i} + \frac{1}{Re}\left(\frac{\partial^2 u_i}{\partial x_j \partial x_j}\right) + \beta \vec{e}_x - 2\, Ro_\tau u_m \epsilon_{i3m} \quad \textbf{(2.10)}$$

Energy:

$$\frac{\partial \theta}{\partial t} + \frac{\partial (u_j \theta)}{\partial x_j} = \frac{1}{Re \cdot Pr}\left(\frac{\partial^2 \theta}{\partial x_j \partial x_j}\right) - \gamma u_x \quad \textbf{(2.11)}$$

where the $\beta\overrightarrow{e_x}$ in Equation 2.10 is the applied mean pressure gradient source term that balances out the friction and form losses in the streamwise direction. The Coriolis force is also represented in Equation 2.10 by the Ro_τ term. The $-\gamma u_x$ in Equation 2.11 is the heat sink term that balances the energy that is added to the domain by the heat flux at the walls. Without this term a periodic domain would just continuously heat up.

2.3 Turbulent Wall Modeling for LES

LES simulations are able to simulate the mean flow and model the smaller vortex structures of turbulence. By doing so it reduces computational time when compared to Direct Numerical Simulations (DNS) but not as much of a reduction in computational time as using Reynolds Averaged Navier-Stokes

(RANS) simulations. RANS simulations have difficulty in accurately predicting separated flow which makes it undesirable for ribbed geometries. LES simulation are computationally expensive when trying to predict turbulent boundary layers as the requirements for grid resolution increases greatly as Reynolds number increases. This is due to the flow becoming more energetic and significant smaller scale flow structures developing in the inner boundary layer, which become progressively smaller with increasing Reynolds number [10]. Therefore computational cost can be reduced by modeling the inner layer, when high Reynolds number flow is being simulated, the turbulent wall model utilized with GenIDLEST is shown in Patil and Tafti [6]. Details are repeated here for the zonal two layer velocity and heat transfer model.

The zonal two layer velocity model is used in the inner wall layer, applied along a normal line from the wall to the first off wall grid point ($y^+ < 50$). The wall model is formulated by solving simplified equations in the inner wall layer. Coupling between the inner and outer layer is done by using the instantaneous outer flow velocity as a boundary condition for the inner layer, which is then used to compute the wall shear stress by solving a set of reduced equations. The wall shear stress is then used as another boundary condition in the solution of the outer layer equations at the first off-wall node.

The reduced set of equations is formulated in local wall coordinates (*n*, *t*) for the inner layer. This reduced equation is used instead of solving three separate momentum equations in the inner layer for each component of the velocity. The reduction of the three separate equations involves neglecting the convective and time derivative terms, reducing the number of independent variables to one spatial normal direction (*n*). This allows the solution of a tri-diagonal system of equations at each location along the normal to the wall. This results in an effective tangent momentum transport equation, as shown below in Equation 2.12.

$$\frac{\partial}{\partial n}\left[\left(\frac{1}{Re}+\frac{1}{Re_\tau}\right)\frac{\partial u_t}{\partial n}\right] = \frac{\partial P}{\partial t} \qquad \textbf{(2.12)}$$

By the no-slip condition $u_t = 0$ at the wall and $u_t = \left|\left|\overrightarrow{U_t}\right|\right|$ at the edge of the inner layer, where $\overrightarrow{U_t}$ is the instantaneous tangential velocity at the first off wall grid point. To model the eddy viscosity in the inner layer, as detailed by Cabot and Moin [11], Equation 2.13 and the subsequent definitions are used.

$$\frac{1}{Re_\tau} = \frac{\kappa^+}{Re} d^+ \left(1 - e^{-\frac{d^+}{A}}\right)^2$$

$$d^+ = \frac{\rho u_\tau d}{\mu}$$

$$u_\tau = \sqrt{\frac{||\tau_w||}{\rho}} \qquad \textbf{(2.13)}$$

Where κ^+ is the von Karman constant, d^+ is the normal distance to the wall, and A is a constant equal to 19. The one dimensional equation is then solved iteratively (for u_τ and $\left|\left|\tau_w\right|\right|$) by using a standard tri-diagonal solver for a second-order central difference approximation. From the solution of Equation 2.13, the magnitude of the tangential wall shear stress can be predicted by,

$$\left|\left|\tau_w\right|\right| = \frac{1}{Re}\frac{\partial u_t}{\partial n}|_{wall} \qquad \textbf{(2.14)}$$

Which then can be decomposed into the respective directional components as shown below in Equation 2.15.

$$\overrightarrow{\tau_w} = \left|\left|\tau_w\right|\right|\vec{t} = \left|\left|\tau_w\right|\right|t_x\overrightarrow{e_x} + \left|\left|\tau_w\right|\right|t_y\overrightarrow{e_y} + \left|\left|\tau_w\right|\right|t_z\overrightarrow{e_z} \qquad \textbf{(2.15)}$$

Defining $\vec{t}$ as the unit tangential vector and

$$\frac{1}{Re}\frac{\partial u_i}{\partial n}|_{wall} = \left|\left|\tau_w\right|\right|t_i \qquad \textbf{(2.16)}$$

With the equations given, the stress components at the wall can now be used as boundary conditions for solving the discretized momentum equations at the first grid point normal to the wall. Substitution of the directional stress in the respective momentum equations completes the coupling between the inner and outer layers.

Details about the zonal two layer heat transfer model are now briefly discussed. An equivalent form of the reduced momentum equation in Equation 2.12 can be written for the energy equation in the inner layer,

$$\frac{\partial}{\partial n}\left[\left(1+\frac{Re\cdot Pr}{Re_t\cdot Pr_t}\right)\frac{\partial\theta}{\partial n}\right]=0 \tag{2.17}$$

To solve Equation 2.17 requires the closure model for the turbulent Prandlt number. In the current investigation, the formulation of Kays [12] is used and represented by,

$$\frac{1}{Pr_t}=0.58+0.22\left(\frac{Re}{Re_t}\right)-0.0441\left(\frac{Re}{Re_t}\right)^2\left\{1-\exp\left[-\frac{5.165}{\frac{Re}{Re_t}}\right]\right\} \tag{2.18}$$

Solution to Equation 2.17 is conducted in the inner layer in a similar method as outlined for the solution method for velocity model in Equation 2.12. The temperature at the first LES grid point off the wall and the specified wall temperature are used as boundary conditions for solving Equations 2.17. The heat flux, when not specified as a boundary condition, is obtained by

$$q_w{}''=-\frac{1}{Re\cdot Pr}\frac{d\theta}{dn}\Big|_{wall} \tag{2.19}$$

This heat flux can now be used as a boundary condition for the outer LES grid instead of using the specified wall temperature similar to the approach for the velocity model.

2.4 Nusselt Number Calculation

For heat transfer prediction the local Nusselt number must be calculated in different ways dependent on the boundary condition applied at the walls. As both constant heat flux and constant wall temperature boundary condition cases are applied in this investigation, details for calculation of Nusselt number for each respective case will be discussed here. Starting with the general energy equation at a wall,

$$q_w^*{}''=h_c^*(T_w^*-T_m^*)=-k^*\frac{dT^*}{dy^*}\Big|_{wall} \tag{2.20}$$

The subscript 'm' stands for mixed-mean and will be discussed following the calculation methods. From the definition of the non-dimensional temperature $\theta=\frac{\left(T^*-T_{ref}^*\right)}{T_0^*}$ and non-dimensionalizing by the characteristic length, D_h, substitution and simplifying results in,

$$\frac{q_w^*{}''D_h^*}{k^*T_0^*}=\frac{D_h^*h_c^*}{k^*}(\theta_w-\theta_m)=\frac{d\theta}{dy}\Big|_{wall} \tag{2.21}$$

With the non-dimensional heat transfer equation at the wall defined, the boundary condition that is applied will have its own unique Nusselt number calculation based the non-dimensional temperature. Defining first the Nusselt number relating to the constant heat flux boundary condition. The non-dimensionalizing temperature scale is defined, for a constant heat flux condition, as $T_0^* = q_w^*"D_h^*/k^*$ and defining the Nusselt number as $Nu = D_h^* h_c^*/k^*$, substituting into Equation 2.21 results in,

$$1 = Nu(\theta_w - \theta_m) = \frac{d\theta}{dy}|_{wall} \qquad \text{or} \qquad Nu = \frac{1}{\theta_w - \theta_m} \tag{2.22}$$

Now to calculating the Nusselt number for a constant temperature boundary condition, the non-dimensionalizing temperature scale is redefined as $T_0^* = T_w^* - T_{in}^*$. Substituting with previously defined characteristic length and Nusselt number results in,

$$\frac{D_h^*}{k^*}\frac{q_w^*"}{T_w^* - T_{in}^*} = q_w^" = Nu(\theta_w - \theta_m) = \frac{d\theta}{dy}|_{wall} \tag{2.23}$$

where $q_w^"$ is the non-dimensional heat flux at the wall calculated as $\frac{d\theta}{dy}|_{wall}$ and the Nusselt number is obtained from $Nu = \frac{q_w"}{\theta_w - \theta_m}$.

Under the fully-developed assumption, the mixed-mean temperature is calculated as the mass-averaged velocity over the whole periodic domain, whereas in developing flow simulations, the mixed-mean temperature is calculated at each streamwise location.

The reference value for the Nusselt number is obtained from the Dittus-Boelter correlation,

$$Nu_0 = 0.023 Re^{0.8} Pr^{0.4} \tag{2.24}$$

2.5 Particle Governing Equations

The particle motion is determined by following the trajectories of the individual particles in a Lagrangian frame of reference. A compatible Lagrangian tracking method was developed for the flow solver in GenIDLEST by Shah [7], which is capable of interfacing with a general parallel-unstructured-multiblock frame work. The verification and validation of this Lagrangian tracking method for turbulent channel flow is reported in [7, 13]. The Lagrangian frame of reference describes the position of a particle by the following set of ordinary differential equations:

$$\frac{d\overrightarrow{x_p^*}}{dt^*} = \overrightarrow{u_p^*} \tag{2.24}$$

$$m_p^* \frac{d\overrightarrow{u_p^*}}{dt^*} = \sum \overrightarrow{F_p^*} \tag{2.25}$$

Here: $\sum \overrightarrow{F_p^*} = \overrightarrow{F^*}_{drag} + \overrightarrow{F^*}_{body} + \overrightarrow{F^*}_{Cor} + \overrightarrow{F^*}_{cent} + \overrightarrow{F^*}_{lift} + \overrightarrow{F^*}_{collision} + \overrightarrow{F^*}_{brown} + \overrightarrow{F^*}_{thermo} + \overrightarrow{F^*}_{other}$

The typical forces acting on a particle, summarized as the summation in Equation 2.25, are each discussed briefly here with assumptions used. The Stokes drag force is exerted on the particle due to the relative velocity between the fluid and particle and acts in a direction opposing the relative flow. With the high density ratio between fluid and particle and range of particles considered in this thesis (0.5-175μm), the Stokes drag force is significant [14]. The body force consists of the gravitational force, which is neglected because in gas turbine applications there is no preferred direction for the action of gravity. In the current study, the Coriolis ($\overrightarrow{F^*}_{Cor}$) and centrifugal forces ($\overrightarrow{F^*}_{cent}$) are considered due to the rotation of the geometry. The Saffman lift force is caused by shear of the surrounding fluid which results in a non-uniform pressure distribution around the particle. The contribution by lift is small and is neglected in the current study, Wang et al. [15] have shown that neglecting the lift force results in a slight decrease in deposition rate.

The force due to inter-particle collision is now considered - as the simulation represents a low volume fraction of particles, the inter-particle collision and effect of particles on fluid motion and turbulence levels are neglected [16, 17]. For submicron diameter particles, the Brownian and thermophoretic forces should be included, which are a result of random molecular motion and temperature gradients, respectively. The Brownian and thermophoresis forces along with Basset, added mass, buoyancy (of particle), and force due to the acceleration of the fluid surrounding the particle can all be neglected due to their small influence in comparison to the Stokes drag force. It is also assumed that the subgrid scales have a negligible effect on the particle transport [18, 19].

All particles are represented as rigid spheres and are considered numerically as point masses located at the center of the sphere. The walls are smooth surfaces to avoid additional complexity when computing the particulate motion. Using the listed assumptions, the equations for particle motion can be written via:

$$\frac{du_i^*}{dt} = -\frac{3}{4}\frac{\rho_f^*}{\rho_p^*}\frac{C_D}{d_p^*}\left|u_i^{p*} - u_i^{f*}\right|\left(u_i^{p*} - u_i^{f*}\right) \tag{2.26}$$

The drag coefficient C_D is given by Cliff et al. [20] and is valid for particle Reynolds numbers up to 700,

$$C_D = \frac{24}{Re_p}\left(1 + 0.15Re_p^{0.687}\right) \tag{2.27}$$

where, the particle Reynolds is defined by $\left|u_i^{p*} - u_i^{f*}\right| d_p^*/\nu^*$. The continuity equation is presented in non-dimensional form and vector notation,

$$\frac{dx_i^p}{dt} = u_i^p \tag{2.28}$$

The non-dimensional particle momentum equations are written here for the x, y, and, z directions, respectively. The Coriolis and centrifugal buoyancy forces are shown as the third and fourth terms, respectively, in the x-direction momentum equation. The buoyancy is only represented in the x-direction momentum equation because the x-direction has the only significant radius (r_x).

$$\begin{aligned}
\frac{du^p}{dt} &= -\frac{1}{St_p}\left(1 + 0.15Re_p^{0.687}\right)\left(u^p - u^f\right) + 2Rov^p + Ro^2 r_x \\
\frac{dv^p}{dt} &= -\frac{1}{St_p}\left(1 + 0.15Re_p^{0.687}\right)\left(v^p - v^f\right) - 2Rou^p \\
\frac{dw^p}{dt} &= -\frac{1}{St_p}\left(1 + 0.15Re_p^{0.687}\right)\left(w^p - w^f\right)
\end{aligned} \tag{2.29}$$

where, St_p is the particle Stokes number, which is the ratio of the particle time scale λ_p^* to the flow time scale, D_h^*/u_b^*,

$$St_p = \frac{\lambda_p^*}{D_h^*/u_b^*} = \frac{\rho_p^* {d_p^*}^2/18\mu^*}{D_h^*/u_b^*} \tag{2.30}$$

The particle Stokes number gives an estimate as to how quickly a particle responds to the flow field [21]. A particle Stokes number much larger than unity implies a slow inertial response of the particle to

the surrounding flow field, while particles with Stokes number much lower than unity responds almost instantaneously to the flow field, resulting in a nearly identical particle and fluid velocity. The particle energy equation is now presented in non-dimensional form,

$$\frac{d\theta^p}{dt} = \frac{1}{St_{conv}}\left(\theta^f - \theta^p\right) + \frac{1}{St_{rad}}\left(1 - \theta^p\right) \quad \textbf{(2.31)}$$

where, St_{conv} is the particle convective thermal Stokes number defined as,

$$St_{conv} = \rho_p^* C_p^* d_p^* u_b^* / 6 h_c D_h^*. \quad \textbf{(2.32)}$$

St_{rad} is the particle radiative thermal Stokes number defined as,

$$St_{rad} = \rho_p^* C_p^* d_p^* u_b^* / 6 h_r. \quad \textbf{(2.33)}$$

The convection heat transfer coefficient, h_c, is obtained from the Ranz Marshall correlation [22] and the effective radiative heat transfer coefficient is defined as $h_r = \varepsilon\sigma(T_w^* + T^{p*})\left(T_w^{*2} + T^{p*2}\right)$. The above particle transport equations are integrated in time using the third-order Adams-Bashforth scheme to advance the particle location and temperature [7].

Chapter 3

LES Simulations of Rotating Two-Pass Ribbed Duct with Coriolis and Centrifugal Buoyancy Forces at Re = 100,000[1]

The focus of this chapter is to predict the flow and heat transfer in a rotating two-pass duct geometry with staggered ribs using Large-Eddy Simulations (LES). The geometry consists of a U-Bend with 17 ribs in each pass. The ribs are staggered with an e/D_h = 0.1 and a P/e = 10. LES is performed at a Reynolds number of 100,000, a rotation number of 0.2 and buoyancy parameters (Bo) of 0.5 and 1.0. The effects of Coriolis forces and centrifugal buoyancy are isolated and studied individually. In all cases it is found that increasing Bo from 0.5 to 1.0 at Ro=0.2 has little impact on heat transfer. It is found that in the first pass, the heat transfer is quite receptive to Coriolis forces which augment and attenuate heat transfer at the trailing and leading walls, respectively. Centrifugal buoyancy, on the other hand has a bigger effect in augmenting heat transfer at the trailing wall than in attenuating heat transfer at the leading wall. On contrary, it aids heat transfer in the second half of the first pass at the leading wall by energizing the flow near the wall. The heat transfer in the second pass is dominated by the highly turbulent flow exiting the bend. Coriolis forces have no impact on the augmentation of heat transfer on the leading wall till the second half of the passage whereas it attenuates heat transfer at the trailing wall as soon as the flow exits the bend. Contrary to phenomenological arguments, inclusion of centrifugal buoyancy augments heat transfer over Coriolis forces alone on both the leading and trailing walls of the second pass.

3.1 Introduction

Gas turbine blades operate at temperatures much higher than the melting point of the material of which they are constructed. Cooling is therefore necessary so that the blades can operate in such conditions; a common cooling technique is the use of internal cooling passages within the blades [1]. The flow within these cooling passages is at a high Reynolds number, is highly turbulent, and has effects from the high speed rotation of the blades. The rotation of the geometry gives rise to additional Coriolis and

[1] A part of this chapter is reproduced from published work in ASME Summer Heat Transfer Conference, Paper No. HT2016-7348

centrifugal forces on the fluid versus a stationary blade. The Coriolis force acts to deflect the flow towards one side of the cooling passage, due to the rotation. This apparent deflection augments and attenuates heat transfer on the trailing and leading walls for outward flow, respectively. This is demonstrated experimentally by Wagner et al. [23], where increasing rotation increases heat transfer on the trailing wall of the domain. Since the flow is operating at high temperatures, variations in the density of the fluid also come into play. This results in the centrifugal buoyancy force, which results in an additional augmentation in heat transfer along the trailing wall for outward flow. Conversely, the heat transfer is attenuated on the leading side for outward flow, due to the addition of centrifugal buoyancy forces. These trends are supported experimentally by Wagner et al. [23], when increasing the temperature difference between wall and cooling fluid resulted in additional augmentation and attenuation on the trailing and leading walls, respectively.

The current investigation is motivated by the need to accurately and effectively predict flow and heat transfer in high Reynolds number ribbed duct flows undergoing rotation. Simultaneous measurement of flow and heat transfer in rotating geometries is quite challenging and accurate prediction techniques are important to the design process.

Ribbed ducts for internal cooling have been investigated extensively over the decades. For an overview, the reader is referred to [1]. The effects of Coriolis forces on the flow and heat transfer independent of buoyancy are presented by Mayo et al. [24]. Experimentation used a small temperature difference between the wall and cooling fluid, therefore negating buoyant effects. The experimental results presented are for a rotating geometry with one wall having ribs, with a P/e of 10 and a e/D_h of 0.1. Results are presented for non-dimensional rotation numbers from 0.12-0.3 in both clockwise and counterclockwise directions, for a variation of Reynolds numbers, 15,000-40,000. Results showed, for increasing rotation, an increase in heat transfer for rotation where the ribbed wall is defined as the trailing wall. It is speculated that the secondary flow due to the rotation plays an influential role in the increase in heat transfer.

Experimental flow and heat transfer results have been presented by Iacovides et al. [2,3], respectively. The geometry was a full U-Bend geometry with staggered ribs, P/e of 10, and e/D_h of 0.1. A Reynolds number of 100,000 was used with a rotation number of 0.2. Turbulence levels and mean flow results were presented that showed increasing turbulence levels along the trailing wall as the flow advanced towards the bend. Stationary Nusselt number distributions were presented for the leading and trailing walls. The results showed higher heat transfer when investigating regions of higher turbulence, exemplified by the turning of the flow at the bend showing higher heat transfer.

Numerical prediction using techniques based on Reynolds Averaged Navier-Stokes (RANS) is a viable tool. Research using RANS simulation with a variety of turbulence models has shown varying levels of success predicting flow and heat transfer, as shown in [25-35]. Although computationally inexpensive, RANS simulations have issues with flows dominated by separation as well as secondary flows as shown in [34-35]. From the listed RANS simulations, details are presented here for those with relevant two-pass geometries.

Numerical investigation by Okita and Iacovides [31] investigates three components of internal cooling passages: rotation, rib-roughness, and curvature of bend. Results are predicted using a RANS simulation and simulating turbulence using both a high-*Re* k-ε model and high-*Re* second-moment closure model of stress transport. Both smooth and ribbed geometries ($P/e = 10, e/D_h = 0.0625$) are investigated. Reynolds numbers investigated range from 50,000 to 95,000. Agreement with experimental data is concluded to be incomplete but the second-moment closure model was in better agreement with experimental results presented.

Additionally, a numerical investigation was conducted by Sleiti and Kapat [32] for a U-Bend geometry with rounded ribs and a P/e of 10 and a e/D_h of 0.1. A Reynolds number of 25,000 was used with rotation numbers ranging from 0.24-1 and density ratios ranging from 0.13-0.3. A Reynolds stress model for turbulence is used with a RANS simulation. Results showed that the turbulence model and near wall treatment agree well with experimental results for Nusselt number predictions for varying rotation number cases.

The numerical investigation by Chen et al. [34] used a two pass geometry with 45° ribbed turbulators ($P/e = 10, e/D_h = 0.094$) to simulate the effects of heat transfer in a rotating geometry with an aspect ratio of 2:1. A RANS model was used and turbulence was modeled with a near-wall second-moment closure model. A Reynolds number of 10,000 was used for all cases with constant rotation number (0.11) and constant coolant to wall density ratio (0.115) to simulate the effects of Coriolis and centrifugal buoyancy forces on the fluid, respectively. Numerical results agree with experimental results presented and a sharp peak in Nusselt number augmentation is predicted directly before a downstream rib.

A more accurate but computationally expensive prediction comes from using Large-Eddy Simulation (LES) which is designed to capture the anisotropic energy producing turbulent scales while modeling the small scales. Tafti [36] used LES in a periodic ribbed duct geometry (P/e=10, e/D_h =0.1) to predict the flow and heat transfer and compared to the experiments of Rau et al. [37]. All the major flow features together with heat transfer augmentation characterized by primary recirculation zones and secondary flows were captured accurately by the LES.

Watanabe et al. [38] also used LES to simulate a periodic ribbed duct (P/e =10, e/D_h =0.1) at a Reynolds number of 100,000 with a uniform heat flux boundary condition on one of the ribbed walls. Time-averaged results were in good agreement with the experimental results presented. Results supported the claim that LES simulations are able to accurately resolve flow and heat transfer for complex flows.

Murata et al. [39] used LES to simulate flow and heat transfer through a two pass ribbed duct. A case study was presented for different rib orientations, P/e =10 and e/D_h =0.1 was used for all cases. Very low Reynolds numbers, on the order of 3000-5000, were used to limit computational cost. Buoyancy forces were ignored and only Coriolis forces were considered. No experimental results were presented for such low Reynolds number, so prediction accuracy of these results was not available.

Sewall and Tafti [40], conducted LES simulation of a rotating single pass ribbed ducted (6 ribs) at a Reynolds number of 20,000. Investigated were a variety of buoyancy parameters (0.00, 0.25, 0.45 and 0.65) with a constant rotation number of 0.3. Results presented were in good agreement with theoretical trends, showing augmented turbulence and heat transfer levels along the trailing wall, for outward flow, as

increasing the buoyancy parameter. Also predicted were attenuated turbulence and heat transfer levels in the vicinity of the leading wall for outward flow. Results for the leading wall also predicted a growing energetic recirculation region which caused a relative augmentation in heat transfer at downstream locations with increasing buoyancy parameter. The relative heat transfer augmentation along the leading wall is supported by recent experimental work of Coletti et al. [41].

The present study is an LES investigation in a two pass ribbed duct under stationary and rotating conditions with and without centrifugal buoyancy effects included. The study is motivated by the challenge of high Reynolds number LES in a complex geometry with complex physics and the lack of such a study in the literature. This study is also motivated by the challenges associated with simultaneous mean and turbulent flow field and heat transfer measurements to facilitate a more in depth understanding of the physics. To facilitate validation with experimental measurements, the geometry of Iacovides et al. [2,3] is simulated. To the best of our knowledge this is the first such critically evaluated study using LES at a high Reynolds number of 100,000 in a two pass duct geometry.

3.2 Methodology

The solution methodology used to solve for the complex flow and heat transfer in the internal cooling passages uses LES with a wall model to limit computational time. The governing equations are presented and cast with a variable property formulation. Details of the computational model and flow conditions are also presented.

3.2.1 Governing Equations

The turbulent flow field is simulated using a conservative finite volume code, Generalized Incompressible Direct and Large Eddy Simulations of Turbulence (GenIDLEST) [4,36]. The governing equations used are for unsteady viscous flow (mass, momentum and energy). The superscript * is used to denote dimensional values throughout the chapter. The equations are shown with variable fluid properties and the equations are cast in the non-dimensional form as shown in Chapter 2.1. A LES wall model is utilized to limit computational time and the formulation is given in Chapter 2.3.

3.2.2 Computational Model

A simplified cooling duct is considered in the present study represented as a U-shaped duct. The duct has a square cross section with staggered ribs as shown in Figure 3.1a. Figure 3.1b shows a cross sectional view of the duct with the wall classification for the leading and trailing walls, for outward flow. The classification is opposite for inward flow. All dimensions are based on the characteristic length, the hydraulic diameter of the duct (D_h^*). Each rib is square and aligned normal to the stream wise flow direction with 17 equally spaced, staggered ribs in each pass. Rib height (e^*) is $0.1D_h^*$ and pitch length (P^*) is $1D_h^*$, giving a pitch to rib height ratio (P^*/e^*) of 10 and a rib height to hydraulic diameter (e^*/D_h^*) of 0.1. These ratios are common in both experimental and numerical investigations. The first pass is $10D_h^*$ long and the second is $14D_h^*$ long with a clearance between the two passes of $0.3D_h^*$. The geometry is given a constant rotational speed (approximately 10,500 RPM) in the counter-clockwise direction around the z-axis as shown in Figure 3.1b.

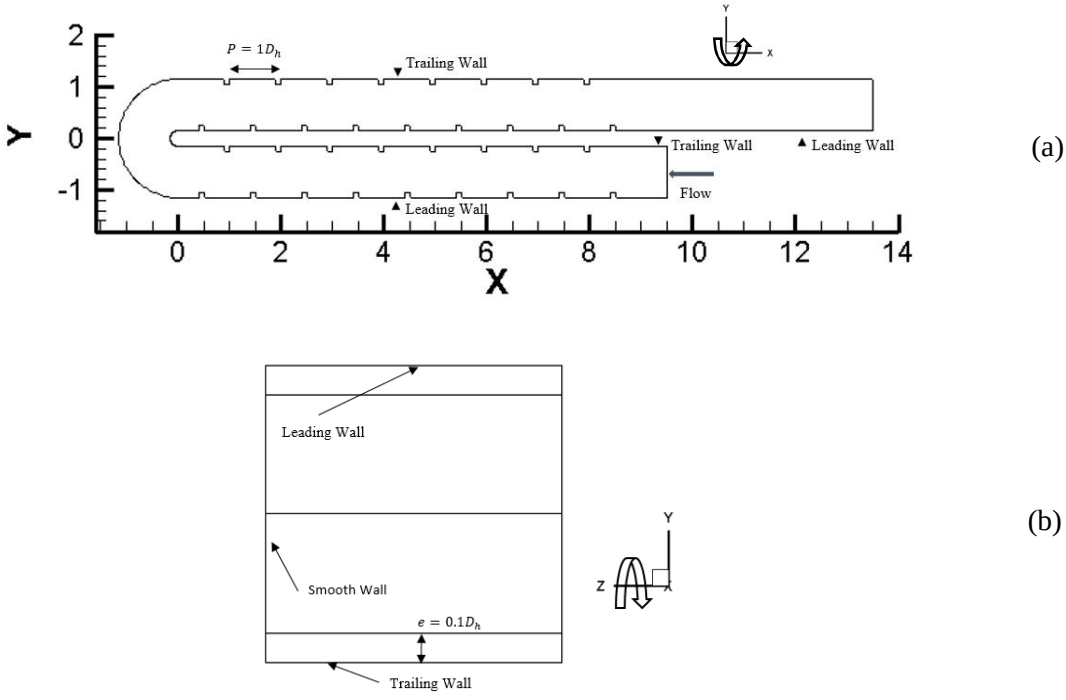

Figure 3.1. Computational domain (a) Top view of two passes (b) Cross section of domain, wall classification is for outward flow.

A representation of the mesh size is given in Figure 3.2, which presents the mesh for a representative pitch and distribution of computational cells. Figure 3.2a shows mesh for the streamwise and spanwise flow directions, and Figure 3.2b shows the mesh for the streamwise and cross duct flow directions. For reference, in the representative pitch there are approximately 800,000 total computational cells, with 108x96x80 cells in the streamwise, spanwise and cross duct flow directions, respectively.

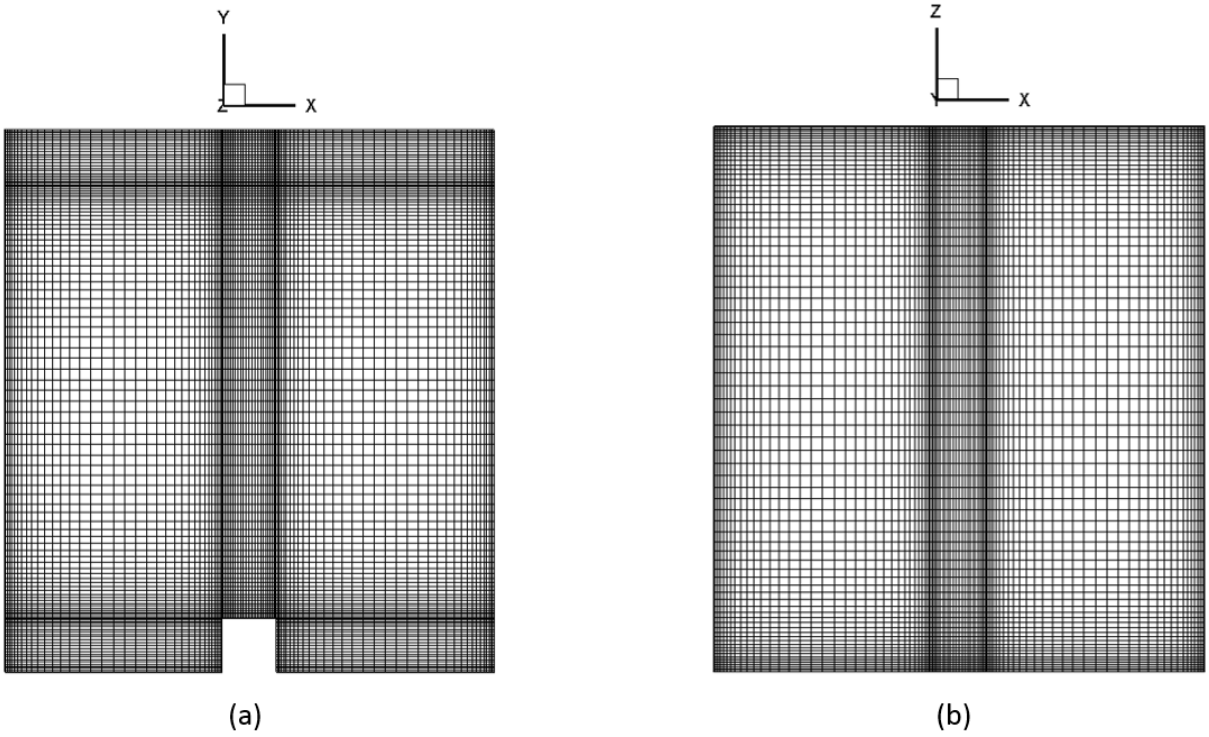

Figure 3.2. Mesh size for (a) Streamwise and spanwise flow directions and (b) Streamwise and cross duct flow directions.

3.2.3 Simulation Details

In the present work four calculations are performed on a mesh of approximately 22 million computational cells distributed over 278 blocks. A near wall spacing of approximately y^+ of 15 is used for the wall model. A Reynolds number of 100,000 is used for all cases.

The first of the four calculations is defined as a stationary case (Ro=0.0, Bo=0.0) and is presented as the base or reference case with predictions compared to the experimental measurements of Iacovides et al.

[2, 3]. The other three cases are rotating at a constant rate with a rotation number of Ro=0.2 and varying Buoyancy number/parameter (Bo=0.0, 0.5, 1.0).

At the inlet to the domain, a uniform velocity (U_{in}^*) and temperature (T_{in}^*) are specified. In the present context, $L_{ref}^* = D_h^*$, $U_{ref}^* = U_{in}^*$ and $T_{ref}^* = T_{in}^*$. Specific values used in simulation are given in Table 3.1 for reference. For constant wall temperature, $T_0^* = (T_w^* - T_{in}^*)$ and for constant heat flux boundary condition $T_0^* = \left(\frac{q_w^* D_h^*}{k_{ref}^*}\right)$. Initially the flow is allowed to develop for 10 non-dimensional time units, which is approximately one flow-through the entire domain, to establish a quasi-steady state. Time-averaged statistical quantities are obtained by sampling in time for an additional 40 non-dimensional time units or 4 flow-through times.

Table 3.1. Reference Parameters used in Simulation

Reference Parameter	Value
Inlet Velocity (U_{in}^*)	54.75 m/s
Hydraulic Diameter (D_h^*)	0.01 m
Inlet Temperature (T_{in}^*)	527 $°C$
Operating Pressure (P_{ref}^*)	15 atm
Density (ρ_{ref}^*)	6.62 kg/m^3
Viscosity (μ_{ref}^*)	3.62 x 10^{-5} kg/ms
Specific Heat ($c_{p_{ref}}^*$)	1097 J/kgK
Thermal Conductivity (k_{ref}^*)	5.68 x 10^{-2} W/mK

The local heat transfer or Nusselt number is calculated for both constant heat flux and constant wall temperature boundary conditions. The reader is directed to Chapter 2.4 for details on the calculation of Nusselt number for both boundary conditions. The reference value for the Nusselt number is obtained from the Dittus-Boelter correlation for a smooth duct,

$$Nu_0 = 0.023 Re^{0.8} Pr^{0.4} \quad \textbf{(3.1)}$$

3.2.4 Boundary Conditions

The duct inlet has a constant velocity profile normal to the boundary. A convective outflow boundary condition is used at the outlet. The duct walls, as well as all faces of the ribs that are exposed to the main

flow, have a no-slip boundary condition applied to the face. The walls are maintained at either a constant temperature or constant heat flux boundary condition.

3.3 Results and Discussion

The introduction of rotation or Coriolis forces to a stationary flow destabilizes turbulence and augments heat transfer along the trailing wall in outward flow. The Coriolis force conversely stabilizes and attenuates turbulence on the leading side. The effects are reversed for inward flow, with the leading side being augmented and the trailing side being attenuated. A second effect of the Coriolis force is the production of secondary flow in the cross section of the duct which develops strong upwash/downwash regions. Since there is now increased heat transfer on the trailing wall for radially outward flow, the fluid in the vicinity of the wall will be cooler than at the leading wall, producing a temperature gradient across the duct. This temperature difference gives rise to a density stratification across the channel with higher density fluid near the trailing wall. This density stratification combines with centrifugal forces resulting in the centrifugal buoyancy force, which results in a larger magnitude force on the fluid in the vicinity of the trailing wall than the leading wall, for radially outward flow.

For increasing buoyancy number, which is indicative of the intensity of density stratification, there will be an augmentation in heat transfer along the trailing wall for radially outward flow. For the leading wall there is an attenuation in heat transfer with lower buoyancy numbers as shown in Sewall and Tafti [40]. However, at buoyancy numbers greater than 0.5, increasing the buoyancy number augments heat transfer along the leading wall at locations further down the channel. This is due to the recirculation zone size and shear layer growing along the leading wall while remaining relatively constant in size along the trailing side of the domain. A more in-depth investigation of this phenomena will be discussed later.

A major effect of the U-Bend geometry is the augmentation of turbulence levels due to the turning of the flow in the bend. The turbulence due to the turning dominates the flow at this location causing the effects of the Coriolis force to be less apparent. For this same reason, there is no longer an apparent density stratification across the channel. Therefore, the effects of centrifugal buoyancy and Coriolis forces are not apparent until 3-4 ribs downstream of the bend for radially inward flow.

For general reference throughout the presentation of results, Figure 3.3 is used to define locations of interest and to classify the walls. As results are presented for both passes of the geometry and a stationary geometry, it is not possible to classify the walls as leading or trailing walls. Instead outer and inner sides are used and correspond to sides referenced in Figure 3.3.

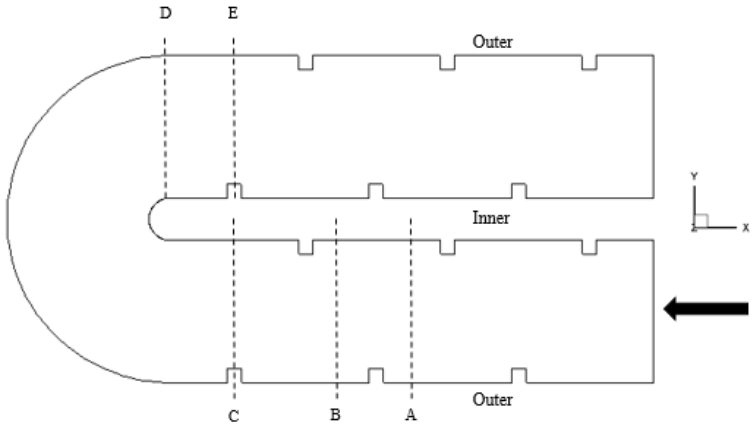

Figure 3.3. Reference locations for presentation of results.

3.3.1 Flow Field

As no experimental work is available for centrifugal buoyancy effects at this Reynolds number and geometry, the numerical model for the flow field will first be validated for the stationary and rotation results, without heat transfer, to the experimental results of Iacovides et al. [2]. Results are shown for comparison at various locations before and after the bend to demonstrate the ability of the numerical model to capture complex flow structures. Experimental results for mean flow and turbulence levels have an uncertainty < 2% of the mean velocity. Additional validation cases for stationary and rotating numerical predictions are presented in Appendix C at various channel and bend locations.

3.3.2 Stationary Mean and Turbulent Flow Validation

The stationary mean flow prediction is compared with experimental results of Iacovides et al. [2] in Figure 3.4. Results are presented across a vertical line at the center plane of the domain (Z=0.5) at locations C and E. Predictions at locations C and E agree well with the main flow structures of the mean velocity profile. There is slight over prediction near the outer wall at location C and slight under

prediction in results near the outer wall at location E. Negative velocities near the inner wall at location E are demonstrative of the recirculation zone formation downstream of the bend.

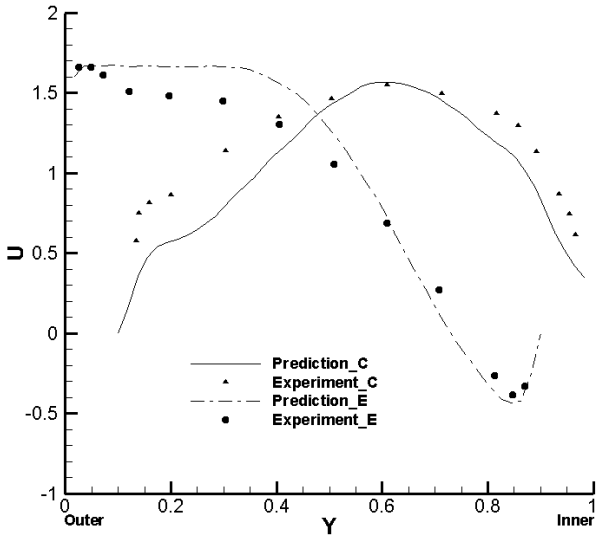

Figure 3.4. Mean streamwise velocity distribution at C and E, across duct for Ro=0.0, Bo=0.0.

Figure 3.5 examines the streamwise turbulence intensity (u_{rms}) for the stationary domain in the symmetry plane (Z=0.5) and compares those predictions to the experimental work of Iacovides et al. [2]. Two locations are again chosen, location C and E, to demonstrate the ability of the numerical model before and after the bend, respectively. Considering the high levels of turbulence and the complex flow acceleration and separation in the bend, the prediction results agree very well with experimental data for the most part with some slight differences.

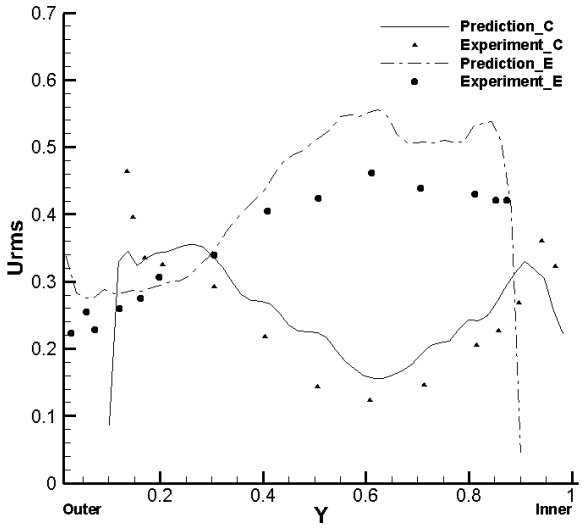

Figure 3.5. Turbulence intensity, u_{rms}, variations at locations C and E across duct height, for Ro=0.0, Bo = 0.0.

3.3.3 Rotating Mean and Turbulent Flow Field

Results in Figure 3.6 are presented across a vertical line at the center plane of domain (Z=0.5). At location C going into the bend, the mean velocity profile is distorted and fuller at the inside of the bend at the trailing side. On exiting the bend at location E, the flow is characterized by a large recirculation zone on the inside of the bend and flow acceleration on the outer side. The predicted mean velocity at C captures the asymmetric distribution but underpredicts the peak velocity. At location E, the shape of the profile is predicted with accuracy with some differences in the magnitude. A reverse flow region is present at the inner wall as the flow exits the bend.

Figure 3.6 compares the mean velocity profiles across the channel height constructed by using half profiles at locations A and B for Bo=0, 0.5 and 1.0. Since the geometry has staggered ribs, two locations need to be used to obtain a characteristic velocity profile that represents the flow. The composite profile will exhibit a slight discontinuity at the center. Locations A and B are chosen because the flow is expected to be quasi-fully developed and without a strong influence of the bend. At location A, mean flow is presented from the centerline to the inner wall and at location B, results are presented from centerline to outer wall. Again, results presented in Figure 4 are at the center plane (Z=0.5) of the domain.

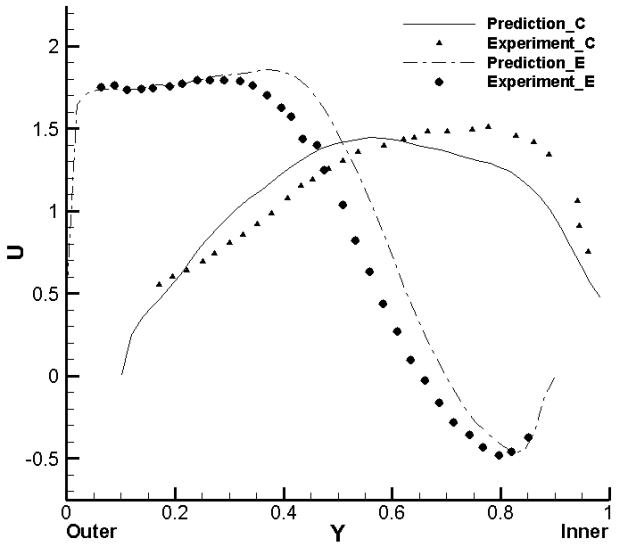

Figure 3.6. Mean streamwise flow velocity distribution at locations C and E across duct height for Ro = 0.2, Bo=0.0.

Comparing the results in Figure 3.7, the rotation case with no buoyancy effects (Bo = 0.0) predicts that the peak velocity is skewed toward the leading (outer) side, when compared to the stationary case. With the introduction of buoyancy, the peak velocity is slightly skewed toward the trailing (inner) side, which supports the expected trend that the centrifugal buoyancy forces will be larger near the trailing wall in comparison to the leading side. The leading side profiles show slight variations as Buoyancy number increases but offers no distinguishable trends. Near the trailing side, results show an increase in mean flow from Bo=0.0 to Bo=0.5 but then show a decrease with increasing Buoyancy number. The rib induced recirculation zones are characterized by the negative velocities near the walls.

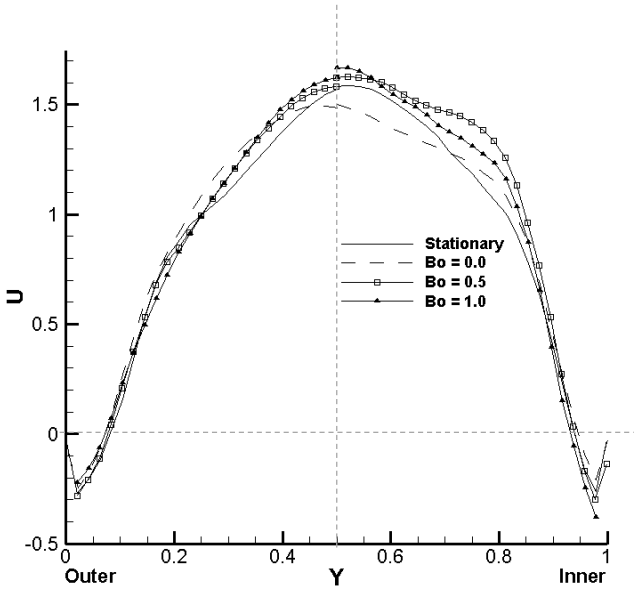

Figure 3.7. Mean rotating velocity profiles along vertical line segments at locations A and B in symmetry plane Z=0.5.

Next, validation of the numerical model for turbulent quantities is presented with comparison to Iacovides et al. [2] for Ro = 0.2, Bo=0.0. These comparisons are for Coriolis forces only as no experimental data is presented for buoyancy. Results presented in Figure 3.8 are for u_{rms} values at locations C and E. Results show good agreement with experimental values for both locations. There is some numerical over prediction near the inner wall at location C. At location E, the predicted maximum in u_{rms} is pushed towards the inner wall, which is consistent with the mean profile in Figure 3.6 It is noted that downstream of the bend, there is a large augmentation in turbulence levels.

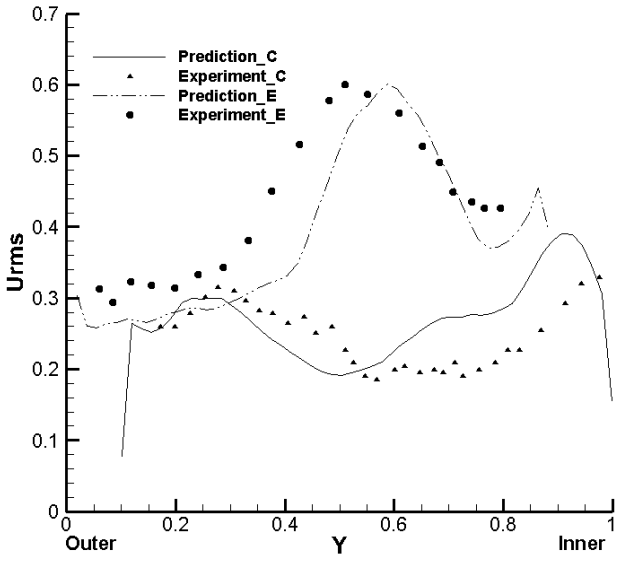

Figure 3.8. Turbulence intensity, u_{rms}, variation at locations C and E across duct height for Ro=0.2, Bo=0.0.

Results presented in Figure 3.9 are for $\overline{u'v'}$ values in the second pass at locations D and E. Results are again in reasonably good agreement considering the complexity of the flow coming out of the bend. The negative peak at location D is representative of the separated shear layer on the inside of the U-bend. At location E, the peak in $\overline{u'v'}$ is generated within the shear layer which forms on the rib at the inner wall.

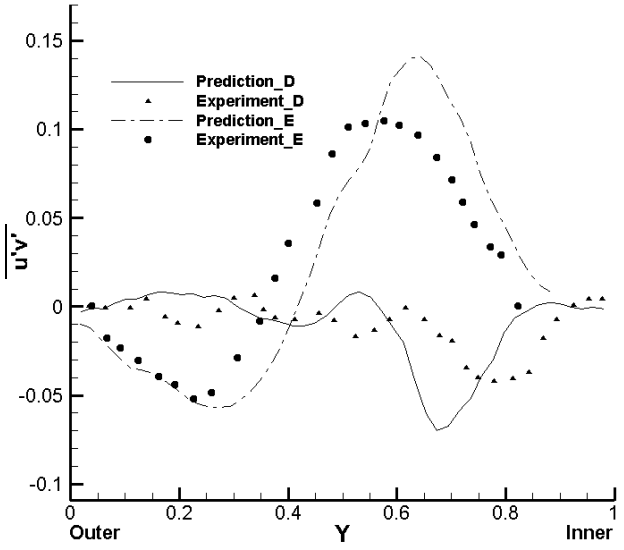

Figure 3.9. Turbulent shear stress, $\overline{u'v'}$, variation at locations D and E across duct height for Ro=0.2, Bo=0.0.

The effects of centrifugal buoyancy are more prevalent in the first pass than in the second pass. This is due to the turning of the flow which increases the turbulence levels and mixes the flow, thus making buoyancy and rotation effects less distinguishable. This is demonstrated when comparing turbulence intensity, u_{rms} levels, at a location in the first pass (location C) and in the second pass (location E), in Figures 3.10 and 3.11, respectively. Results are presented across a vertical line at the center plane of the domain (Z=0.5). The blocks on the Y axis in the figures represent the rib locations.

Results in Figure 3.10, support the claim that, in the first pass along the trailing wall, turbulence intensity is augmented with the addition of Coriolis forces (Ro=0.2, Bo=0.0). Also shown is the additional augmentation in turbulence levels at the trailing wall with the addition of centrifugal buoyancy effects (Bo=0.5 and Bo=1.0). There is a substantial increase in u_{rms} at Bo=0.5 compared to Bo=0.0, but a near asymptotic state is reached as Bo is increased further to 1.0. Conversely, turbulence is attenuated at the leading wall with rotational Coriolis forces (Bo=0.0), and remains at a constant level with the introduction of centrifugal buoyancy at Bo = 0.5. On further increase to Bo=1.0, there is an increase in u_{rms} near the leading wall. This is counter to the general expectation that increase in buoyancy will tend to attenuate turbulence at the leading wall in outward flow. On the leading side, because of the adverse effect of centrifugal buoyancy forces, the primary recirculation zone that forms in the wake of the rib increases in size and reaches a state where it extends across the whole pitch and engulfs the downstream rib. This recirculation zone gets more energetic as the flow advances into the duct and as a result there is an increase in turbulence intensity. The phenomenon is shown in Figure 3.12 which shows the flow streamlines at the center plane Z=0.5 in the first pass just before the bend region. It can be seen that as the Buoyancy parameter increases the recirculation zone between ribs gets larger and as the bend region is approached, the recirculation region engulfs the downstream rib with a demarcating shear layer which separates the core flow from the recirculating flow. Actually, this phenomenon was observed for the first time in earlier studies by Sewall and Tafti [40], and recently validated in the experiments of Coletti et al. [41]. It was shown by Sewall and Tafti [40] that the energetic recirculation on the leading side, led to an increase in the heat transfer coefficient as the flow traversed into the first pass. A similar trend is observed

in the current study. Conversely, the recirculation zone on the trailing side shrinks slightly under the effect of rotational Coriolis forces and centrifugal buoyancy effects, but the degree of shrinkage reaches an asymptotic state and does not visibly change between Bo=0.5 and 1.0.

Downstream of the bend at location E, shown in Figure 3.11, rotational Coriolis forces do not have a large impact on the magnitude of u_{rms} in the shear layer coming out of the bend. However, the action of centrifugal buoyancy has a large impact on u_{rms}. The peak u_{rms} increases from 0.6 to 0.7 at Bo=0.5 but remains fairly constant as the Buoyancy parameter increases to 1.0. At the same time, the separated shear layer tends to shift towards the outer wall (trailing side) increasing the size of the recirculation region on the inner wall coming out of the bend. This could be brought about by the increased momentum of fluid (due to centrifugal buoyancy effects) entering the bend from the trailing wall of the first pass and increased inertia as the fluid traverses the bend. The increase in the turbulence levels at Bo = 0.5 is facilitated by the high turbulence intensities near the inner wall (trailing side) as the flow in the first pass enters the bend, which gets augmented further due to strong streamline curvature and shear effects as the flow maneuvers the bend.

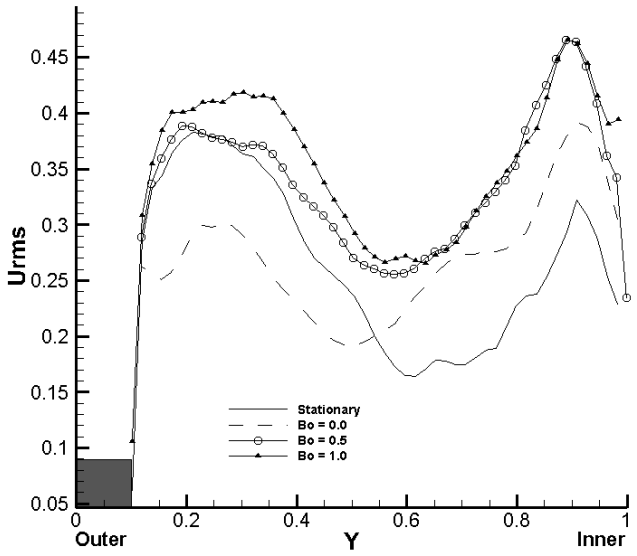

Figure 3.10. Turbulent intensity, u_{rms}, variation at location C across duct height at Z=0.5.

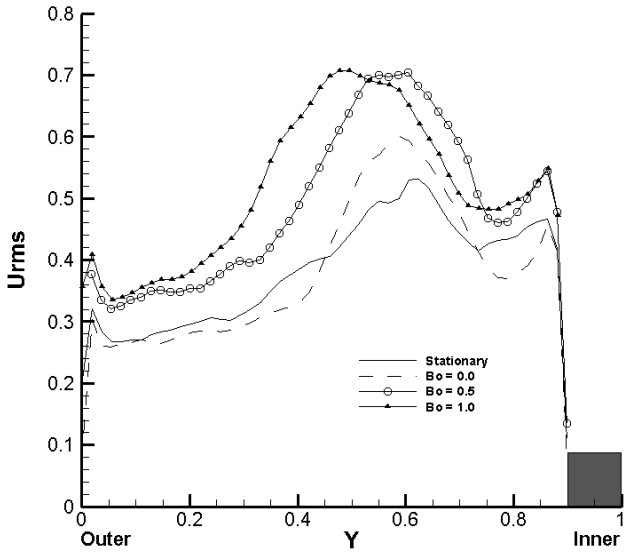

Figure 3.11. Turbulent intensity, u_{rms}, variation at location E across duct height at Z=0.5.

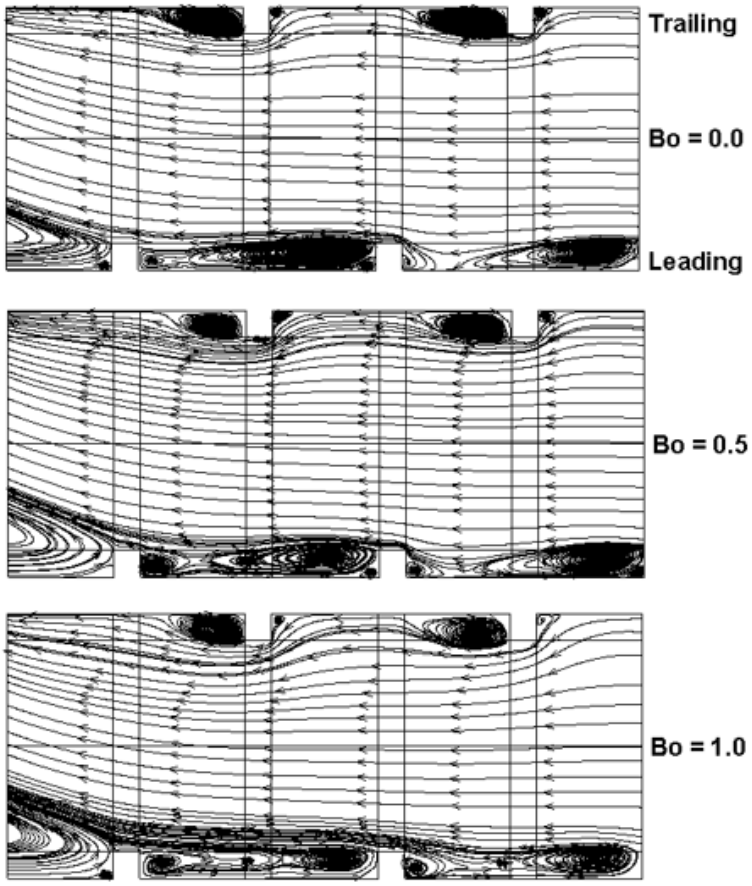

Figure 3.12. Mean flow streamline profiles showing recirculation zones for Bo = 0.0, 0.5, and 1.0, classification of trailing and leading walls is the same in all cases.

The re-energizing of the flow on the leading side of the duct with increase in Buoyancy parameter is represented more quantitatively in Figure 3.13, where the turbulent kinetic energy [TKE=$(\overline{u'^2} + \overline{v'^2} + \overline{w'^2})/2$] is shown across the height of the duct at the center plane (Z = 0.5). Results for these TKE profiles are obtained similarly as the method discussed for Figure 3.7. Because of the staggered nature of the rib placement, locations A and B are used to give a consistent representation of the variation between ribs. Since data is being taken at two locations there will be slight discontinuity at $Y = 0.5$.

Results along the trailing wall are in good agreement with the expected trend of increasing turbulence activity with an increase in Buoyancy parameter which asymptotes as the Buoyancy parameter increases beyond a certain value, which in this case of Bo=0.5. What is somewhat unexpected is the increase in TKE on the leading side of the duct with an increase in the Buoyancy parameter. While there is an expected drop in TKE on the leading side on the introduction of rotation (not shown), further introduction of centrifugal buoyancy actually increases turbulence. This trend is contrary to expectations and is explained by the dynamics shown in Figure 3.12.

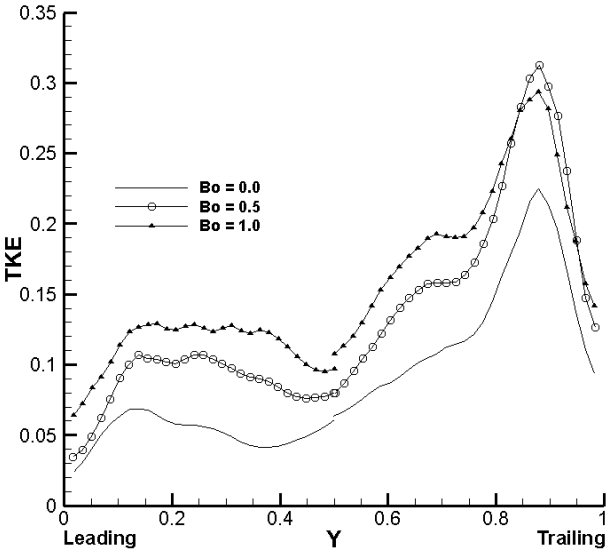

Figure 3.13. Turbulent kinetic energy profiles across duct height at locations A and B.

3.3.4 Heat Transfer Results

Results are now presented for the heat transfer distribution along the walls of the domain, represented by Nusselt number distributions. First, for validation purposes the predicted numerical results are

compared for a stationary duct (Ro=0) with the experimental results of Iacovides et al. [3]. Experimental uncertainty for side-averaged Nusselt number values is ± 5.5%.

The experiments used a constant heat flux boundary condition, so a different numerical model was used where the boundary condition was a constant heat flux boundary condition. The Nusselt number, for reference, is calculated as shown in Chapter 2.4. Whereas in the experiments, only the ribbed walls were subjected to a heat flux boundary condition, in the numerical modeling the heat flux boundary condition is applied at all surfaces. We expect these differences to be mostly compensated by the use of the mixed mean temperature in calculating the heat transfer coefficient.

For validation purposes only results along the outer and inner side of the duct (ribbed surfaces) for the first pass are presented in Figure 3.14 and 3.15, respectively. The results show side-averaged mean Nusselt number distributions. Side averaged values are obtained at each X location along the wall by averaging in the Z direction at that X location. Reference Figures 3.1 for coordinate axis and X locations.

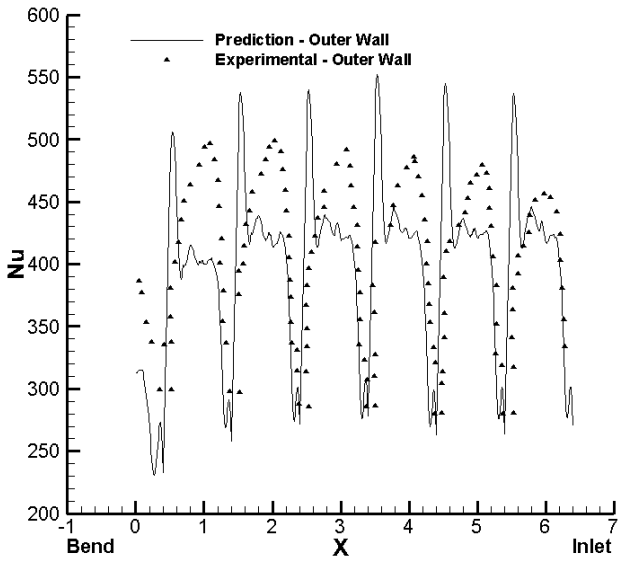

Figure 3.14. Side-averaged Nusselt number distribution along the outer ribbed wall in first pass for Ro=0.0, Bo=0.0.

The experimental and numerical predictions compare reasonably well with two main sources of disagreement. The experiments do not predict the peak in heat transfer coefficient just before the ribs, whereas the numerics underpredict the peak heat transfer that occurs between ribs near reattachment. The

former is a result of highly energetic unsteady eddies that form at the rib-wall junction and is a well-established phenomenon from previous work (Tafti [36], Watanabe [38]). These eddies constantly disrupt the thermal boundary layer and lead to large gradients and high heat transfer coefficients in the mean. The experiments in all probability do not resolve that region well enough to capture the trend. On the other hand, the underprediction of the heat transfer coefficient between ribs, could be attributed to the high Reynolds number of the flow and the inability of the LES and the wall model to capture the right levels of augmentation. It is our expectation, that increasing grid resolution would resolve this problem, as shown by the grid sensitivity analysis in Figure 3.16. We note that while the predictions indicate a pitchwise fully developed thermal state, the experiments do not, but instead show a steady increase in the heat transfer coefficient which is somewhat unusual for a stationary duct, which reaches a fully-developed state by the fourth or fifth rib pitch. Another factor which could play a role in the observed discrepancy could be the difference in the applied thermal boundary conditions between the experiments and the computations. While the experiments applied heat flux boundary conditions only at the ribbed walls, the computations had constant heat flux boundary conditions at all surfaces. It was assumed that the calculated streamwise mixed mean temperature would adequately represent these differences to make the two set of heat transfer results equivalent, but was not explicitly reproduced. Nevertheless, the predicted results are used as baselines to compare to the trends with Coriolis and centrifugal buoyancy effects.

Results in Figure 3.16 for the grid resolution analysis show there is a drastic increase in prediction accuracy with an increase mesh resolution from approximately 8 million to 22 million cells.. Results are shown for a representative rib pitch on the inner wall in the first pass. The experimental results are presented with their experimental uncertainty of ±5.5% for Nusselt number predictions. This lends credence to the expectation that an additional increase in mesh resolution would increase prediction accuracy. Further resolution was not conducted due to computational cost and because of the already good agreement with hydrodynamic experimental data on the 8 million mesh size.

Figures 3.17 and 3.18 plot the pitch averaged Nusselt number augmentation ratio distribution along the ribbed leading and trailing walls, respectively, for outward flow in the first pass. Consistent with

expectation, the Nusselt number decreases between 20-50% on the introduction of rotation (Ro=0.2). Here centrifugal buoyancy does not have a large impact on the Nusselt number. However, as the flow traverses the first pass, there is a slight recovery in the Nusselt number. This trend has been observed by Sewall and Tafti [40] also and is a result of the re-energizing of the recirculating shear layer that forms in the wake of the rib. As explained in Sewall and Tafti [40] and shown in Figure 3.12, turbulence is augmented at the leading side and the recirculating shear layer on contact with the downstream rib aids in entraining colder fluid towards the wall, which increases the Nusselt number at the wall.

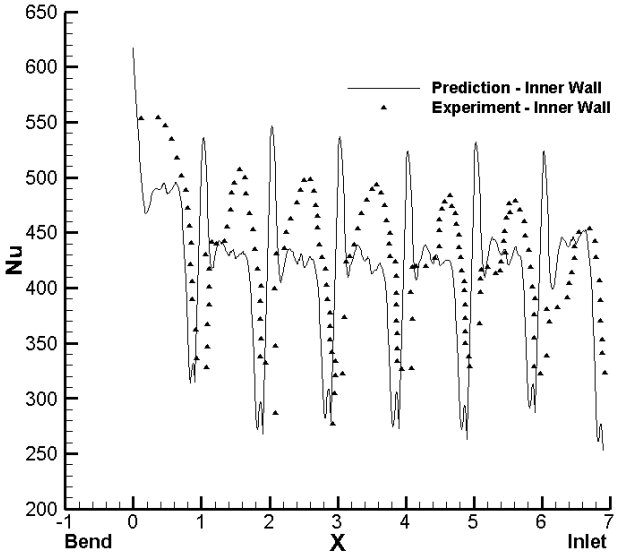

Figure 3.15. Side-averaged Nusselt number distributions along the inner ribbed wall in first pass for Ro=0.0, Bo=0.0.

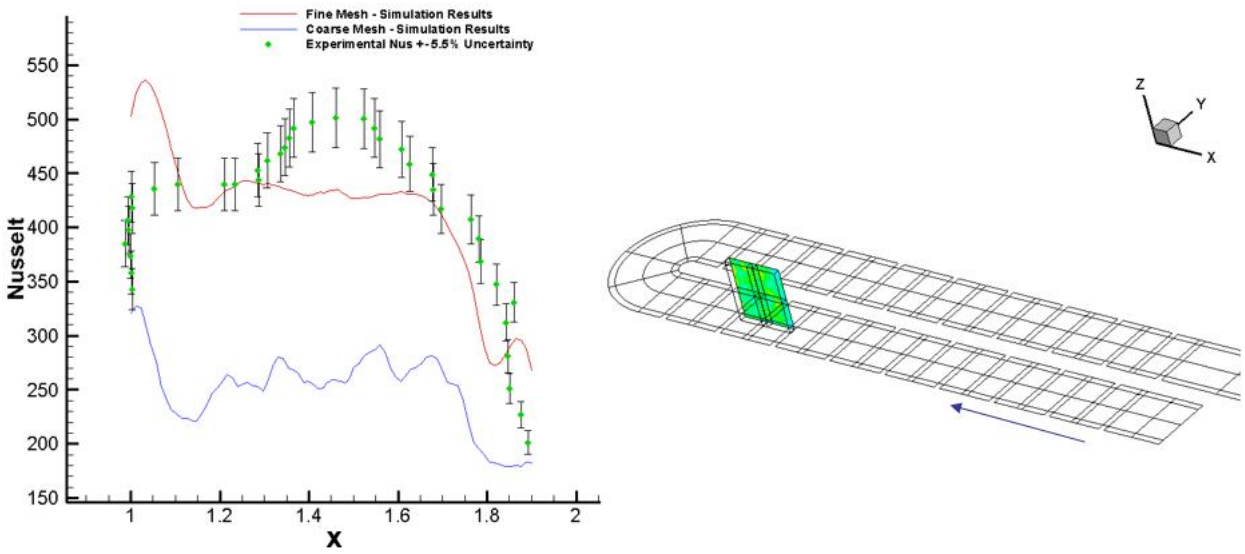

Figure 3.16. Grid sensitivity analysis for Nusselt number prediction at representative pitch on inner wall of first pass, comparison for coarse (~8 million cells) and fine (~22 million cells) mesh sizes.

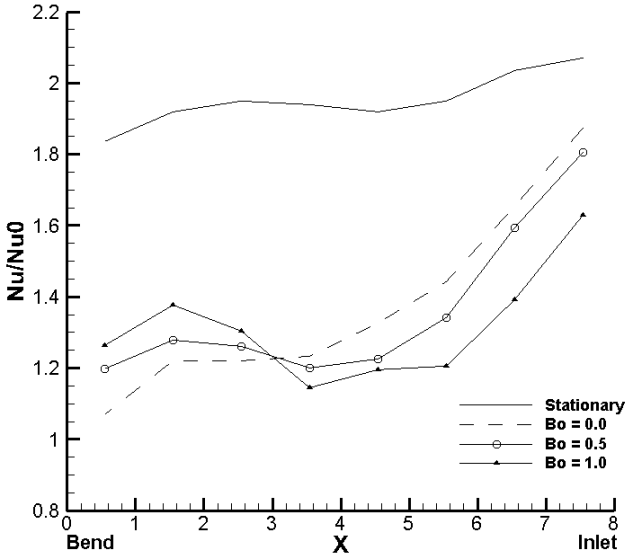

Figure 3.17. Pitch-averaged Nusselt number augmentation ratio distribution along leading wall of the first pass for Bo = 0.0, 0.5, 1.0.

In contrast to the leading wall, the heat transfer coefficient is augmented between 20-50% at the trailing wall on the introduction of rotation, which is consistent with the increase in turbulence intensity and shrinking of the rib induced recirculation zone. With the addition of centrifugal buoyancy, there is an additional augmentation in heat transfer levels. This is due to the centrifugal buoyancy adding an

additional force on the fluid and increasing the turbulence intensity along the trailing wall. Whereas, an appreciable augmentation is evident at Bo=0.5, smaller levels of additional augmentation result at the higher Buoyancy parameter. Additionally, whereas the effect of rotation and buoyancy seem to mostly saturate with X on the leading side (except for the upturn in the latter half with buoyancy), there is a monotonic increase in Nusselt number at the trailing side with no indication of the heat transfer coefficient reaching an asymptotic state. The sharp increase on the trailing side between X=1 and 0 is due to the flow accelerating at the trailing (inside) wall as the bend approaches.

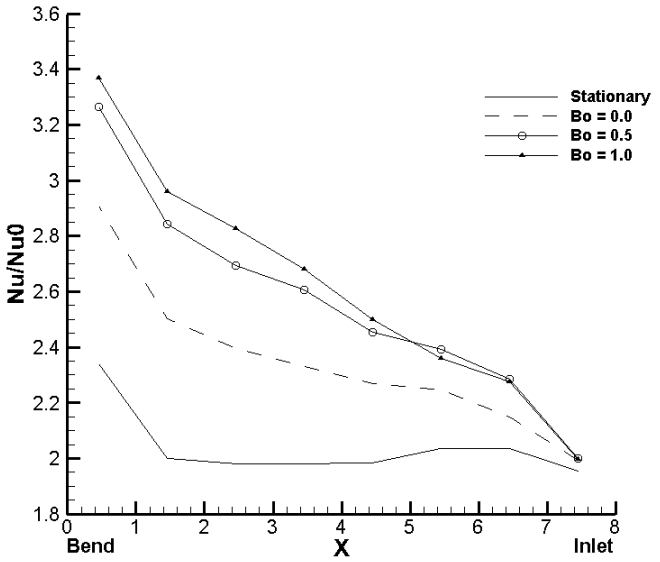

Figure 3.18. Pitch-averaged Nusselt number augmentation ratio distribution along trailing wall of the first pass for Bo =0.0, 0.5, 1.0.

Figures 3.19 and 3.20 examine the pitch averaged Nusselt number augmentation ratio distribution on the leading and trailing ribbed walls of the second pass. The Nusselt number distribution is dependent on the interplay between many different effects. First, the flow coming out of the bend is characterized by very high turbulence intensities with a recirculation zone which forms at the inner (leading) wall as the flow exits the bend. Because of the inward flow, Coriolis forces destabilize the flow at the leading wall and stabilize at the trailing wall. In addition, the centrifugal buoyancy forces now act against the flow direction and are expected to stabilize the flow on the leading side more than on the trailing side.

At the trailing (outer) wall, the augmentation in Nusselt number is high coming out of the bend followed by a steady decay as the flow progresses into the second pass. The high values are due to flow impingement as the flow comes out of the bend. Contrary to the leading wall, the stabilizing effect of Coriolis forces is evident right from the start at the trailing wall as the flow exits the bend, and is reflected by the lower augmentation compared to the stationary case. The degree of attenuation however increases further into the second pass. The action of centrifugal buoyancy augments the Nusselt number to a level midway to the stationary case. The degree of augmentation over Bo=0 is approximately the same as that experienced on the leading wall. At both walls, the flow and heat transfer have not reached a fully-developed state at the exit of the second pass.

At the leading (inner wall), the Nusselt number is low initially due to the presence of a recirculation zone. As the flow attaches, there is an increase in the Nusselt number in all cases. For the stationary duct, there is a monotonic decrease at the leading inner wall as the turbulence levels decay, but the Nusselt number does not reach a steady asymptotic value before it exits the duct and is still decreasing. The action of rotational Coriolis forces to destabilize the flow on the leading wall is only evident in the latter half of the second pass during which the destabilizing action of Coriolis forces maintains a higher value than the stationary case. The introduction of centrifugal buoyancy effects augments the overall level of Nusselt number because of the intense turbulent flow that exits the bend region. However, there are no distinguishing trends which would point to the selective action of centrifugal buoyancy in the second pass. Except in the early part of the second pass, there is no difference in augmentation between the two buoyancy parameters.

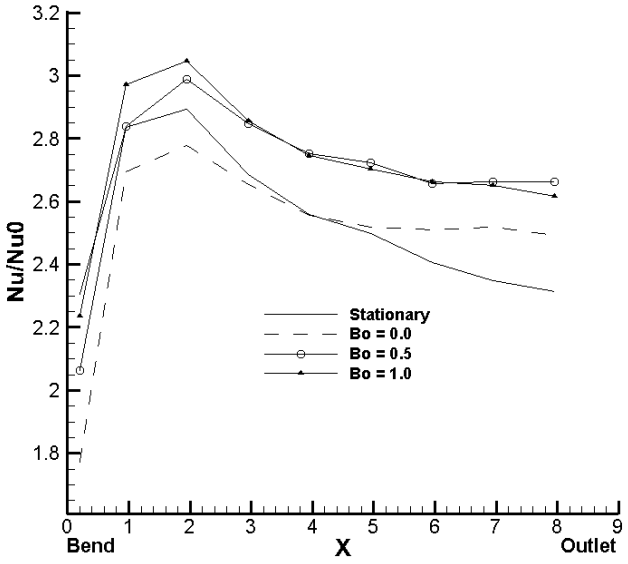

Figure 3.19. Pitch-averaged Nusselt number augmentation ratio distribution along leading wall of the second pass for Bo = 0.0, 0.5, 1.0.

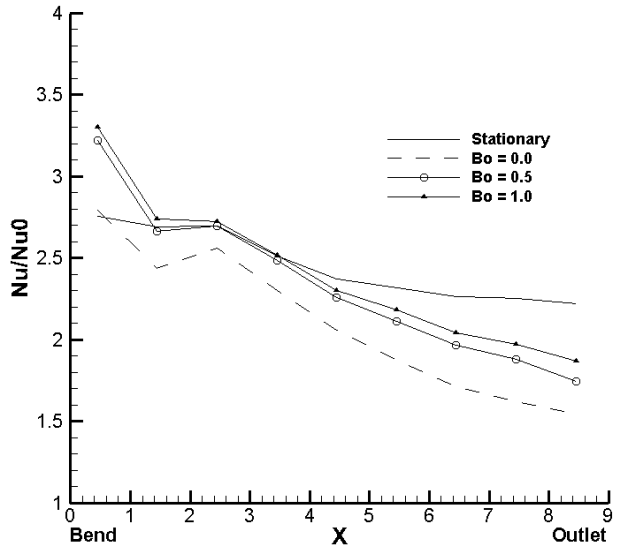

Figure 3.20. Pitch-averaged Nusselt number augmentation ratio distribution along trailing wall of the second pass for Bo = 0.0, 0.5, 1.0.

3.4 Conclusions

Large-Eddy Simulations with a wall model are conducted in a two-pass ribbed duct at Re=100,000 under stationary and rotating conditions at Ro=0.2. The effect of Coriolis forces on flow and heat transfer and centrifugal buoyancy effects are investigated independently for Bo=0.0, 0.5 and 1.0. Mean flow and

turbulent quantities are validated against available experiments and show very good agreement with measured profiles.

In the first pass or outward flow, Coriolis forces augment heat transfer on the trailing side, and attenuate heat transfer on the leading side between 20-50%. Centrifugal buoyancy, on the other hand has a stronger impact on the trailing side over and above the augmentation provided by rotational Coriolis forces than on the leading side. On the leading side, centrifugal buoyancy has a minimal effect on further attenuating heat transfer. Instead it has the effect of staging a slight recovery in heat transfer augmentation in the downstream half of the duct by energizing the rib separated shear layer and increasing turbulence intensities in the vicinity of the leading wall.

In the second pass, rotation has a larger impact on the trailing side at which heat transfer is attenuated by the effect of Coriolis forces than on the leading side at which heat transfer is only augmented in the second half of the pass. Buoyancy on the other hand has the effect of augmenting heat transfer (over Coriolis force effects) both at the leading and trailing sides, which is contrary to the phenomenological understanding of centrifugal buoyancy effects in inward flow. However, we note that compared to a stationary duct, Coriolis and centrifugal buoyancy combine to augment heat transfer on the leading side and attenuate heat transfer on the trailing side in the second pass.

Chapter 4

Sand Transport and Deposition in Rotating Two-Pass Ribbed Duct with Coriolis and Centrifugal Buoyancy Forces at Re=100,000

The focus of this chapter is to simulate the transport of 0.5-175μm diameter sand particles in the two-pass internal cooling duct of a turbine blade under high speed rotation. The geometry consists of a U-bend with 17 ribs in each pass. The ribs are staggered with an e/D_h = 0.1 and a P/e = 10. The flow field and heat transfer are identical to Chapter 3, with Coriolis and centrifugal buoyancy forces acting on the carrier and dispersed phase. LES simulation is used with a Reynolds number, Re=100,000, a Buoyancy parameter, Bo=0.5, and a rotation number, Ro=0.2. The sand particles are tracked in a Lagrangian framework. These sand particles will impinge on the surfaces and, under favorable conditions, deposit. To model these collisions and to determine deposition, a two model formulation is used. This formulation takes into account the temperature effects and the velocity/angle at which the particle impinges on the wall. These two factors play the greatest role in determining whether the impacting particle will deposit or not. Deposition and impingement patterns for the particle size range of 0.5-175μm are investigated for three different wall temperatures, 950, 1000, and 1050°C under rotating and stationary conditions. The effects of rotation gives rise to increased impingement and therefore deposition throughout the domain, especially in the first pass of the domain. There is a slight increase in deposition with increasing wall temperature but not as high as expected. This is due to the high Reynolds number of the flow leading to short residence times in the internal cooling circuit not allowing the particles to heat up to the wall temperature. Coriolis forces play an important role in increasing deposition and impingement levels in the two-pass ribbed, internal cooling duct.

4.1 Introduction

Gas turbines often operate in particle laden environments, which lead to particle ingestion into the engine and eventually into the internal cooling passages of turbine blading, by means of being entrained in the cooling air bled from the compressor. These particles can impinge on the surfaces of the cooling passages which lead to erosive effects and/or deposition of the particulate matter on the surface. The flow in a rotating two-pass ribbed duct is dominated by separated and secondary flow which makes particles

mores susceptible to deposition as they impinge on the walls more often. Deposition on surfaces can lead to attenuated heat transfer from the heated metal to the cooling fluid, as there is now another conductive layer for the heat to pass through. Eventually this can lead to hot spots where the blade can warp or even fail. These particulates can also clog film cooling holes and further degrade the cooling performance on the exterior of the blade.

The current investigation is motivated by the need to accurately predict particle transport and particle-wall interaction in high Reynolds number ribbed duct flows undergoing rotation. The detailed study of particulate interaction and deposition in turbine cooling channels at high temperatures has yet to be extensively studied experimentally for small particle diameters. Controlled laboratory based experimental measurement of particulate motion and deposition within a rotating, high temperature geometry are extremely difficult. Numerical prediction, on the other hand, offers an investigation method which can predict particle transport and model collisions to predict deposition.

Different aspects of the problem of particulate ingestion have been studied previously in canonical geometries. A majority of the work focuses on deposition and impact of particles under a variety of operating conditions. To determine the operating conditions that are critical when modeling particle-wall interaction, the means of energy loss in particle-wall interaction are investigated. A brief review is given here that shows the major energy losses during impact. Tabakoff and Sugiyama [42] have used laser Doppler velocimetry (LDV) to study the particle-surface interaction and have shown that the impact angle primarily affects the restitution ratio. The independent effects of sand particle size, number of particles, and surface temperatures on particle deposition was studied by Walsh et al. [43]. It was shown that the temperature of the metal was a critical parameter in deposition levels. A temperature threshold (above 1000°C) for sand deposition was presented.

Experimental investigation conducted by the group of Crosby, Bons, and Fletcher [44-47], presented results for particulate deposition, where the particulates were composed of ash from various synfuels used in land based gas turbine applications. Crosby et al. [44] have conducted experimental deposition tests to determine the effect of particle size, gas temperature, and contact surface temperature, independently. The

experimental setup consisted of particulate entrained flow contacting a coupon angled at 45 degrees. The particle sizes investigated ranged from 3-16 microns and showed increasing deposition with increasing particle diameter. The investigation also showed that with larger diameter, the particles were more likely to contact the coupon and not deviate with the flow. The gas temperature investigation used particles of 3 micron diameter for a temperature range from 860 to 1183°C. Results showed an exponential increase in deposition with an increase in gas temperature, giving rise to a threshold for deposition of 960°C. Finally, cooling of the coupon caused a decrease in deposition of impacting particles.

Additionally, experimental work by Delimont, Ng, and Ekkad [48, 49] presented coefficient of restitution and deposition results for micro-particles under high temperature conditions. Delimont et al. [49] investigated particulate impingement on a coupon and presented a coefficient of restitution calculation method for a variation of impacting angles (30-80°) and surface temperatures (1073-1323 K). A constant impact velocity of 70 m/s was used and particle sizes ranged from 20-30 microns for sand particles impacting a stainless steel coupon. Results presented showed similar deposition results for all impacting angles investigated and that as the temperature increased the deposition increased exponentially. With an increase in impacting angle there was a decrease in the normal restitution coefficient, which was observed for all temperatures tested.

Experimentally tracking the individual particle motion, impingement, and deposition levels within a rotating geometry has yet to be studied. Numerical investigation provides a viable option in prediction of particulate motion, impingement and deposition for ribbed duct geometries undergoing rotation under high temperature conditions. To accomplish this, the development of a dispersed two phase flow solver was conducted by Shah [7]. The capabilities of this two-phase flow solver is demonstrated by Shah and Tafti [13] for a periodic in-line ribbed duct geometry. This investigation demonstrated the secondary flow effects of ribbed flow on the transport of particulates. LES simulations using a Reynolds number of 20,000, a rotation number of 0.35, a P/e of 10 and a e/D_h of 0.1 to represent the geometry. The dynamics of the particulates were investigated but no heat transfer or deposition was investigated. Two different particulate sizes were investigated, 10 micron and 50 micron. The investigation showed that the larger particles (50

micron) collect in the near wall region in greater number and concentration than the smaller particles (10 micron) at the end of the simulation.

A composition dependent deposition model was developed by Sreedharan and Tafti [50], this model was compatible with the two phase flow solver developed by Shah [7]. The model numerically used the physical dependence of the viscosity on temperature of a particle and determined how this affected deposition probability when a particle came into contact with a wall. The capabilities of the model were demonstrated by simulations with particulate laden flow contacting a coupon surface angled at 45°. Sreedharan and Tafti applied this deposition model to leading edge film cooling for particle sizes of 5 and 7 microns over a range of blowing ratios (0.5-2) [51]. LES was used with Syngas ash particles of 5 and 10 microns modeled as discrete particles. Simulation showed that Syngas samples with lower softening temperatures experienced higher levels of deposition. A blowing ratio of 1.5 experienced the lowest capture efficiency for all particle sizes and compositions investigated.

At the same time as the deposition model was developed by Sreedharan and Tafti [50], another research group conducted deposition related numerical investigations, Ai and Fletcher [52] presented results for coupon impingement and deposition. This was made possible by the development of a numerical deposition model. The model investigated here used El-Batsh and Haselbacher [53] deposition model as a basis and implemented a capture or critical velocity model. At impact speeds below the capture velocity, the particle would deposit and above the capture velocity it rebounded off the wall. The capture velocity model was developed by semi-empirical relations from experimental data for specific particle compositions and sizes. Simulation was preformed to demonstrate the effectiveness of the model. Simulation used a particle entrained flow contacting a coupon at 30 degrees. A steady RANS simulation with a k-ω turbulence model was used for the fluid domain. A Lagrangian approach was used for particulate motion. The average particle size used in simulation was 13.4 micron and results for various gas temperatures (1300-1450K) showed exponentially increasing deposition with increasing gas temperature. Results also supported that larger particles do not deviate from the mean flow and therefore were more likely to contact the coupon. The

larger particle sizes predicted almost no deposition while for the smaller particle size, prediction showed that the particle would deposit almost every time they impinged on a surface.

Singh and Tafti developed a coefficient of restitution (COR) deposition model [54]. The model took into account incoming angle and velocity to determine a deposition probability due to loss of kinetic energy. The COR model considered both elastic and elastic-plastic deformation losses during collision. The COR model was combined with the viscosity model of Sreedharan and Tafti [50] to predict deposition [55]. Singh and Tafti [56] validated the effectiveness of the combined deposition model in LES simulations in a stationary two pass geometry, with 16 inline ribs in the first pass and 14 inline ribs in the second pass. A Reynolds number of 25,000 was used with a constant wall temperature boundary condition on all surfaces exposed to mean flow and the ribs were constructed with a P/e of 9.28 and a e/D_h of 0.0625. Used in this investigation were particulate sizes ranging from 0.5-25 microns and 3 different wall temperatures (950, 1000, 1050°C). A particle softening temperature of 1120°C was used, which represents the temperature above which a particle would stick to a wall regardless of velocity or angle. Results showed increased deposition with increasing wall temperatures. This investigation also showed higher deposition in the second pass than in the first due to higher turbulence levels and mixing from turning of the flow. Also shown, the smaller particles had a higher probability of depositing when contacting the wall at low velocities as they had lower incoming kinetic energy. Finally, secondary flow due to flow interaction with the ribs caused particulate impacts on the side walls but resulted in low levels of deposition on the smooth side walls of the channel.

4.2 Methodology

The solution methodology used to solve for the complex carrier phase and heat transfer in the internal cooling passages uses LES with a wall model to limit computational time. The governing equations are discussed briefly for the carrier phase with a variable property formulation and for the dispersed phase. Details of the two model formulation for particulate deposition and simulation details/boundary conditions are also briefly presented. The computational model is the same as presented in Chapter 3.

4.2.1 Carrier Phase

The turbulent flow field is simulated using a conservative finite volume code, Generalized Incompressible Direct and Large Eddy Simulations of Turbulence (GenIDLEST) [4,36]. The superscript * is used to denote dimensional values throughout the chapter. The equations are shown with variable fluid properties and the equations are cast in the non-dimensional form as shown in Chapter 2.1. A LES wall model is utilized to limit computational time and the formulation is given in Chapter 2.3.

4.2.2 Dispersed Phase

The particle transport is solved using a Lagrangian framework developed and integrated into GenIDLEST by Shah [7]. The governing equations for particle motion take into account drag and rotational forces acting on the particle. The rotational forces, Coriolis and centrifugal buoyancy, are implemented similarly as done in the fluid domain. For the energy equation treatment of the particles, convection and radiative effects between the dispersed phase and carrier fluid and surroundings are taken into account. The reader is referred to Chapter 2.5 for reference to the particle governing equations and their casting in the non-dimensional form. The particles used in the simulations are representative of sand and have a diameter range of 0.5-175μm which corresponds to particle Stokes numbers (St_p) ranging from 0.006-676, respectively. The size range is representative of Fine Arizona Road Test Dust from Powder Technology Inc., with a mean diameter of 9μm (St_p=1.79) and standard deviation of 4μm. This corresponds to 50% of injected particles being less than 4μm in diameter, with 90% being less than 50μm, shown in Figure 4.1b. Figure 4.1a shows the cumulative size distribution of injected particulates and Figure 4.2 shows the actual number of particles injected per size group out of a total of 200,000 particles.

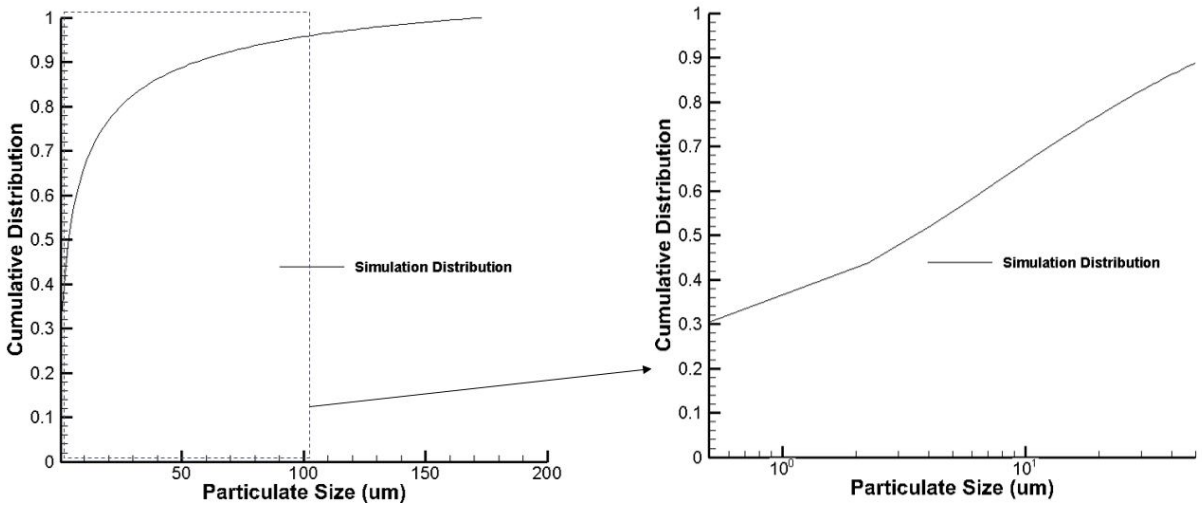

Figure 4.1. Size distribution (a) Overall cumulative distribution (b) Cumulative distribution on a log scale to give focus to the majority of particulate sizes.

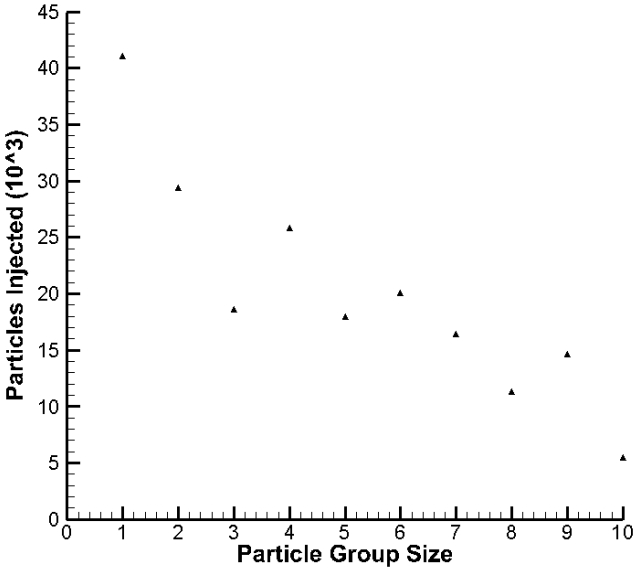

Group	Size Range
1	0.5 - 3µm
2	3 - 5µm
3	5 - 10µm
4	10 - 20µm
5	20 - 30µm
6	30 - 50µm
7	50 - 75µm
8	75 - 100µm
9	100 - 150µm
10	> 150µm

Figure 4.2 Size distribution of particles injected by particle size groups, with size group definitions.

4.2.3 Deposition Model Formulation

As the particles used in simulation are represented as rigid spheres and are considered as point masses located at the center of the sphere, a model must be used to determine the particle-wall interaction. The deposition model considers the kinetic energy lost during collision and the effect of temperature. To account for the temperature effects a critical viscosity model is used, developed and integrated with GenIDLEST

by Sreedharan and Tafti [50]. To account for the kinetic energy losses during collision, the COR model is used, developed by Singh and Tafti [54], using an improved coefficient of restitution prediction model developed by Yu and Tafti [57], which considers elastic, elastic-plastic, and plastic losses, surface adhesion, and size dependent property variation of sand. These two models are combined to form a final sticking probability. Details for the two models will briefly be repeated here.

4.2.3.1 Critical Viscosity Deposition Model

The model by Sreedharan and Tafti [50] predicts the deposition probability of a particle based on the particle composition and the particle temperature during an impact. The predictions [50] showed good agreement with the measurements over a range of temperatures for ash and PVC particles. This model assumes that the sticking probability increases with decrease in viscosity of the particle, or as the temperature increases. Above the critical temperature or the softening temperature (assumed to be $T^*_{soft} = 1120°C$), the viscosity rapidly decreases and below this critical viscosity (μ^*_{cr}), the sticking probability is assumed to be unity. Below the softening temperature a sticking probability is calculated from:

$$P_{visc} = \frac{\mu^*_{cr}}{\mu^*_T}, \quad \mu^*_{cr} = \mu^*_{soft} \tag{4.1}$$

where μ^*_T is the viscosity of the particle at the particle temperature. Sand composition is varied and the composition can change with type and source of sand, to properly handle this, a model was developed by Senior and Srinivaschar [58] that is used to compute the sand viscosity as a function of temperature. Viscosity of sand particles is calculated from the particle temperature from the following:

$$\log\left(\frac{\mu^*}{T^*}\right) = A + \frac{10^3 B}{T^*} \tag{4.2}$$

where the constants A and B are calculated from the sand composition [58]. The softening temperature of the sand can then be calculate based on this sand composition from the empirical relation proposed by Yin et al. [59]. As this critical viscosity model was initially developed for coal ash particles and it is a composition based model, it is assumed that it can be used for sand particles since the composition is comparable as shown in [54]. Based on the composition, the softening temperature should lie in the range of 1000°C-1200°C. For all calculations discussed here, a softening temperature of 1120°C is chosen.

Particle temperatures much lower than the softening temperature are less likely to deposit. This trend is demonstrated in Figure 4.3 which shows the probability of sticking for sand particles (P_{visc}) with temperature of the particle. As shown sticking probability rises exponentially as approaching the softening temperature. Any collision temperature above 1120°C will have a sticking probability of 1. Any deposition much below this temperature is due to energy losses due to deformation and adhesion losses, as discussed in the following section.

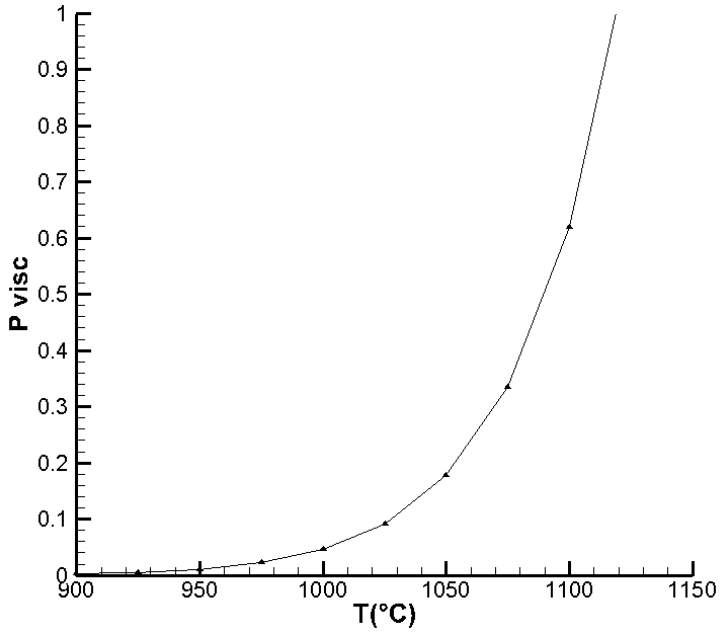

Figure 4.3. Probability of deposition based on the viscosity (P_{visc}) with temperature.

4.2.3.2 Coefficient of Restitution Deposition Model

With the deposition probability calculated that takes into account the temperature variations of the particle as it contacts the surface, the effects of impacting velocity and angle are now taken into consideration. This model, developed by Singh and Tafti [54], assumes the probability of deposition is a function of the fraction of the kinetic energy lost by the particle during impact. The coefficient of restitution (COR) is the ratio of the rebound velocity to the impact velocity and is a parameter that contains all of the energy losses incurred by the particles during a collision. The additional model to predict the COR for sand particles based on deformation and adhesion losses during collision was developed by Yu and Tafti [57]. This COR model has been validated with experimental COR data for various particle sizes and

compositions. This COR model takes into account elastic, elastic-plastic, and plastic impact deformation losses. The model determines adhesive losses during the recovery stage, with Van der Waal's forces and dissipative Hertzman contact forces acting against the particle rebounding from the wall. The impact and adhesive losses are assumed to act independently. Also taken into consideration are the sensitivity of the mechanical properties (Young's modulus and yield stress) of sand to the size of the particle. As the particle/wall mechanical properties are important in determining deposition from the COR criteria, Table 4.1 is given with the relevant properties for the surface and particle. Bulk values are given for Young's modulus and yield stress. The Poisson's ratio for sand was approximated based on the composition of major components of sand, given in [50].

Table 4.1 Relevant mechanical properties for particles (Sand) and walls (Steel) used for simulation.

Particle (Sand)	
Density (kg/m^3)	2630
Specific Heat (J/kg/K)	730
Thermal Conductivity (W/m/K)	1.5
Bulk Young's Modulus (GPa)	190
Bulk Yield Stress (MPa)	1000
Poisson's Ratio	0.162
Wall (Steel)	
Density (kg/m^3)	8050
Young's Modulus (GPa)	210
Poisson's Ratio	0.27
Yield Stress (MPa)	250

Representative normal COR results for a variety of particle sizes and incoming velocities are presented for normal collisions in Figure 4.4. Also presented are representative tangential COR predictions in Figure 4.5, results are shown for a 5μm particle for various incoming angles and velocities. Only one particle size was used as the predictions were similar for all particle sizes. The predictions in Figure 4.4 show discontinuities in the COR results for the 50 and 100 micron particle sizes are representative of when the particle enters into the plastic regime from the elastic-plastic regime. Overall it should be noted that the model by Yu and Tafti [57], predicts that on average, over half of the incoming energy is lost in collision.

The predictions in Figure 4.5 show that for shallow incoming angles the tangential COR prediction will be near unity and the tangential COR decreases as the collision angle increases approaching a normal collision. The COR predictions are used in the model of Singh and Tafti [54] to calculate a sticking probability.

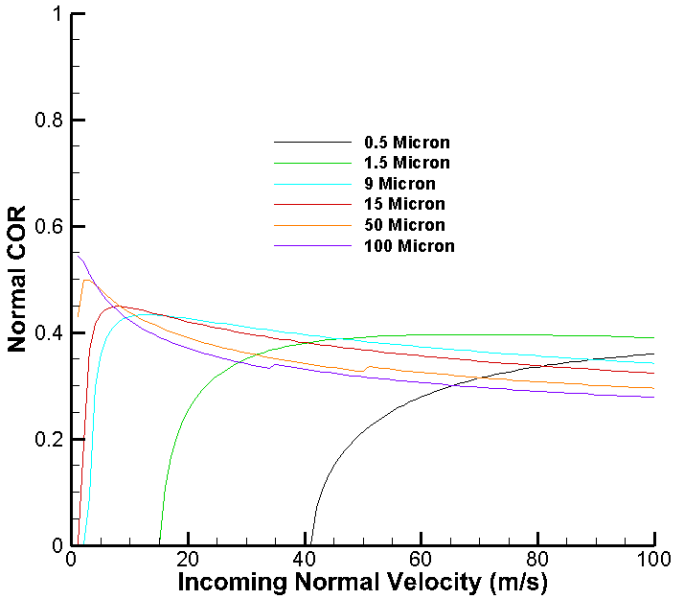

Figure 4.4. Normal coefficient of restitution (COR) prediction for various incoming velocities and particles sizes.

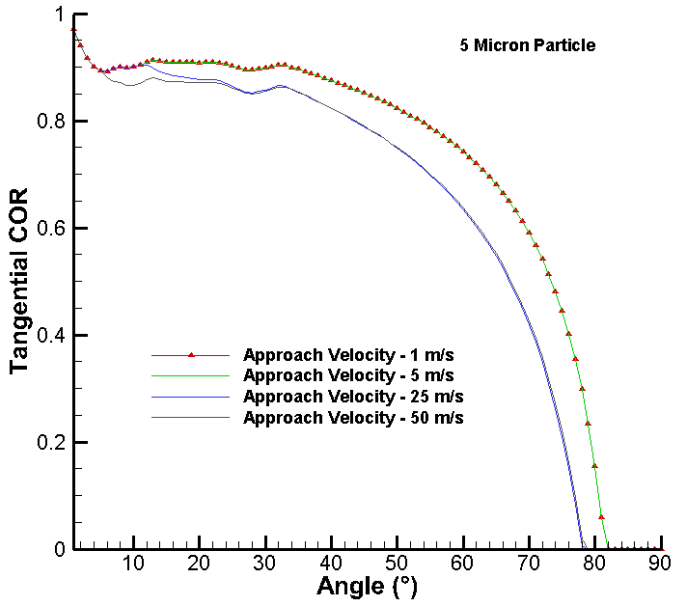

Figure 4.5 Tangential coefficient of restitution (COR) prediction for a 5μm particle with various incoming angles and velocities.

The probability of sticking should be a function of energy losses during a collision and is calculated from coefficient of restitution model as $P_{COR} = f(COR)$. An exponential function was chosen such that the sticking probability based on COR, becomes significant only when the particle loses more than half the initial kinetic energy during impact. Starting with,

$$P_{COR} = \exp(-c * COR) \quad \textbf{(4.3)}$$

$$\text{If } P_{COR} = 0.0 \text{ for } 1 - COR^2 \leq 0.5 \text{ i.e } COR \geq 0.707 \quad \textbf{(4.4)}$$

$$\text{Resulting in } c \approx 6.5 \Rightarrow P_{COR} = 0.01 \text{ for } COR = 0.707 \quad \textbf{(4.5)}$$

The variation in the probability of deposition due to the COR is given in Figure 4.6 when the exponential function is used.

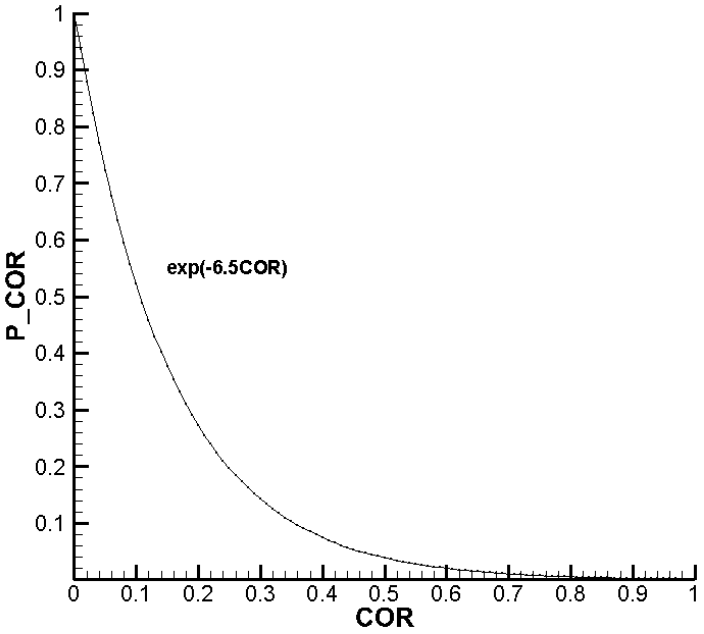

Figure 4.6. Probability of deposition based on incoming velocity (P_{COR}) with COR.

The current model emphasizes that both the mechanisms, the change in physical properties with temperature and collision losses, should be accounted for in the final deposition probability. The final deposition probability is calculated based on the two deposition probabilities previously discussed,

$$P_{dep} = \min\{P_{COR} + P_{visc}, 1\} \quad \textbf{(4.6)}$$

Equation 4.6 demonstrates how the conditions at which a particle collides will have either one of the two mechanisms dominate the deposition prediction or both mechanisms can combine to determine the

deposition prediction. This accounts for low temperature particles depositing if there collision losses are high and vice-versa.

This deposition probability (P_{dep}) is then compared with a random number, determined by a uniform random number generator, which generates a number between 0 and 1. If the random number is less than the deposition probability calculated, the particle is assume to deposit. If the particle does not deposit, it rebounds with the velocity calculated from the coefficient of restitution model. The above discussed deposition model is used in the following simulations to model sand particle laden flow within a U-Bend ribbed duct geometry.

4.2.4 Boundary Conditions and Simulation Details

The duct inlet has a constant velocity profile normal to the boundary. A convective outflow boundary condition is used at the outlet. The duct walls, as well as all the faces of the ribs exposed to the main flow, have a no-slip boundary condition. The walls are maintained at a constant temperature boundary condition. For a constant wall temperature the non-dimensionalizing temperature scales (T_0^*) is given as $T_0^* = (T_w^* - T_{in}^*)$. At the inlet to the domain, a uniform velocity (U_{in}^*) and temperature (T_{in}^*) are specified. In the present context, $L_{ref}^* = D_h^*$, $U_{ref}^* = U_{in}^*$ and $T_{ref}^* = T_{in}^*$. Reference values for inlet conditions are similar as given in Table 3.1. Initially the flow is allowed to develop for 10 non-dimensional time units, which is approximately one flow-through of the entire domain, to establish a quasi-steady (stationary) state. Time-averaged statistical quantities are obtained by sampling in time for an additional 40 non-dimensional time units or 4 flow-through times. The reader is directed to Chapter 2.4 for details on the calculation of Nusselt number for the constant wall temperature boundary condition.

In the present chapter four calculations are performed on a similar mesh as presented in Chapter 3. A Reynolds number of 100,000 is used for all cases. The first simulation (referred to as Case 1) is at a constant wall temperature of 1050°C and is stationary, Ro=0.0. The next three calculations are rotating at a constant rate with a rotation number of Ro=0.2 with constant Buoyancy number of Bo=0.5. The constant wall temperature is varied for the final three cases, (950°C, 1000°C, and 1050°C), referred to as Cases 2, 3, and

4, respectively. The final simulation is stationary (Case 5) with a constant wall temperature of 950°C. As the temperature difference between the wall and mean fluid is changing but a constant Buoyancy number is desired, the dimensional radius ($\overline{r_1}^*$) between the inlet of the duct and the axis of rotation is modified with changing wall temperature.

Randomly distributed particles are injected at the inlet with 10,000 particles per injection for 20 injections, overall 200,000 particles are allowed to flow through the domain. Initially upon injection, the particle velocities and temperatures are set to be the same as the surrounding fluid. The particles are tracked and the calculation is run for one additional flow-through of the domain after the last injection of particles. Particle-wall collision and deposition statistics are recorded during the run.

4.3 Results and Discussion

As the flow field and temperature field have been discussed in Chapter 3, only the particle transport and deposition levels will be discussed in the current chapter. Detailed particle impingement and deposition discussion for various surfaces are presented, followed by average impact characteristics presented with the effects of each particle size group on the impact characteristics.

4.3.1 Impact and Deposition Characteristics

The impingement and deposition contour plots are presented here for the surfaces within the ribbed duct. Results are presented for a wall temperature of 1050°C, for the stationary and the rotating conditions (Case 1 and 4, respectively). Results that are presented in all figures are normalized by the non-dimensional cell area. For dimensional values, the contour levels presented must be multiplied by 10^{-10} which gives results in the number of deposits or impacts/mm^2. For reference to the coordinate system and wall labeling, the reader is referred to Figure 4.7. The geometry is given a constant rotational speed (approximately 10,500 RPM) in the counterclockwise direction around the z-axis.

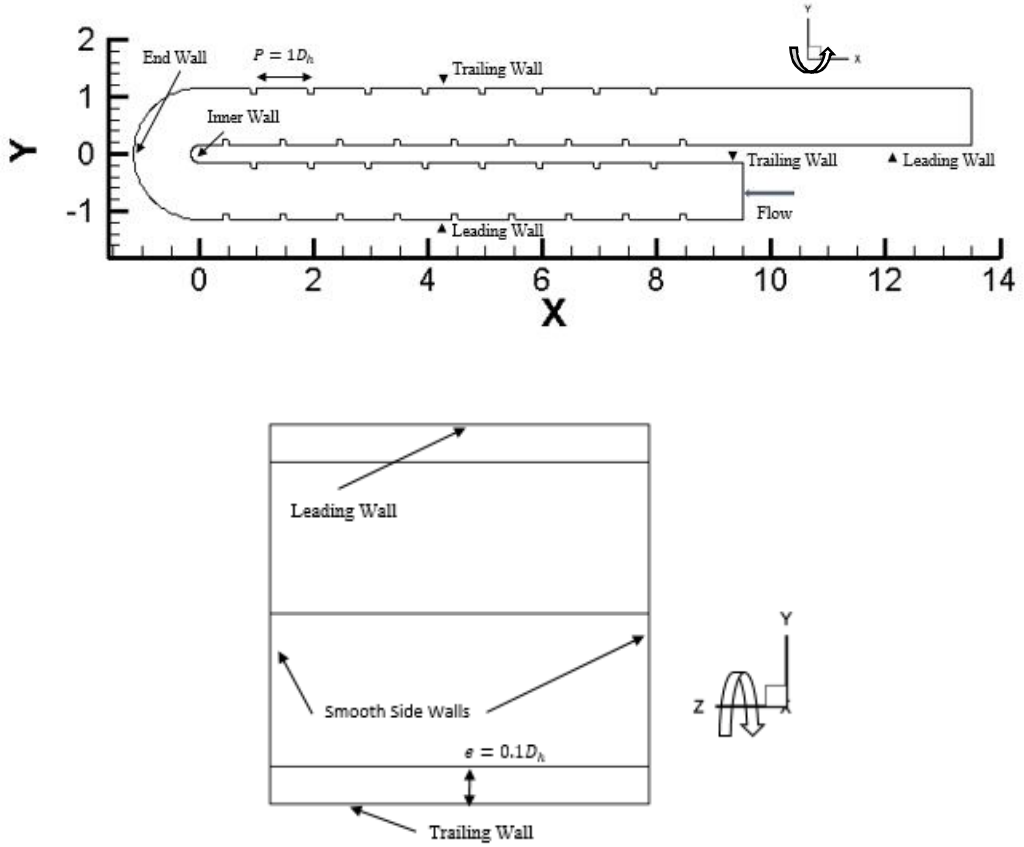

Figure 4.7. Computational domain (a) Top view of two passes (b) Cross section of domain, wall classification is for outward flow in the first pass.

With the addition of Coriolis and centrifugal forces, the particle impingement patterns will be drastically different on the leading and trailing ribbed walls, which are critical components in augmenting heat transfer levels in the cooling passages of a turbine blade. In-depth investigation of ribbed walls is necessary as high deposition levels could lead to heat transfer attenuation. Results presented in Figure 4.8 and 4.9 are impingement and deposition levels normalized by the computational cell area, on the leading and trailing walls of the 1st and 2nd pass, for Cases 1 and 4, respectively. As the impingement and deposition levels are similar in all the rotation cases, representative results are presented using the highest temperature rotating case compared to the stationary geometry. Results for Cases 2, 3 and 5 are presented in Appendix D for all of the following impact and deposition results. Arrows in the figures represent the flow direction.

The results in Figure 4.8 show impingement and deposition patterns on the leading and trailing sides (ribbed surfaces) in both the first and second passes of the stationary geometry. In the first pass both ribbed surfaces exhibit similar impact and deposition patterns, except at the entrance because of the staggered nature of the ribs. High impingement and deposition levels are calculated along the trailing wall when the flow exits the U-Bend into the second pass. As the flow is turned by the bend, particle entrained flow will contact the end wall of the bend in order to navigate the turn, shown as high levels of impingement and deposition at the exit of the bend on the trailing wall. Because of the flow disturbance created by the bend, more impacts and deposition are found on the leading wall in the second pass.

Results in Figure 4.9 show high levels of impingement and subsequent deposition along the trailing wall in the first pass. As the particles and flow have additional Coriolis and centrifugal forces acting on their motion, when the particles are placed in the flow, they are immediately directed towards the trailing wall. As a result very high levels of impact and deposition occur on the trailing ribbed surface at the entrance where the particles are immediately directed towards the trailing wall. Because of the large number of particles that impact the surface, some of these particles deposit on the surface. The many that do not deposit, continue their trajectory close to the trailing wall constantly impacting the surface at shallow angles but relatively high velocities because of Coriolis acceleration. As will be shown later, because of the large number of impacts with the trailing wall in the first pass, the probability based deposition model predicts that a substantial percentage of the particles deposit on the trailing wall in the first pass, particularly in the first three pitches. In the second pass, the particles on exiting the bend impinge and deposit on the trailing wall, but are quickly re-directed to the leading wall by the effect of Coriolis forces, resulting in more impacts and deposition on the leading wall. However, because of the large percentage of particles that deposit in the first pass when the duct is rotating, the predicted levels of particle impacts and deposition on the trailing wall directly downstream of the bend is much less than the stationary case.

Particle size also plays a role on impact and deposition on the first pass trailing wall. More of the larger diameter particles are pushed towards the trailing wall because of the larger Coriolis forces acting on them. These particles undergo many impacts as they travel along the trailing wall and most of them end up

depositing on the ribbed surface. This will be demonstrated in a following figure, Figure 4.18. The smaller, lighter particles tend not to be strongly affected by the Coriolis forces and tend not to deposit in the first pass as well as the second pass of the duct. This will be discussed in greater detail in the following sections.

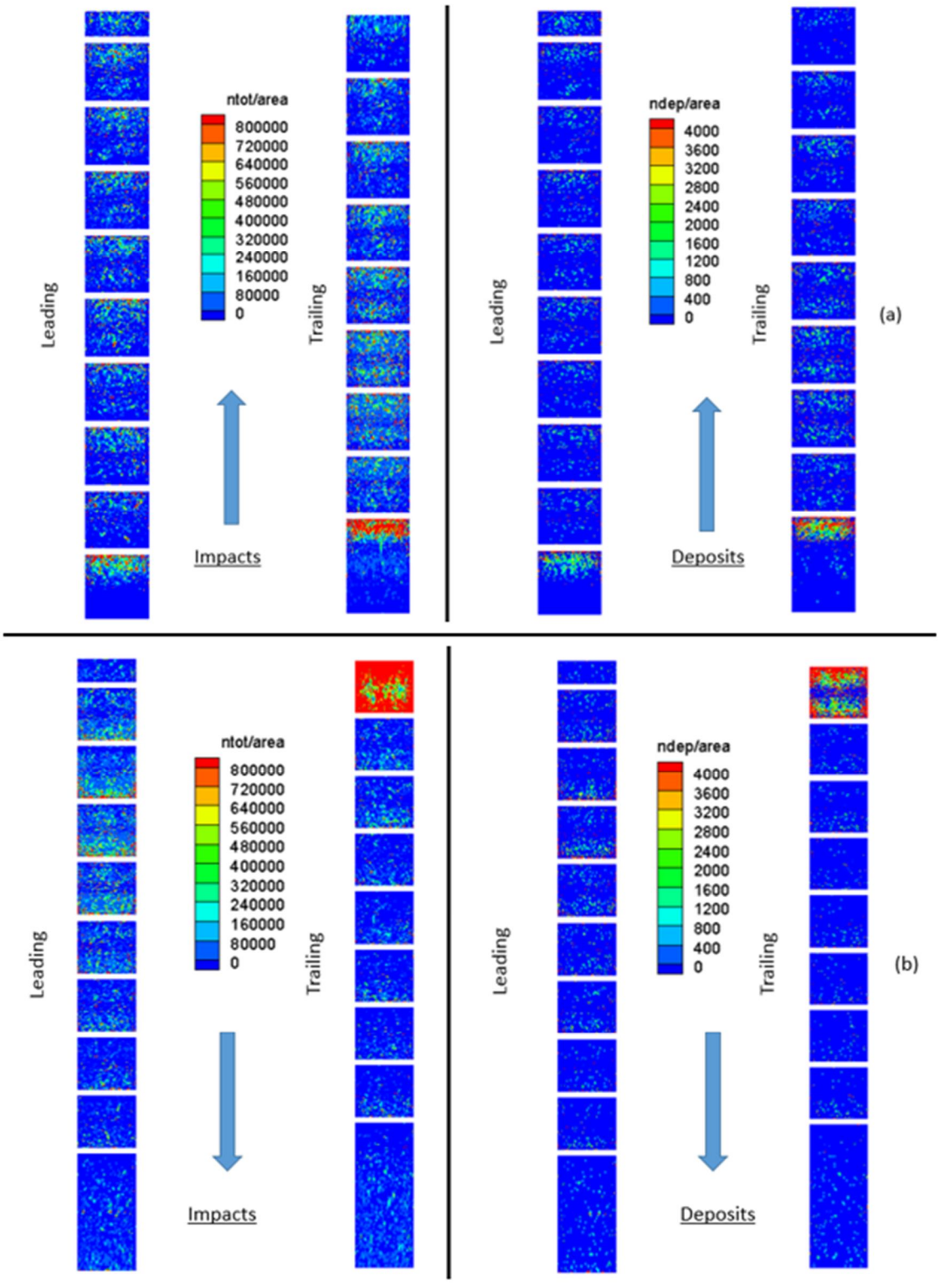

Figure 4.8. Contours of particle impingement (left) and deposition (right) for (a) first pass, (b) second pass on the ribbed walls for Ro = 0.0 and a wall temperature of 1050°C.

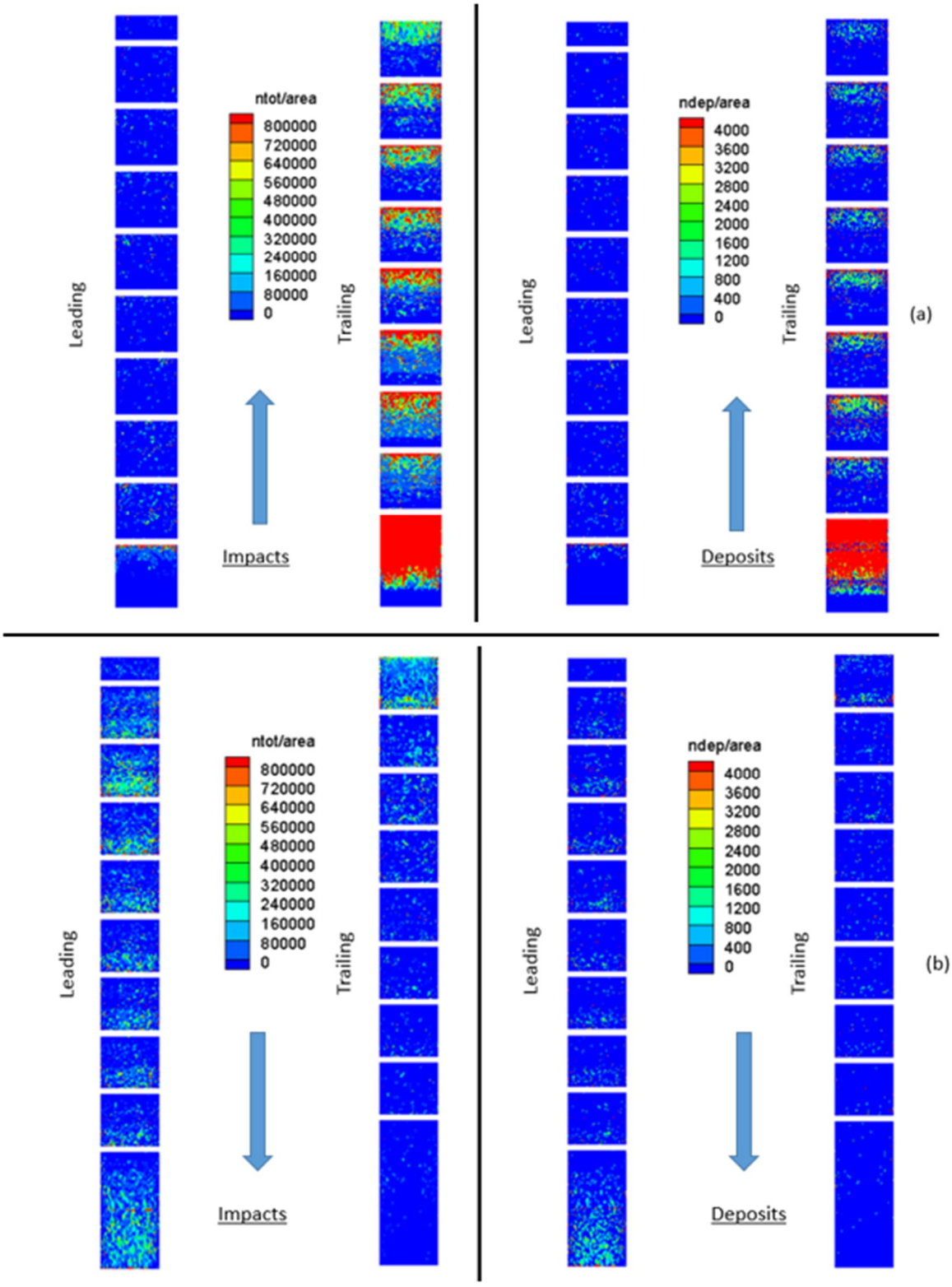

Figure 4.9. Contours of particle impingement (left) and deposition (right) for (a) first pass, (b) second pass on the ribbed walls for Ro = 0.2 and a wall temperature of 1050°C.

The smooth side walls are investigated in Figures 4.10 and 4.11 for Cases 1 and 4, respectively. Both the stationary duct and the rotating duct have cross-sectional secondary flows present which could potentially influence particle trajectories. In the stationary duct, the secondary flow is particularly strong at the ribs at which spanwise velocities of the order of 15-20% of the mean streamwise velocity are generated and directed towards the side wall. In rotating ducts, because of the cross-stream pressure gradient imposed by the Coriolis forces, a secondary flow is generated throughout the pitch as shown in Appendix B, (Figures B7, 8, 12-15) which could potentially entrain particles to the vicinity of the side smooth walls.

Comparing Figures 4.10 and 4.11, show that in the first pass the side walls experience substantial particle impacts and less than 0.5% of these impacts lead to deposition. While the impacts and deposition are symmetric about the centerline for the stationary case, in the rotating duct these are biased towards the trailing wall driven by the effect of Coriolis forces on particle trajectories. Also in the rotating duct, the effect of secondary flow is very evident at ribs on the trailing side of the side wall showing a large concentration of impacts just upstream and near the top of the ribs. In the U-bend, the number of impacts and deposition in the stationary duct is much higher than that observed in the rotating duct. While rotational effects could have something to do with this result, the main reason for this trend is the observation that about 40% of the particles deposit in the first three rib pitches in the rotating duct so fewer particles remain in the flow entering the U-bend. There are no notable differences between the impingement and deposition trends in the second pass, except that in the stationary duct more impact and deposition is realized because of the availability of more particles, and as the flow progresses into the pass, a greater concentration of impacts are observed toward the leading side of the rotating duct, because of the rotational Coriolis forces.

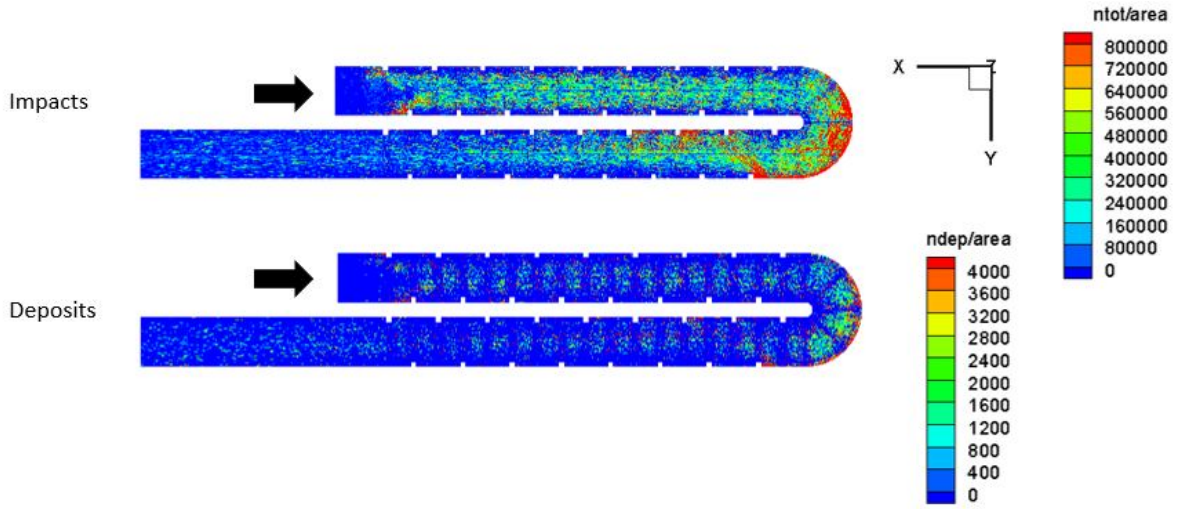

Figure 4.10. Contours of particle impingement (top) and deposition (bottom) for smooth side wall (Z =1.0), with a Ro = 0.0 and a wall temperature of 1050°C.

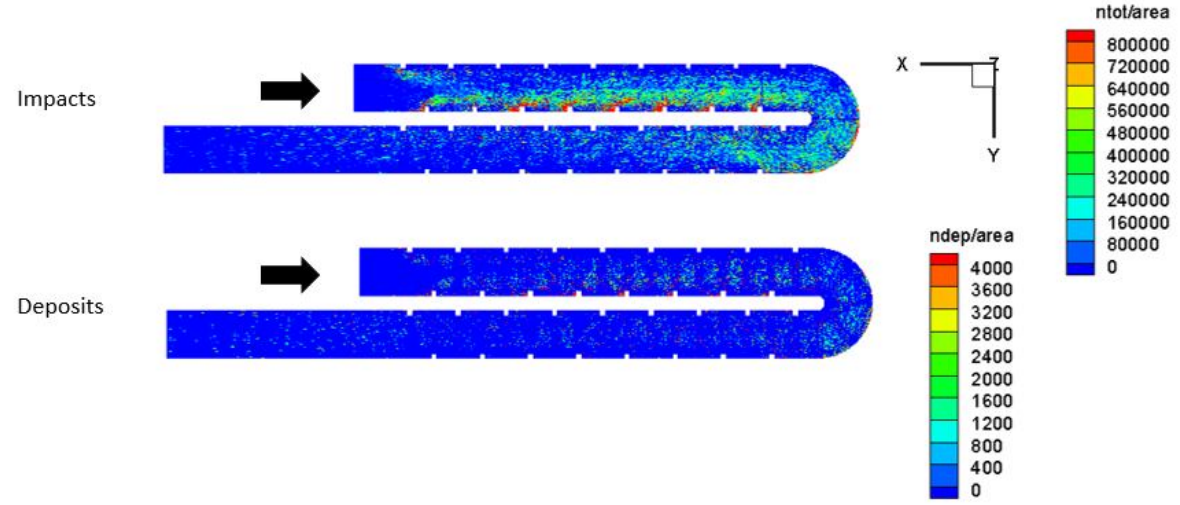

Figure 4.11. Contours of particle impingement (top) and deposition (bottom) for smooth side wall (Z = 1.0), with a Ro = 0.2 and a wall temperature of 1050°C.

Results are now presented for the end and inner walls of the bend, for Cases 1 and 4 in Figures 4.12 and 4.13, respectively. As in previous plots, results presented show impingement and deposition levels per unit non-dimensional area. However, it is noted that due to the high levels of impingement and deposition, the end wall figure has a different scale than previously presented. Coordinate axis and arrows that represent flow direction are given for reference.

Impingement and deposition is higher in the stationary domain on the end wall, as shown in Figure 4.12, which is due to there being more partilces still present in the flow as discussed previously. A notable difference between the stationary and rotating duct is the location of impacts. In the rotating case, the area of high impact is shifted further downstream into the bend; this is because most of the particles coming out of the first pass are concentrated at the trailing wall and as they manuever the bend they impinge the end wall further downstream than the stationary configuration in which the particles are uniformly distributed at the entrance to the bend. In the rotating and stationary configurations, a high relative density of impacts and deposition is observed at the corners (Z=±1) in the downstream half of the bend.

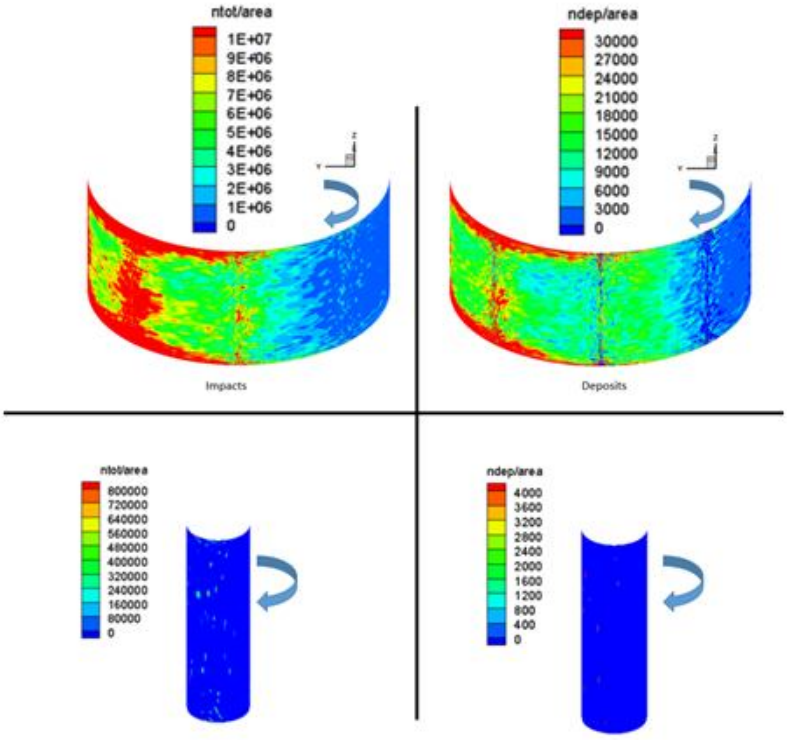

Figure 4.12. Contours of particle impingement (left) and deposition (right) for end (top) and inner walls (bottom), with a Ro = 0.0 and a wall temperature of 1050°C.

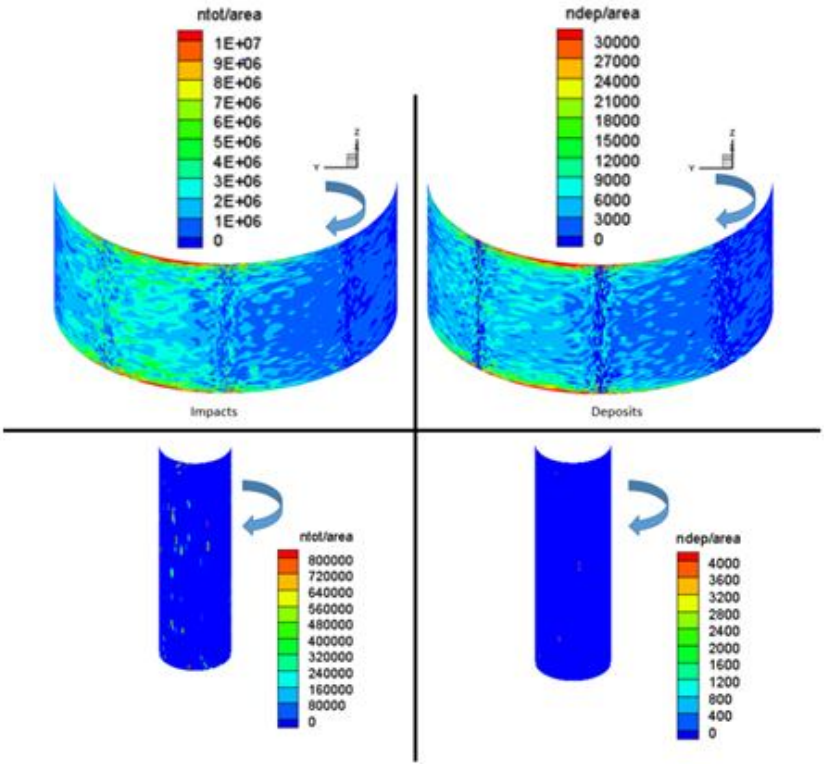

Figure 4.13. Contours of particle impingement (left) and deposition (right) for end (top) and inner walls (bottom), with a Ro = 0.2 and a wall temperature of 1050°C.

Finally the leading ribbed surfaces facing the flow are investigated in Figures 4.14 and 4.15, for the statioary duct in the first and second pass, respectively. Corresponding results for the rotating duct are presented in Figure 4.16 and 4.17 in the first and second pass, respectively. The results are oriented with the ribbed wall surface always at the bottom. Note that due to the higher levels of impingement and deposits in the rotating case the scales have been changed.

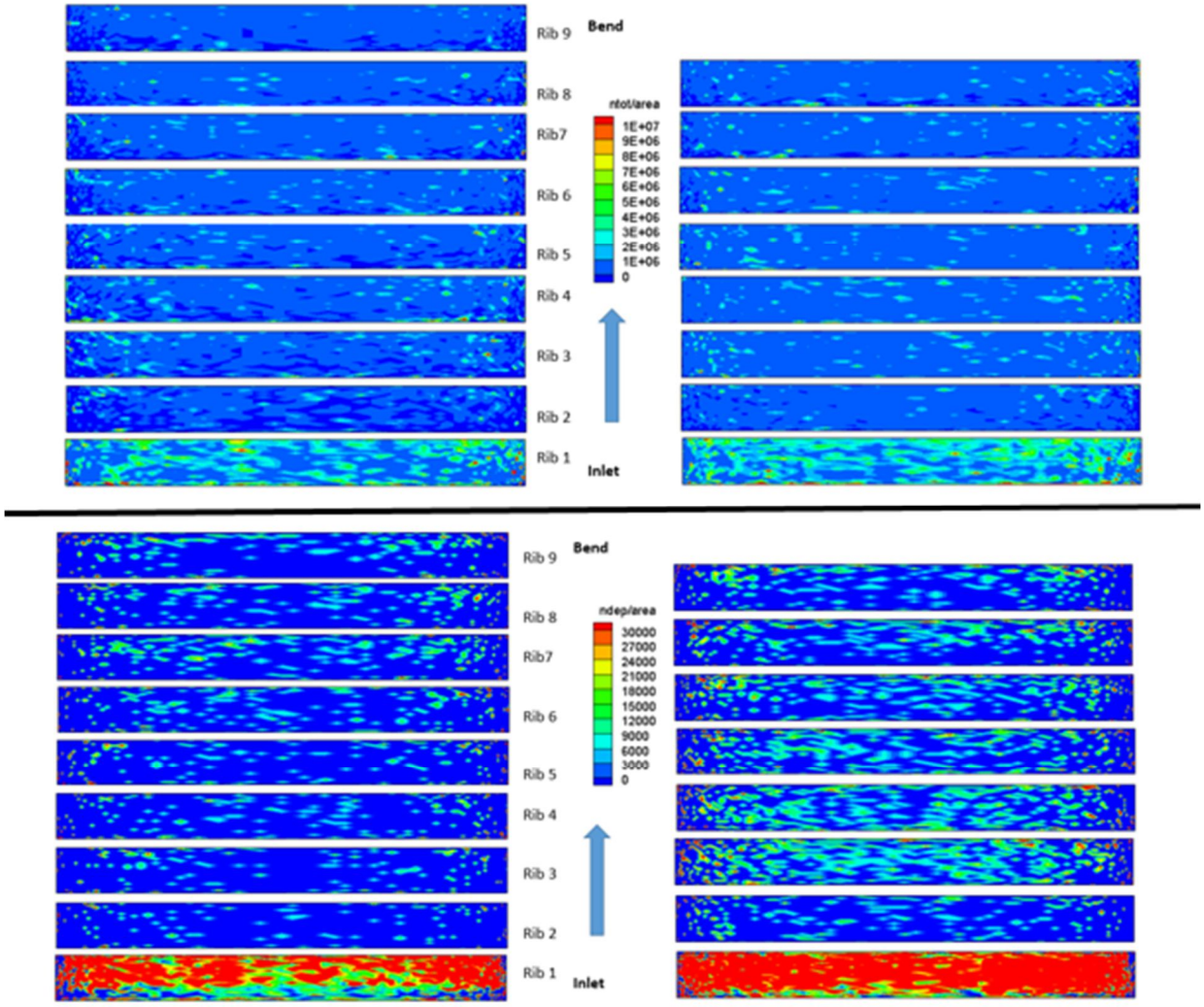

Figure 4.14. Contours of particle impingement (top) and deposition (bottom) for the leading (left) and trailing walls (right) in the first pass, with a Ro = 0.0 and a wall temperature of 1050°C.

Results in Figures 4.14 and 4.15 show relatively similar impingement and deposition patterns on the rib faces in both the first and second passes. However, much higher densities of impact and deposition are observed in the first pass, particularly at the first rib. As previously mentioned, the particles are injected just upstream of the first rib at the fluid velocity in a uniform flow and they will have a strong probability of impinging on the rib. In an actual blade the incoming flow will be quite turbulent and the level of impingement and deposition will not as high as predicted here. In the second pass, the ribs on the leading wall experience more impacts as the particles coming out of the bend are directed towards the leading wall.

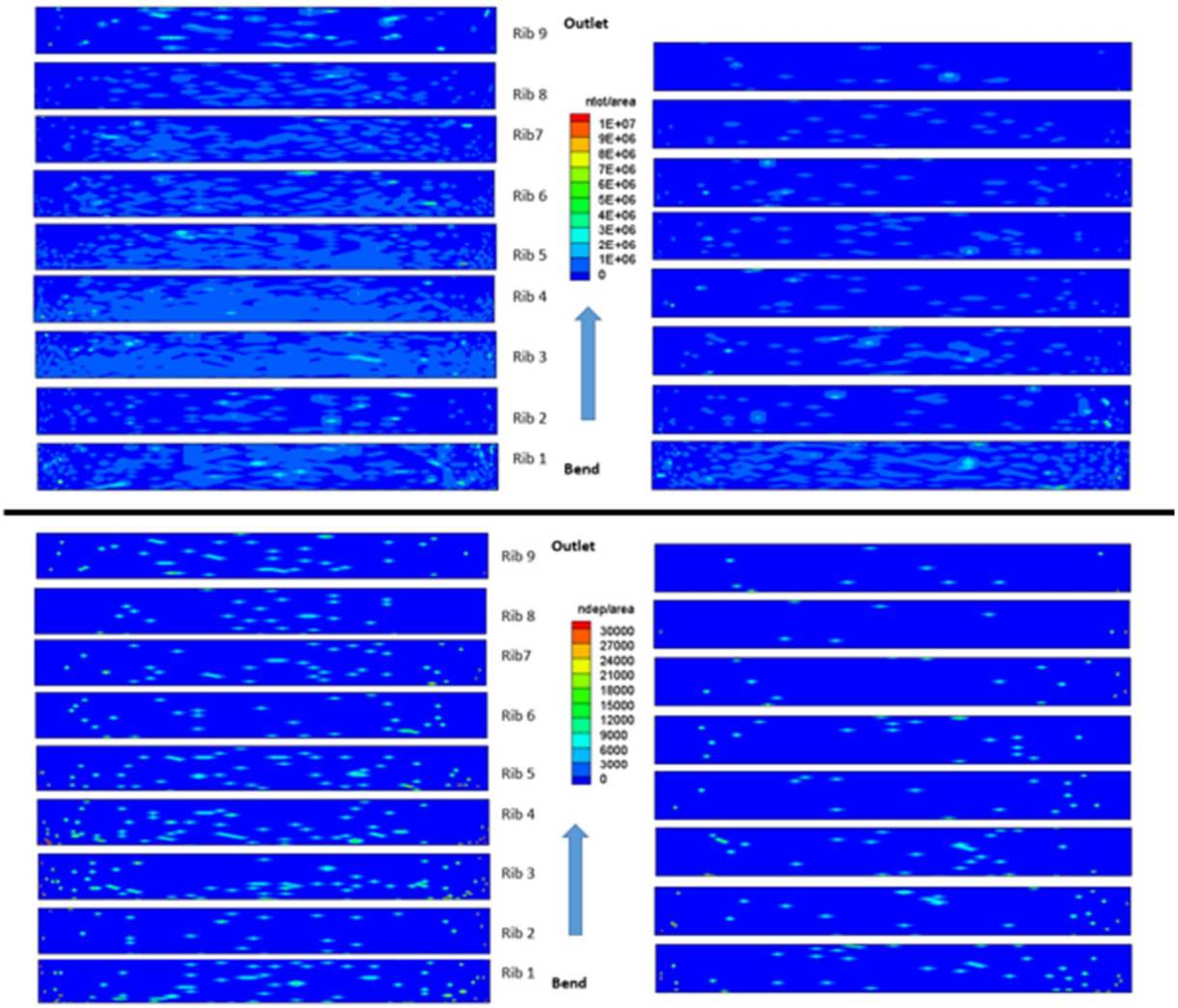

Figure 4.15. Contours of particle impingement (top) and deposition (bottom) for the leading (left) and trailing walls (right) in the second pass, with a Ro = 0.0 and a wall temperature of 1050°C.

Results in Figure 4.16 show the larger impingement and deposition results along the trailing wall in the first pass. As explained previously in Chapter 3, the particle laden flow will impinge on the trailing wall more due to the action of Coriolis force. The effect of Coriolis forces acting on the particles is most evident as they traverse through the first few ribs and impinge/deposit on the rib faces. Results also follow expected trends in the second pass, with the leading wall having higher impingement and deposition levels due to the flow and the particles interacting with the leading wall more due to the action of Coriolis forces, on both the fluid and particles.

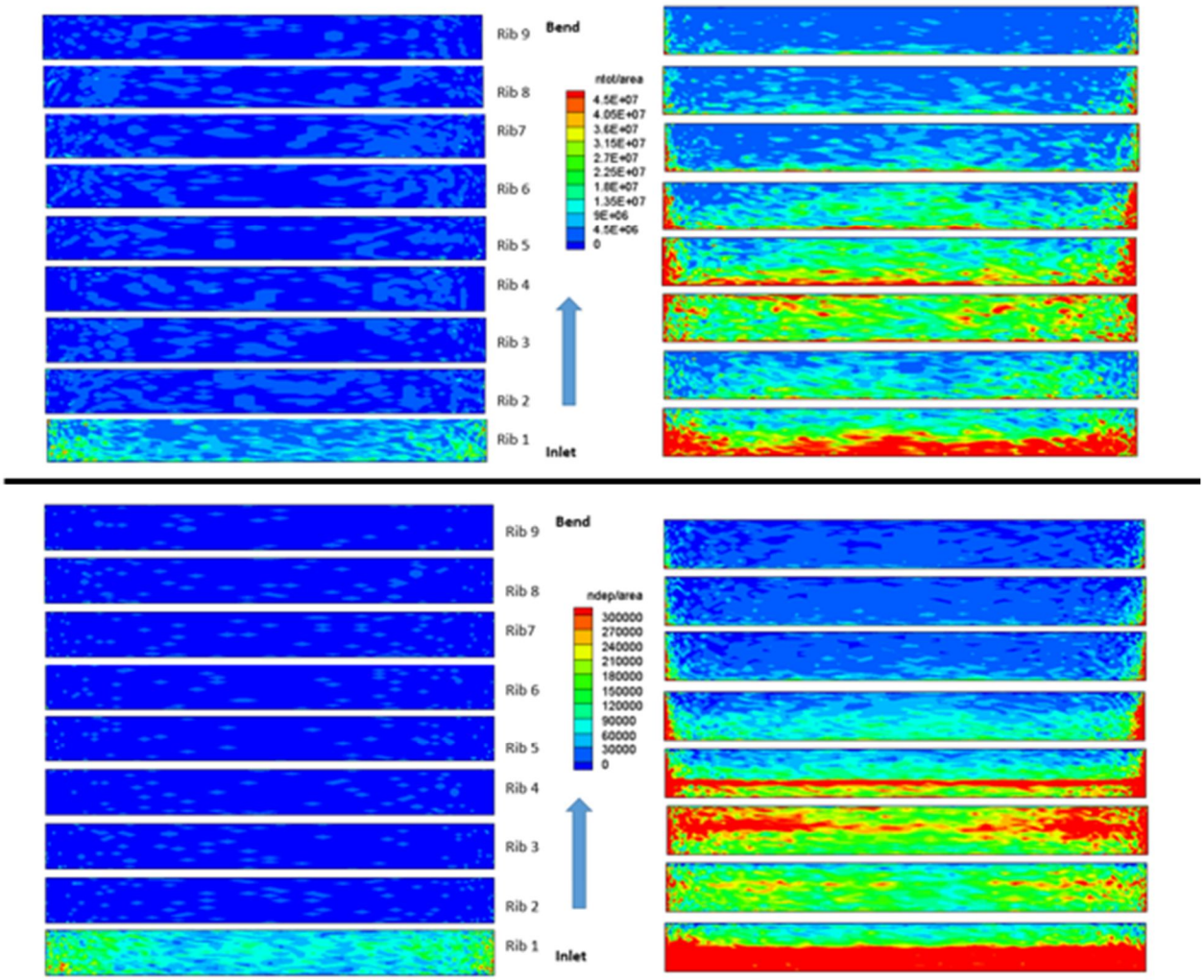

Figure 4.16. Contours of particle impingement (top) and deposition (bottom) for the leading (left) and trailing walls (right) in the first pass, with a Ro = 0.2 and a wall temperature of 1050°C.

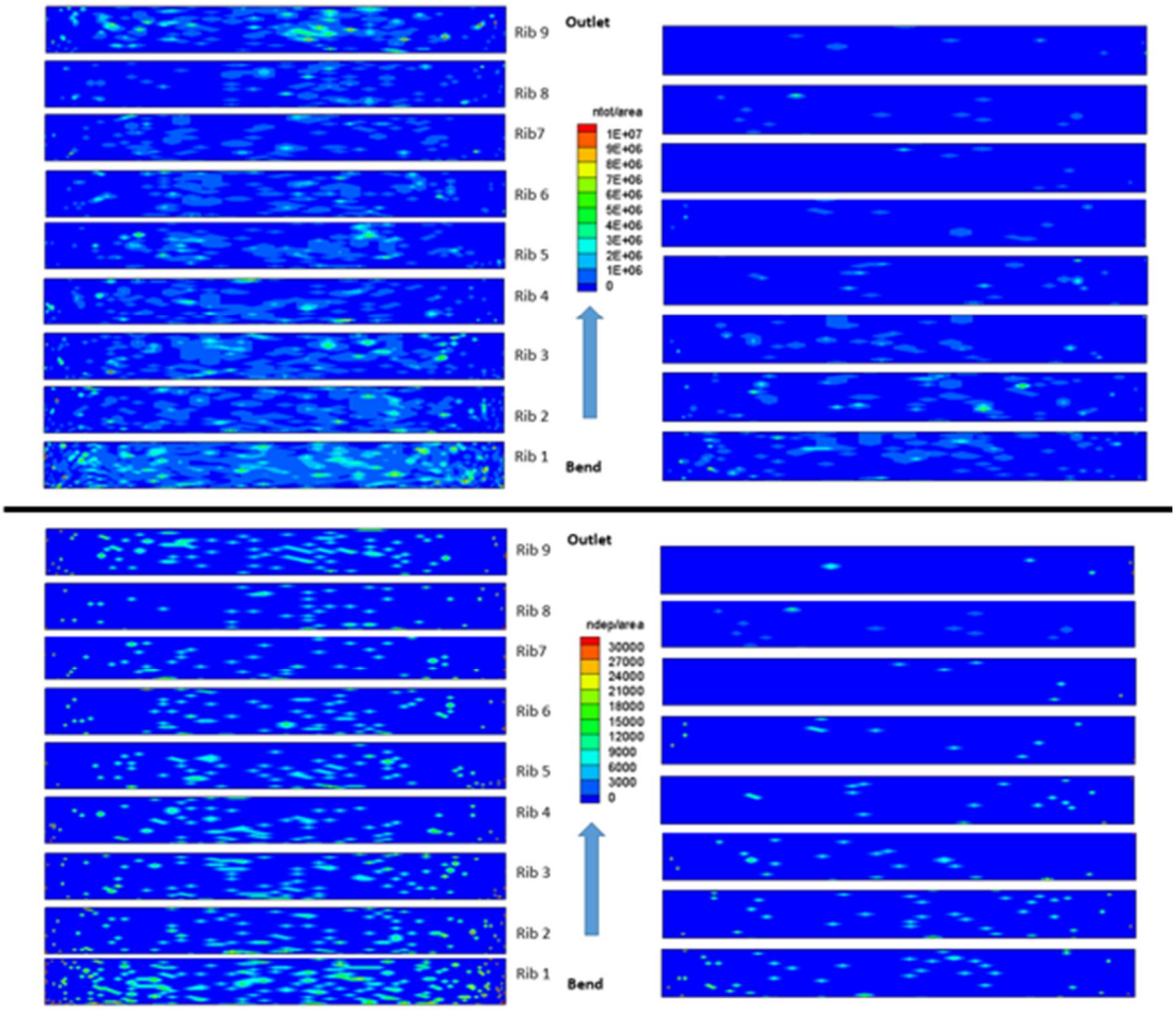

Figure 4.17. Contours of particle impingement (top) and deposition (bottom) for the leading (left) and trailing walls (right) in the second pass, with a Ro = 0.2 and a wall temperature of 1050°C.

To summarize the contour plots previously presented, two regions of high deposition are identified, along the trailing wall in the first pass and in the bend, for the rotating and stationary cases, respectively. To represent the predictions in these two regions better, deposition locations for rotating and stationary (1050°C) cases are given in Figure 4.18 and 4.19 for the first pass trailing wall and bend, respectively. Results are presented for the different particle diameters, to show possible size dependent effects on deposition locations.

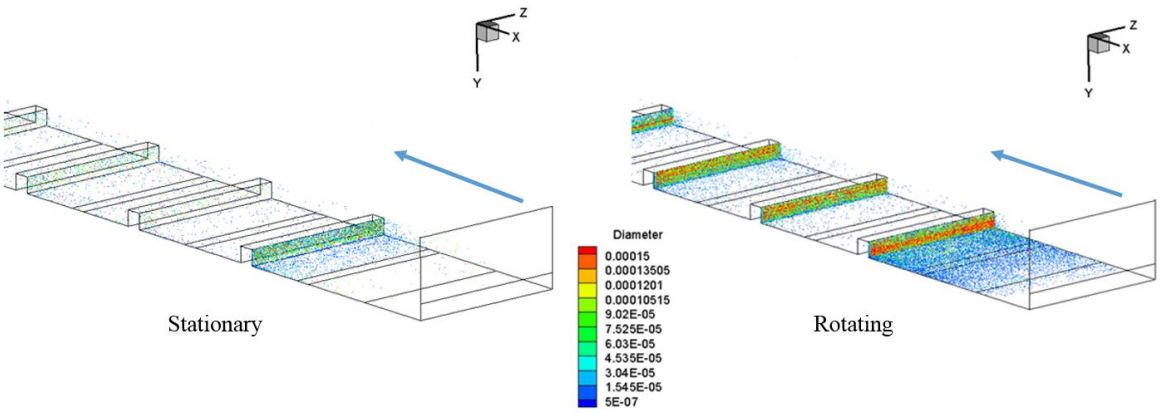

Figure 4.18. Particle deposition locations in the first pass along the trailing wall, color contours represent different particle diameters.

Deposition patterns in Figure 4.18 shows that most of the deposition in the first three rib pitches occurs at the rib faces facing the flow due to the Coriolis force acting on the particles and forcing them towards the trailing wall. The larger particles tend to mostly deposit on the rib faces together with some smaller particles. On the ribbed wall, on the other hand, mostly smaller diameters particles deposit. Figure 4.19 deposition predictions show that in the bend region the stationary case has, on average, larger particle sizes that deposit as they traverse the bend, when compared to the rotating predictions. This is due to all of the larger particles depositing before they enter the bend region in the rotating case.

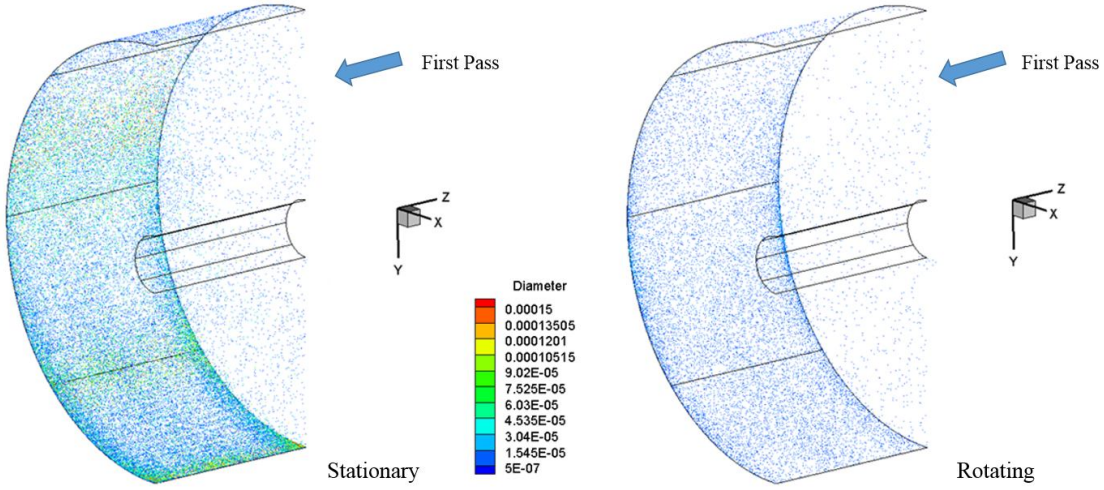

Figure 4.19. Particle deposition locations in the bend region, flow is moving from top to bottom, color contours represent different particle diameters.

To summarize, in quantitative form, the results of deposition and impingement within the entire domain, Table 4.2 is presented. Presented are the total number of impacts and deposits in all four cases. The bolded percentages are calculated as shown in Equation 4.7 for the sticking (η_{stick}) and capture (η_{cap}) efficiencies. Defining N_{dep} as the number of deposited particles, N_{imp} as the number of impacting particles, and N_{inj} as the number of injected particles (200,000).

$$\eta_{stick} = \frac{N_{dep}}{N_{imp}}, \ \eta_{cap} = \frac{N_{dep}}{N_{inj}} \tag{4.7}$$

It can be surmised from the Table that the wall temperature has very little effect on deposition as shown by the similar capture efficiencies. The number of particles deposited increase by about 0.11% when the wall temperature increases from 950 °C to 1000 °C and further by an additional 0.6% when the wall temperature is 1050 °C. The relative insensitivity of deposition to the wall temperature can be attributed to the high Reynolds number and the high bulk flow which does not heat up enough to raise the particle temperature to near the wall temperature. More than the wall temperature, rotation seems to influence deposition. As mentioned earlier, about 40% of the particles deposit in the first three rib pitches under rotation because of the strong effect of Coriolis forces. Particles that do not deposit are retained near the trailing wall where they continuously impinge on the trailing wall leading to increased deposition.

Table 4.2 Total impact and deposition results with sticking and capture efficiency for each case.

	Wall Temp °C	Simulated	Sticking Efficiency (η_{stick})	Capture Efficiency (η_{cap})
Number of Impacts	Stat 950	53.1 Million	-	-
	Stat 1050	43.1 Million	-	-
	950	41.8 Million	-	-
	1000	40.3 Million	-	-
	1050	37.4 Million	-	-
Number of Deposits	Stat 950	112,510	**0.21%**	**56.25%**
	Stat 1050	115,886	**0.27%**	**57.94%**
	950	174,160	**0.42%**	**87.08%**
	1000	174,359	**0.43%**	**87.18%**
	1050	175,390	**0.47%**	**87.70%**

4.3.2 Average Impact Characteristics

As in the impact and deposition distribution results, impact characteristics given by velocity, angle, and temperature at impact are quite similar for the different wall temperatures and thus results from only the stationary and rotating cases at 1050°C will be discussed. Results for Case 2, 3, and 5 (rotating 950°C, rotating 1000°C and stationary 950°C, respectively) are presented in Appendix D. Results are presented here as contour plots that have been recorded and averaged for the entire simulation.

4.3.2.1 Average Impact Velocity

Figure 4.20 plots the average impact velocity on the smooth side walls. In the first pass, the average impact velocity is higher with rotation because of the additional Coriolis and centrifugal forces that act on the particle. The highest impact velocities are experienced by the particles exiting the bend, early in the second pass.

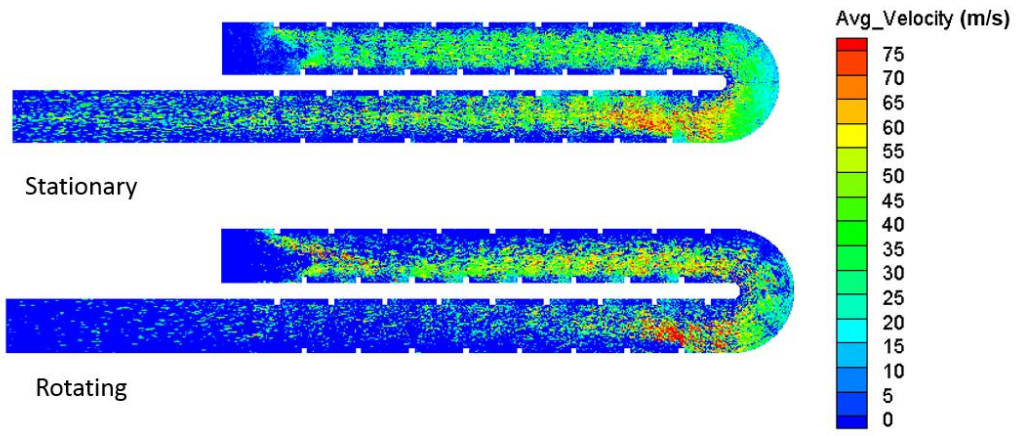

Figure 4.20. Contours of average particle impacting velocity (m/s) for smooth side walls for the stationary (Ro = 0.0) and rotating domains (Ro = 0.2) for a wall temperature of 1050°C.

The average impact velocity is presented for the leading and trailing walls of the first and second pass in Figure 4.21. Results for the stationary case show relatively lower impact velocities in comparison to the rotating case in the first pass. This is again due to the additional Coriolis force acting on the particles and accelerating them towards the trailing wall. As the flow and particles approach the bend and accelerate near the trailing wall, the particles impact the region with a higher velocity for both stationary and rotating ducts. Higher impact velocities are also predicted in the second pass along the leading wall for both rotating and

static cases, where the separated shear layer in the bend reattaches. High impingement velocities are also observed on the trailing wall coming out of the bend as the accelerated particles cannot maneuver the bend and impinge on the trailing wall in both the stationary and rotating ducts. This supports the general observation that the bend region is not influenced by Coriolis and centrifugal buoyancy forces as much as by the geometry of the bend itself which causes the flow to accelerate around the outer end wall and separate at the inner wall.

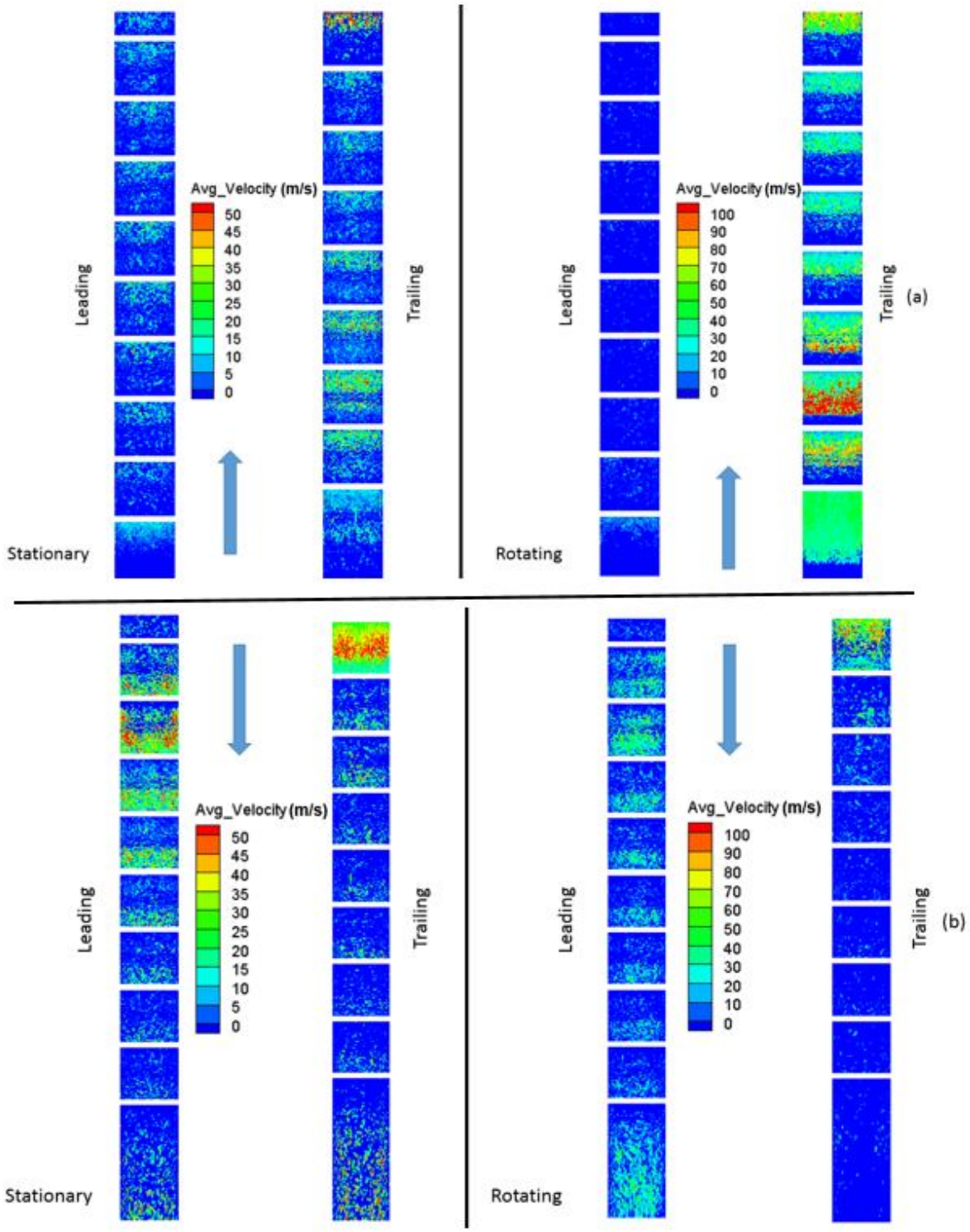

Figure 4.21. Contours of average particle impacting velocity (m/s) for leading and trailing walls in the (a) First pass and (b) Second pass of stationary (Ro = 0.0) and rotating domains (Ro = 0.2) for wall temperature of 1050°C. Note - velocity scales are not similar.

Results on the end and inner wall of the bend are presented in Figure 4.22. The inner wall experiences very little impingement and therefore has similar average velocity predictions in both cases. The end wall predictions show two regions of high velocity impingement, one near the exit of the bend and another near the inlet of the bend that aligns mid-channel with the first pass (Ro =0.0) and middle of bend (Ro=0.2). The higher velocity near the end of the bend is due to particles that have accelerated while navigating the bend and which contact at higher speeds. The other region near the first pass is due to the location of particles between the leading and trailing sides just before particles enter the bend. The particles closer to the leading wall will feel the influence of the bend later than those near the trailing side and will therefore be unable to navigate the bend as successfully and will impinge closer to the first pass. Since these particles have been in the mean flow of the channel they will have a higher velocity. The shift from the mid-channel first pass high velocity location in the stationary case to the middle of the bend in the rotating case is due to the location of the particles being more concentrated near the trailing wall in the first pass.

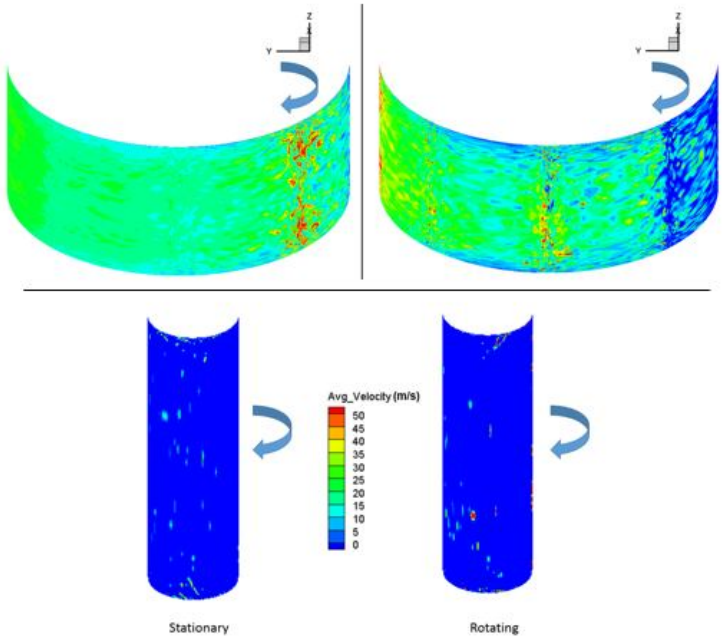

Figure 4.22. Contours of average particle impacting velocity (m/s) for end (top) and inner walls (bottom), for stationary (left) and rotating domains (right), for a wall temperature of 1050°C.

Results on the first three front rib faces are presented in Figure 4.23 on the leading and trailing walls for Case 1 and 4. The results are oriented with the ribbed wall always at the bottom and the arrow reperesents the flow direction. The stationary case experiences significantly higher velocities than the rotating case due to the rotating case particles transport having the Coriolis force directing particles into the trailing wall. The rotating case particles impinge on the trailing wall and then rebound into the rib face at much lower velocities than a direct/normal impingement as seen in the stationary case.

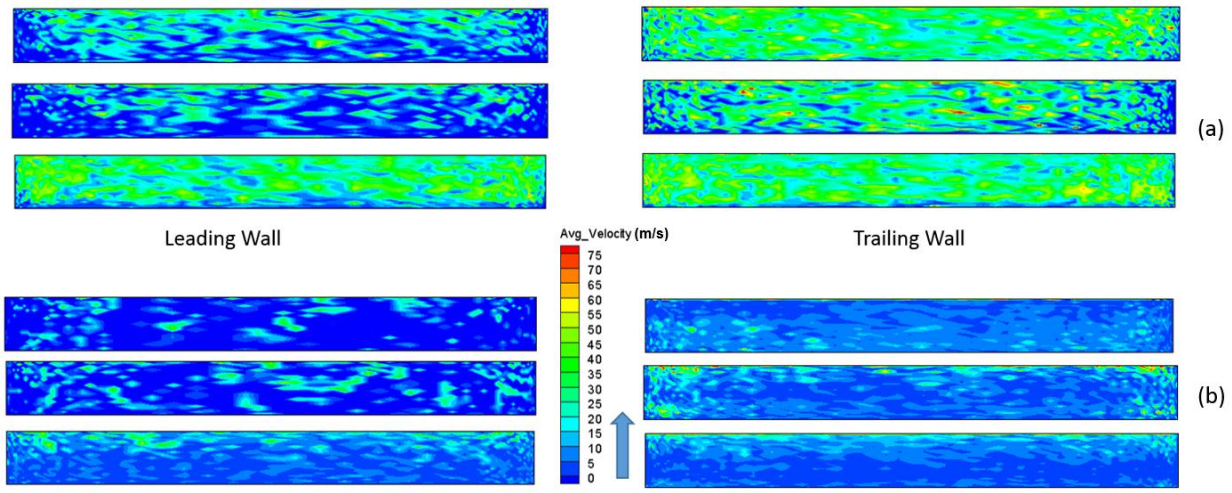

Figure 4.23. Contours of average particle impacting velocity (m/s) for the first three rib faces on the leading and trailing walls for (a) Stationary and (b) Rotating cases.

4.3.2.2 Average Impact Angle

The average impacting angle is presented in degrees from surface for the smooth side walls in Figure 4.24. Results show very similar patterns in both the stationary and rotating geometries, with most of the collision having shallow impact angles with the smooth side walls, which relates to higher COR's and lower deposition probability.

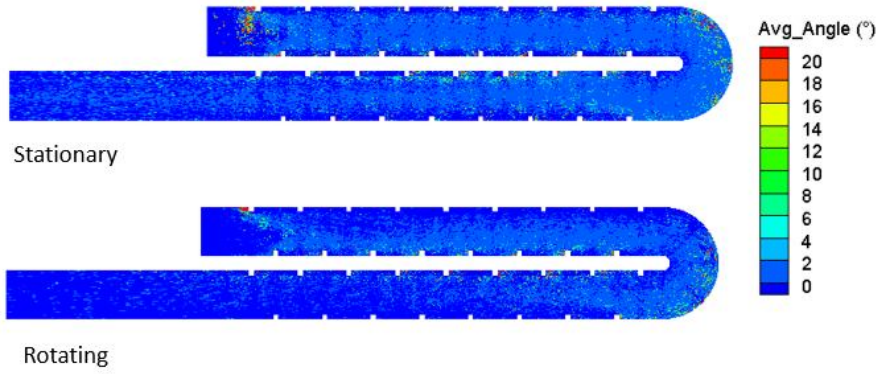

Figure 4.24. Contours of average particle impacting angles for the smooth side walls for the stationary (Ro = 0.0) and rotating domains (Ro = 0.2) for a wall temperature of 1050°C.

The average impacting angle is presented for the leading and trailing walls in the first and second passes in Figure 4.25. Results for the stationary case show relatively similar angle prediction in the first pass for both of the leading and trailing walls. As the angles are approximately less than 30°, it is assumed that most of these are glancing collisions and therefore will have higher predictions of COR. In contrast, for the first pass, the rotating case shows more impacts on the trailing wall with angles closer to 50°, meaning the collisions are more normal to the surface and will therefore have lower COR predictions. Another interesting prediction in the first pass, is the low impact angles (<10°) just before the first ribs in the stationary and more noticeably in the rotating case. As these are averaged results, a much larger concentration of glancing collisions may be dominating the results in this region. As particles do not have enough energy to pass the first rib they will continue to contact the trailing wall at very small heights. These collisions are more of the sliding type with near unity tangential COR predictions and extremely low normal COR predictions, resulting in a low probability of rebounding past the first rib. Because of the large number of impacts in this region, even a very low probability of deposition leads to a substantial levels of deposition.

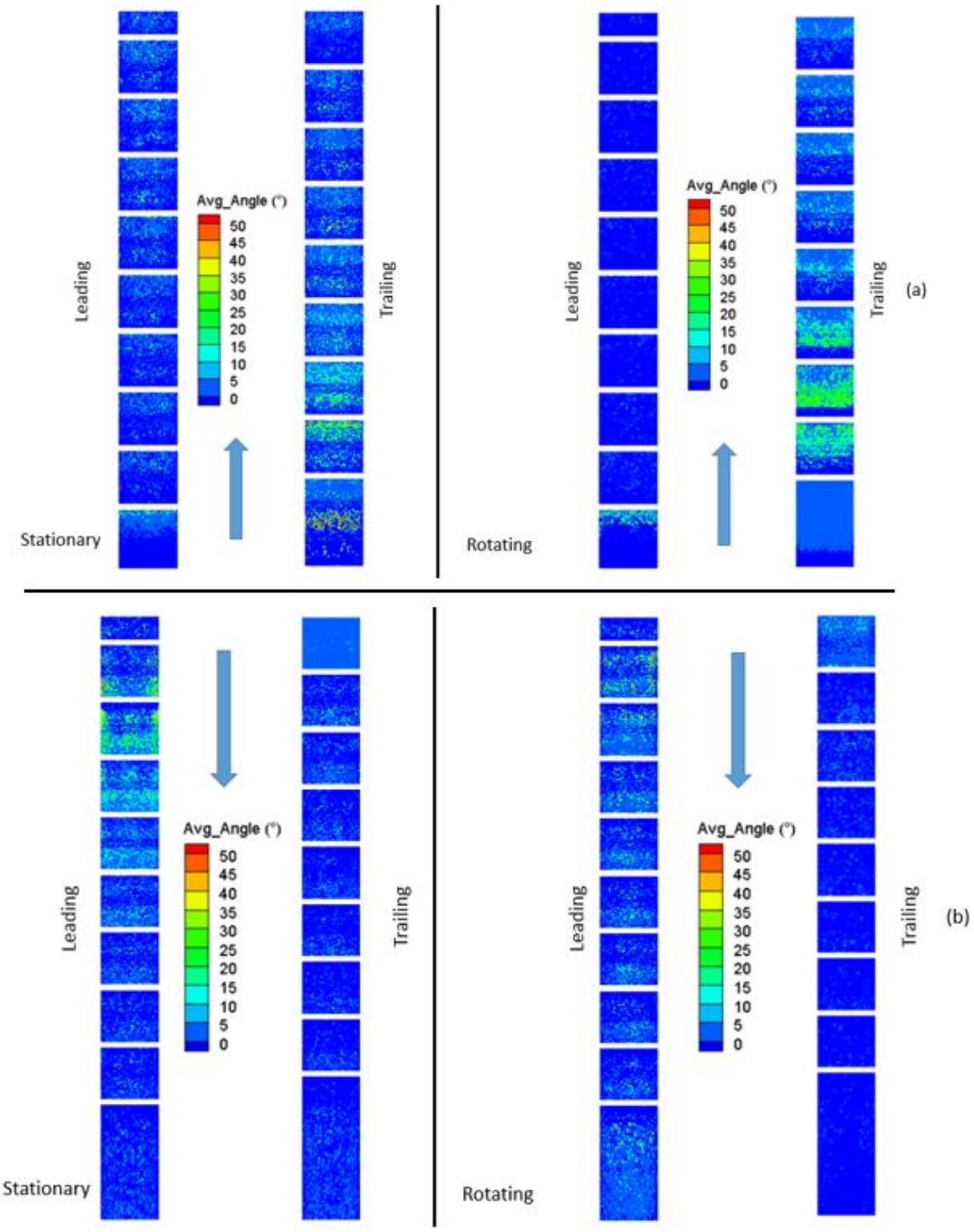

Figure 4.25. Contours of average particle impacting angles for leading and trailing walls in the (a) First pass and (b) Second pass of stationary (Ro = 0.0) and rotating domains (Ro = 0.2) for wall temperature of 1050°C.

Results on the end and inner walls are presented in Figure 4.26. The results shown for the average angle show shallow angles of impact in most of the bend except near the first pass exit in the stationary duct. Regions of high impact angles in the rotating duct are scarce because of the low number of impacts coupled with the Coriolis force effect.

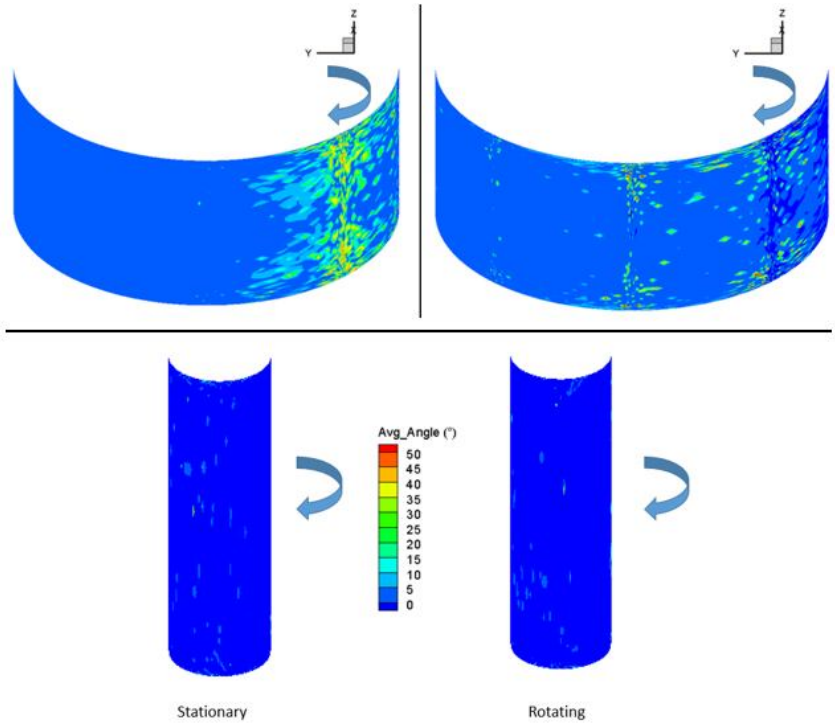

Figure 4.26. Contours of average particle impacting angle for end (top) and inner walls (bottom), for stationary (left) and rotating domains (right), for a wall temperature of 1050°C.

Results on the first three front rib faces are presented in Figure 4.27 on the leading and trailing walls for Case 1 and 4. The results are oriented with the ribbed wall surface always at the bottom and the arrow reperesents the flow direction. Results show that the stationary case has more normal impacts in comparision to the rotating case. This supports the higher impact velocity results in the stationary case in Figure 4.23. This also supports the assertion that the particles in the rotating case initially contact the trailing wall and then contact the front rib faces.

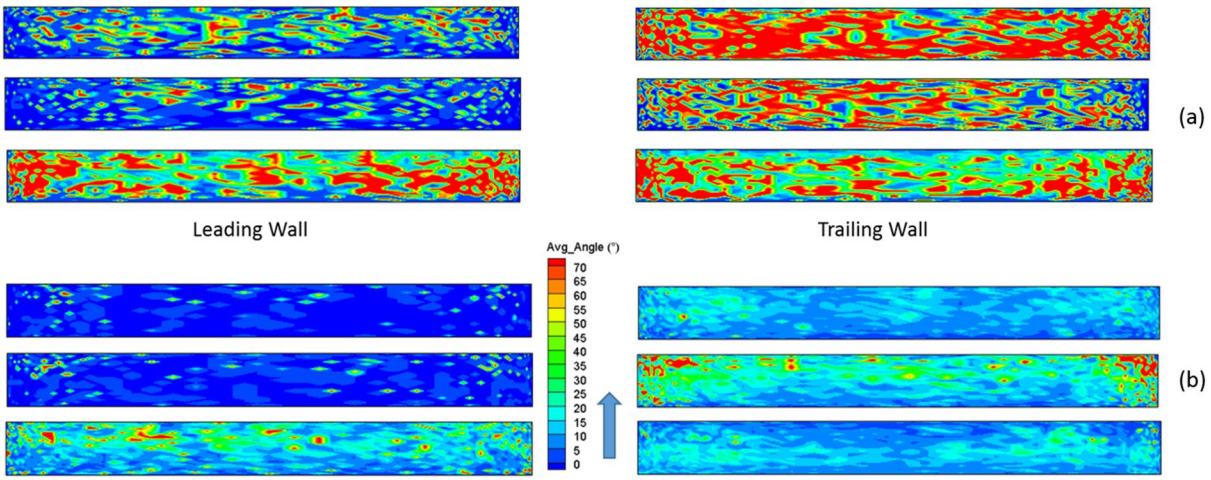

Figure 4.27 Contours of average particle impacting angle for the first three rib faces on the leading and trailing walls for (a) Stationary and (b) Rotating cases.

4.3.2.3 Average Impact Temperature

The predictions for the average impacting temperature are now presented for the smooth side walls in Figure 4.28. The average temperature is presented in dimensional form in degrees Celsius. Results show similar temperature levels in both the stationary and rotating cases with an average temperature of around 700°C to 850°C for all collisions on the smooth side wall throughout the domain. Results show that particles on average do not reach the threshold for deposition on the smooth side walls.

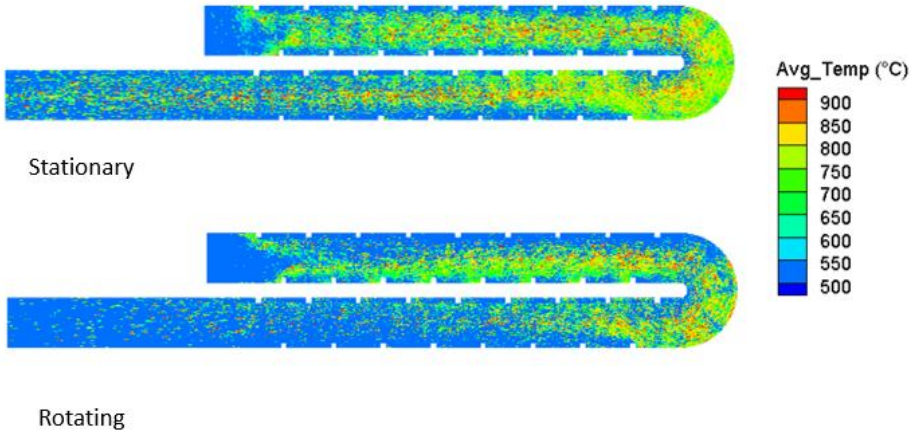

Figure 4.28. Contours of average particle impacting temperatures for the smooth side walls for the stationary (Ro = 0.0) and rotating domains (Ro = 0.2) for a wall temperature of 1050°C.

The average impacting temperature is presented for both the leading and trailing walls in both passes of the domain in Figure 4.29. Results for the stationary case show similar impacting temperatures along the leading and trailing walls in the first pass. The second pass shows slightly higher temperatures and the impacts follow patterns discussed previously. In both rotating and stationary ducts, the region before the first rib exhibits uncharacteristically high particle impact temperatures. This is followed by higher impact temperatures on the trailing wall of the rotating duct. Small particle diameters, shallow angles of impact, and increased residence time in the vicinity of the wall could be source of the contributing factors leading to these results. A more quantitative investigation of this phenomenon will be discussed later. The leading wall in the second pass shows similar temperature levels to those in the stationary case with an increase in temperature approaching the end of the domain. This is due to particles that have navigated the entire domain, heating up as a response and finally coming into contact with the leading wall due to Coriolis forces.

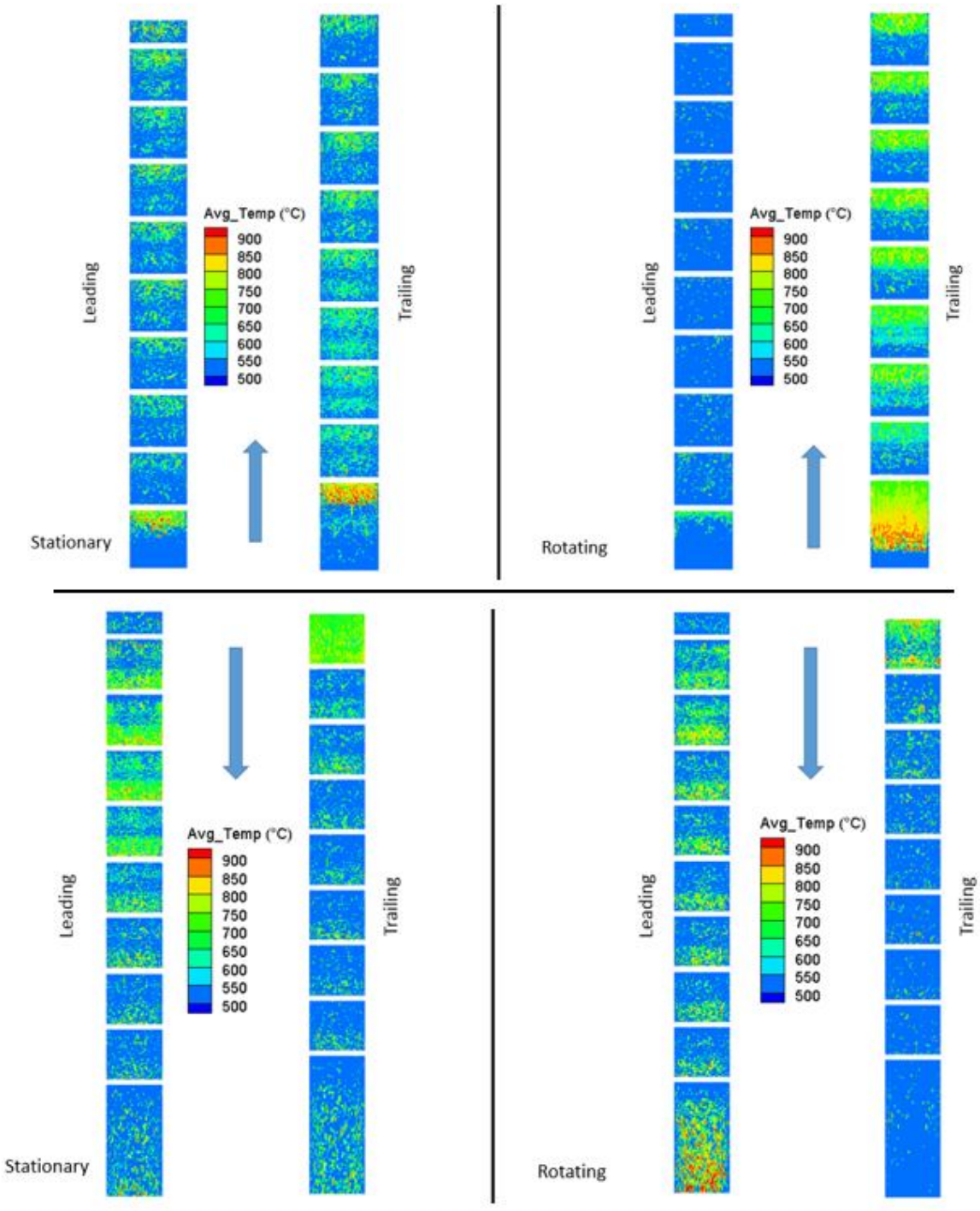

Figure 4.29. Contours of average particle impacting temperatures for leading and trailing walls in the (a) First pass and (b) Second pass of stationary (Ro = 0.0) and rotating domains (Ro = 0.2) for wall temperature of 1050°C.

Results on the inner and end walls within the bend are presented in Figure 4.30. The results show similar results on the inner wall when comparing stationary and rotating cases. The rotating duct shows higher temperature impacts on the end wall than the stationary duct. The higher temperatures in the rotating cases are due to the majority of the impacts in the bend coming from smaller particle sizes. This is due to the majority of the larger particle sizes having deposited before entering the bend, supported by Figure 4.18 and will be demonstrated more clearly in following sections. The smaller particle sizes are able to remain in the near wall region in the first pass without impinging on a wall, and therefore are able to heat up more. Similar average temperatures would be expected in the stationary case if the larger number of large particles did not dominate the impingement levels in the bend.

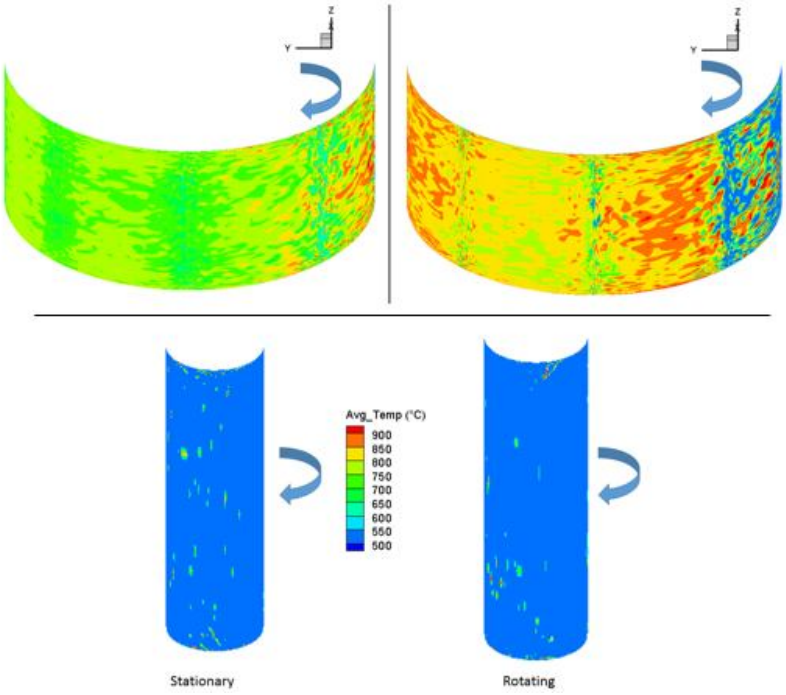

Figure 4.30. Contours of average particle impacting temperatures for end (top) and inner walls (bottom), for stationary (left) and rotating domains (right), for a wall temperature of 1050°C.

Results on the first three front rib faces are presented in Figure 4.31 on the leading and trailing walls for Case 1 and 4. Temperature results show similar temperatures on rib faces for both rotating and stationary cases on both leading and trailing walls, supporting the assertion that deposition results do not have a strong temperature dependence.

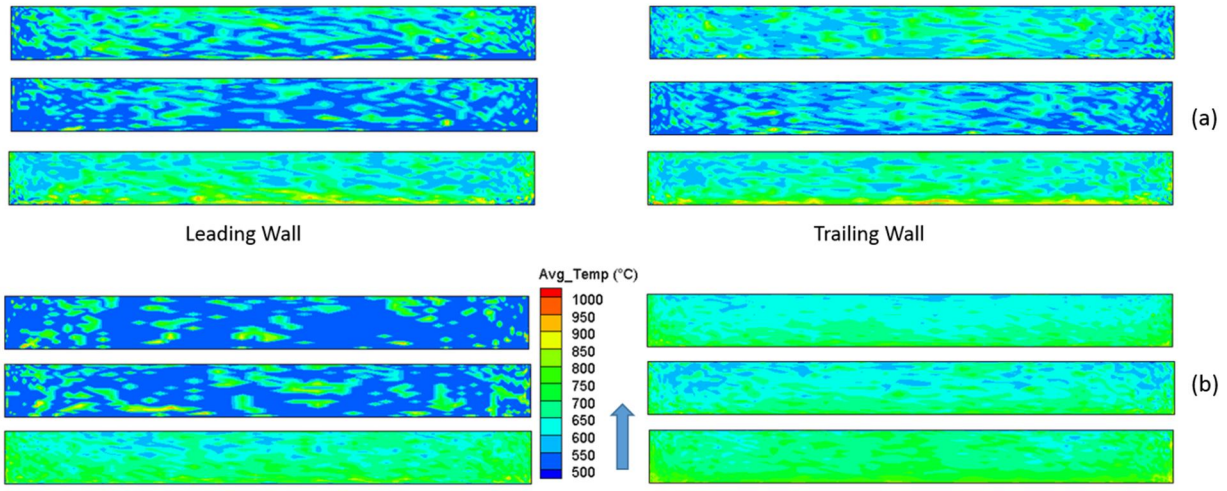

Figure 4.31. Contours of average particle impacting temperature for the first three rib faces on the leading and trailing walls for (a) Stationary and (b) Rotating cases.

4.3.3 Particle Size Effects

As shown in Figure 4.2, the particle size range is divided into 10 groups sized by diameter to better represent the dynamics of different particle sizes and the effects that the size of the particle has on impact and deposition characteristics. The size groups are distributed such that there are more groups in the smaller particle diameter ranges as there is a significantly larger number of smaller particles in the distribution. Table 4.3 reproduces the group size definitions. Particle size effects will only be investigated for the rotating and stationary duct at 1050°C to highlight the effects of rotation.

Table 4.3. Particle size group distribution, 'x' represents the particle diameter.

Group Number	Diameter Range (μm)
1	$0.5 \leq x < 3$
2	$3 \leq x < 5$
3	$5 \leq x < 10$
4	$10 \leq x < 20$
5	$20 \leq x < 30$
6	$30 \leq x < 50$
7	$50 \leq x < 75$
8	$75 \leq x < 100$
9	$100 \leq x < 150$
10	$x \geq 150$

The deposition and impact results for each particle size group are presented in Figure 4.32. The deposition or impingement results for each group are normalized by the number of particles that were injected into each respective group. While the deposition results are presented as percentages, the impacts are presented as factors due to their large number. The formulae that determine the y-axis are given in the figures.

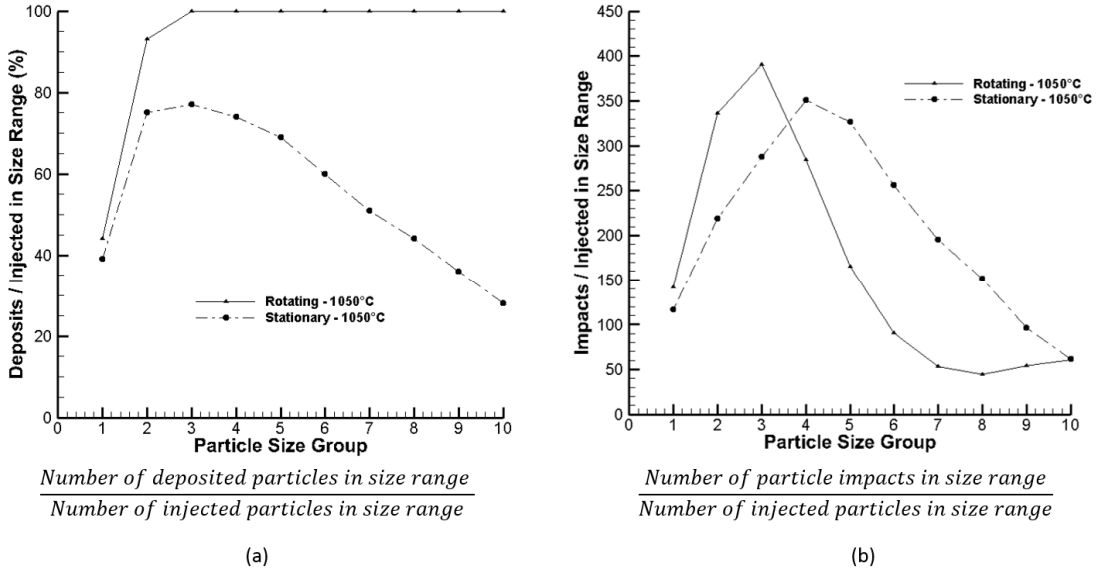

$$\frac{Number\ of\ deposited\ particles\ in\ size\ range}{Number\ of\ injected\ particles\ in\ size\ range}$$

(a)

$$\frac{Number\ of\ particle\ impacts\ in\ size\ range}{Number\ of\ injected\ particles\ in\ size\ range}$$

(b)

Figure 4.32. Particle (a) Deposits and (b) Impacts in each particle size group, normalized by the number of particles injected in the particle size group, for rotating and stationary cases.

Deposition results show that for the rotating case all particle sizes greater that 5 microns deposit by the end of the second pass. As previously noted, the Coriolis force acting on the particles plays a significant role in pushing particles towards the first pass trailing wall where they repeatedly impact the wall and eventually deposit which is driven by the large number of impacts that occur. On the other hand, particles less than 5 microns are not as readily influenced by the action of Coriolis force as are the larger particles and many of them escape from being deposited. Less than 40% of particles smaller than 3 micron deposit which is similar to the deposition calculated in a stationary duct. Conversely, in a stationary duct about 70% of particles between 5 and 10 micron deposit, after which the percentage of particles deposited steadily decreases as the particle size gets larger. Since a majority of the particles in a stationary duct deposit in the bend region, very small particles navigate the bend quite effectively, whereas larger particles with more

kinetic energy tend to impact the end wall at higher velocities and higher angles and escape deposition. Mid-range particle sizes between 3-20 microns are most prone to deposition in the stationary duct.

Figure 4.32b shows that in both static and rotating cases, larger particle size groups have lower impingement levels due to their ability to escape from surfaces quickly. The very small particles are mostly carried by the flow and have limited contact to duct surfaces, whereas the mid-sized particles between 3-20 micron are carried to surfaces, and linger near these surfaces with multiple collisions. It is noted that the relatively large decrease in impacts for the rotating case is due to the larger number of particles that deposit in the larger size ranges and therefore do not remain in the flow long enough to impinge at other locations.

To more clearly present the dominant effect the Coriolis force has in the first pass, the deposits for each group size are presented in Figure 4.33, normalized by the total number of particles injected for each respective group size. Figure 4.33a presents results for the leading and trailing walls of the first pass including the rib surfaces, while Figure 4.33b presents results for deposits on all surfaces in the first pass.

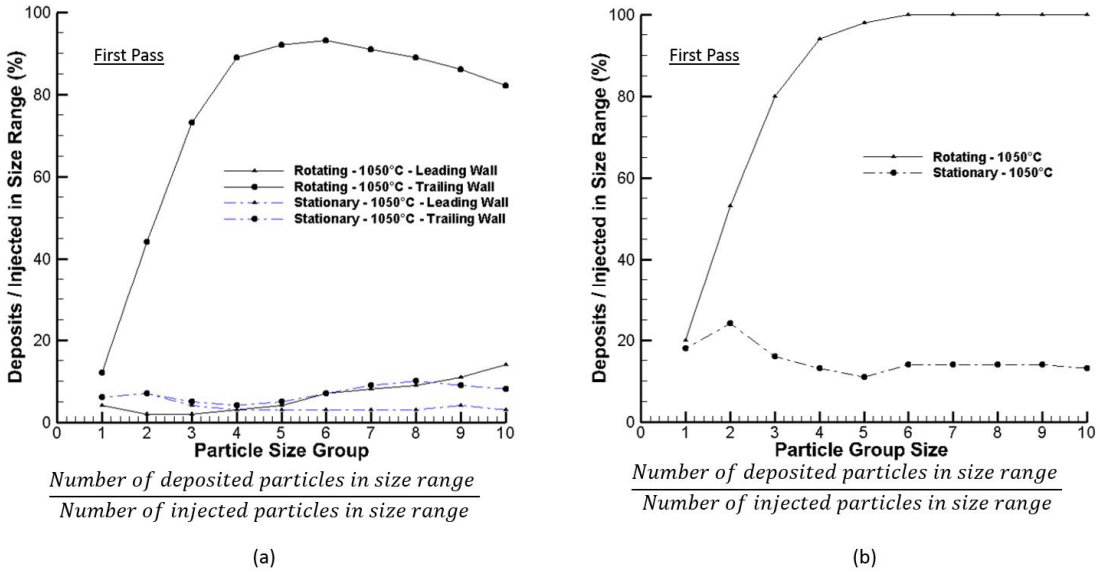

Figure 4.33. Particle deposits in each size group in the first pass, normalized by the number of particles injected in that size group, (a) For the leading and trailing walls (b) For all surfaces, in the rotation and stationary cases.

The deposition predictions in the first pass clearly show that the action of Coriolis force plays a dominant role and causes high levels of deposition on the trailing wall. In the stationary case, the levels of deposition are relatively similar on both the leading and trailing walls for all particle sizes. The high levels of deposition along the trailing wall, has been previously discussed in Figure 4.9 and 4.16, but what this figure shows is that the majority of particles in the larger group sizes have already deposited on the trailing wall before exiting the first pass. To quantitatively compare the rotating and stationary cases in the first pass, 27% of overall deposits within the entire domain occur in the first pass for the stationary case, while 84% of overall deposits occur in the first pass for the rotating case. Over 3 times as many deposits occur in the rotating case in the first pass, which supports the previously made claim that there are significantly fewer number of particles remaining in the flow at the end of the first pass when comparing the rotating case to the stationary. This is also supported by Figure 4.33b which shows that particles above 20μm will all have deposited by the end of the first pass.

Advancing from the first pass, the bend region deposits for each group size normalized by the number of particles injected in each respective group size is presented in Figure 4.34.

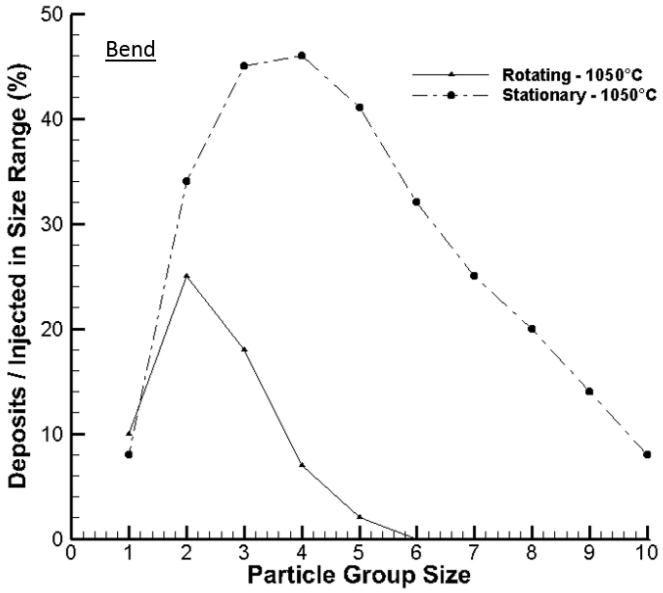

Figure 4.34. Particle deposits in each group size normalized by the number of particles injected in that group size, presented for the bend region with rotating and stationary cases.

Deposition prediction in the bend region shows that for the stationary case there is high level of deposition for particles in the 3-30μm range. This range of particles deposit in the bend in the stationary case because they are not small enough to directly follow the streamlines and avoid impingement. As the flow is being accelerated by the turning of the flow in the bend, the collisions will be at higher velocity and the range of particles mentioned above will not have as high a kinetic energy entering the collision as the larger particle size ranges, making them more likely to deposit where larger particles would rebound off the wall. The increase in deposition in comparison to the rotating case is due to more particles remaining in the flow, as shown in Figure 4.33b. As the bend is dominated by the turning of the flow, Coriolis or centrifugal buoyancy forces are not as prevalent in this region and the flow structure is dominated by the geometry of the bend. It is therefore hypothesized that the physics of deposition should be similar in the rotation case if the same number of particles were entering the bend region as in the stationary case.

To give a spatial map of deposition throughout the domain, the particles remaining in each pitch of the domain are presented in Figure 4.35. The deposition levels are shown for stationary and rotating cases for all wall temperatures simulated.

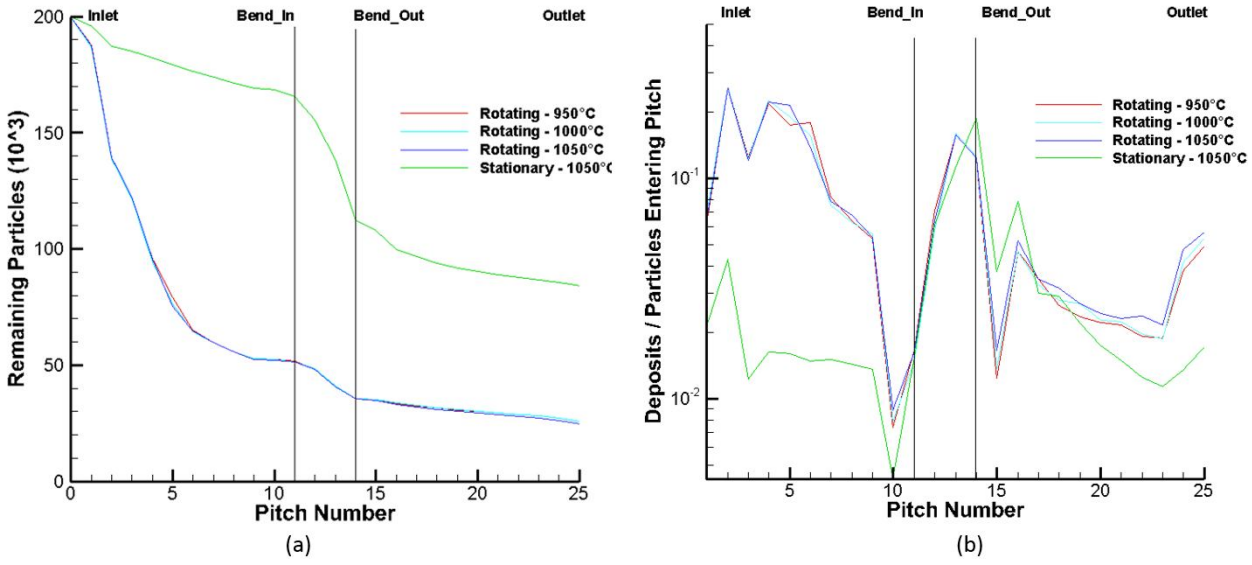

Figure 4.35. (a) Number of remaining particles entering each pitch, (b) Number of deposits in each pitch normalized by particles that entered pitch, for all cases.

The results in Figure 4.35a show the high levels of deposition at the inlet to the duct in the rotating case with about 70% of particles depositing in the first 6 rib pitches. In comparison, in the stationary duct only about 18% deposit in the first pass while about 43% have deposited by the exit to the bend. To desensitize, the deposition trend to the number of particles available for deposition, Figure 4.35b shows the number of deposits per pitch normalized by the number of particles entering the pitch. In the rotating duct approximately 15% of particles entering a pitch deposit in the first six pitches which is considerably higher than the stationary duct. However, in the bend region, deposition in both stationary and rotating cases follow the same trends, once again showing that the particle dynamics in the bend is independent of the Coriolis and centrifugal forces. Deposition dynamics of particles exiting the bend are fairly similar between the stationary and rotating cases for the first few pitches, but deviate after the first three pitches as Coriolis forces start having an effect on particle trajectory and push them towards the leading wall. However, the differences are not as stark as in the first pass.

The results for the three rotating cases show similar results for deposition with varying wall temperature. This was unexpected as a larger deposition dependence on wall temperature would be theoretically supported and was also presented in the previous investigation by Singh and Tafti [54]. However, the previous investigation by Singh and Tafti [54] used a Reynolds number of 25,000, which is relatively low compared to the Reynolds number of 100,000 used in the current investigation. It is reasoned that because of the higher Reynolds number, the fluid heats up less and for that reason the bulk temperature remains well below temperatures that would influence particle viscosity sufficiently to precipitate deposition. While more heat is carried by the fluid from the wall at a higher Reynolds number to compensate the higher flow rate, assuming a similar augmentation ratio, the residence time of the fluid in the duct is about 4 times less leading to a lower fluid temperature.

Predictions of the particle temperature, in support of this conclusion, can be seen in Figure 4.36, which presents the average particle temperature recorded for the collisions. Results are presented for stationary and rotating ducts with a wall temperature of 1050°C. For reference, the fluid and particles are introduced into the domain at 527°C.

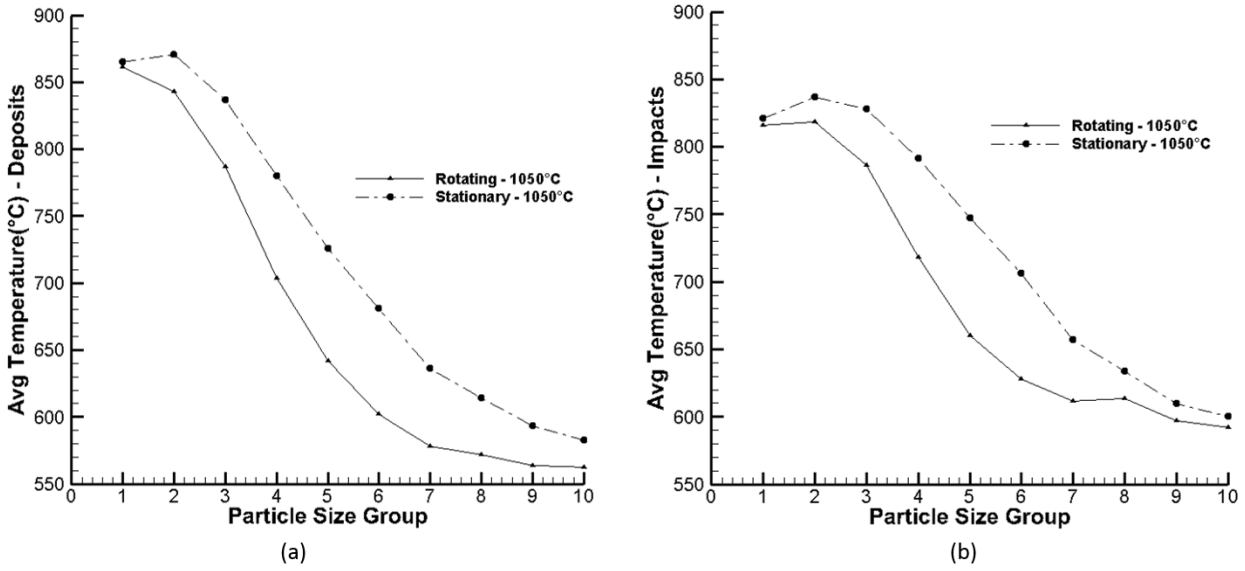

Figure 4.36. Average particle temperature (°C) when (a) Depositing or (b) Impinging on surface, for rotating and stationary domains.

Impingement and deposition temperatures range from 570ºC to 870ºC. The smaller sized particles tend to heat up quickly due to a smaller time constant and larger particles take longer to reach the same temperature because of their increased mass. Additionally, larger particles may not have a large residence times in the near surface fluid layer as much as the smaller particles. The higher temperature of particles in the stationary duct result from the fact that most of the impacts and deposition occur in the bend region, allowing the particles a larger residence time and also due to the fact that most impacts and deposition in the rotating duct occur in the first pass at the trailing wall with low residence times. Also the particles are subject to lower fluid temperature near the trailing wall because of the higher heat transfer coefficients at the trailing wall as discussed in Chapter 3. From Figure 4.3, it can be concluded that contribution to deposition probability by the critical viscosity model is miniscule and thus the majority of depositions are a result of the probability imposed by the coefficient of restitution model in Figure 4.6.

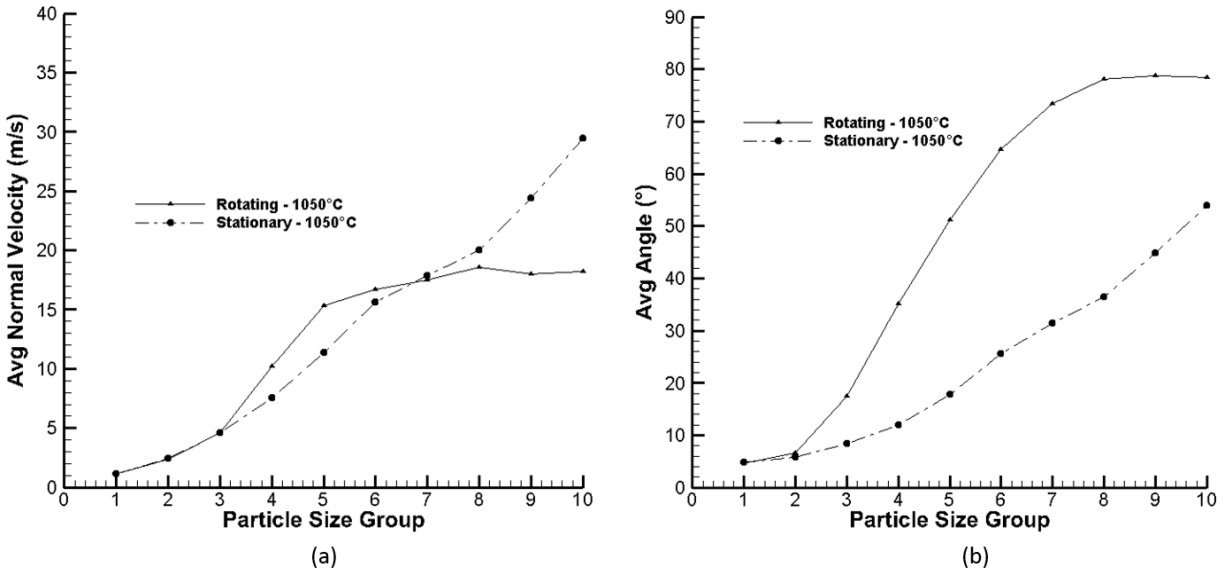

Figure 4.37. Average impact (a) Normal velocity, (b) Angle (°), for deposited particles, for rotating and stationary domains.

Since the majority of depositions are driven by the coefficient of restitution model probability, the average impacting velocity and angle of depositing particles are examined in Figure 4.37 for the stationary and rotating ducts at 1050°C. Both the average impact velocity and average angle increase with particle size. The average deposition velocity ranges from 1 m/s to about 25 m/s in the stationary as well as the rotating case. The larger particles typically carry more momentum and do not have enough residence time in the near surface layer to slow down substantially, whereas the smaller particles have a low momentum-transfer time constant and are prone to reach near-equilibrium with the low velocity fluid near surfaces. While the deposition velocity does not differ substantially between the two cases, the average deposition angle is much higher in the rotating channel. This is because with rotation, many depositions occur at the first pass trailing wall rib faces with head on collisions at high impact angles, while not as many particles deposit on the rib faces in the stationary duct.

4.4 Conclusions

Large-Eddy Simulations with a wall model are conducted in a two-pass ribbed duct at a Re=100,000 under stationary and rotating conditions at Ro=0.2, Bo=0.5 to investigate the transport of ingested sand in

ribbed ducts. Sand particle sizes up to 175 microns are investigated in a distribution with 65% of the sand particles below 10 microns. Impact and deposition characteristics of sand are investigated by analyzing the results from the simulations.

In the first pass, rotation results in much higher levels of impingement and deposition along the trailing wall in comparison to the leading wall and the stationary duct leading and trailing walls. This is due to the action of Coriolis forces which push the particles towards the trailing wall on entry into the rotating duct resulting is a high level of interaction with the trailing duct surface and ribs. Because of repeated impacts (on average each injected particle undergoes about 200 impacts with surfaces in the duct) in this region, deposition levels are high with roughly 0.5% of the impacting particles depositing. It was observed that a majority of particles injected in the rotating cases are unable to escape the first three rib pitches on the trailing wall. This is due to the particles losing energy over multiple impacts and finally depositing. As a result of this about 84% of the particles deposit in the first pass compared to only 27% in the stationary duct. This results in significantly fewer particles remaining in the domain after the first pass in the rotating cases. This results in lower impingement and deposition throughout the bend and on the smooth side walls. It is shown that if a similar amount of particles in the rotating cases were able to enter the bend as in the stationary cases, there would be similar levels of deposition in the bend.

It is found that temperature effects in the range of wall temperatures from 950-1050ºC had no significant effect on deposition because the particle temperatures remained below 900ºC, much below the softening temperature of 1120 ºC to have any significant impact on the deposition dynamics. Thus most of the deposits are theorized to be caused by multiple collisions which eventually lead to deposition, if only by the sheer number of impacts and the probability that a tiny fraction of these impacts will lead to conditions favorable for deposition.

Chapter 5

Summary and Conclusions

In this thesis, the effects of high speed rotation on the fluid motion and particle transport in the ribbed ducts of internal cooling ducts were investigated. Rotation induced Coriolis forces and centrifugal buoyancy forces caused by temperature gradients and density stratification were investigated using variable property Large-Eddy Simulations (LES) at Re=100,000, rotation number, Ro = 0.2 with Buoyancy parameter Bo = 0, 0.5 and 1.0.

Results from the independent investigation of Coriolis and centrifugal buoyancy forces showed that the hydrodynamic and heat transfer predictions, under both stationary and rotating conditions (only Coriolis force), showed good agreement with available experimental data. Results from the centrifugal buoyancy investigation showed that in the first pass, centrifugal buoyancy had a greater effect in augmenting heat transfer at the trailing wall than in attenuating heat transfer at the leading wall. On contrary, it aided heat transfer in the second half of the first pass at the leading wall by energizing the flow near the wall. Contrary to phenomenological arguments, inclusion of centrifugal buoyancy augmented heat transfer over Coriolis forces alone on both the leading and trailing walls of the second pass.

Particle ingestion into these ribbed duct internal cooling geometries was also investigated to explore a major area of concern in the gas-turbine industry. The objective of this section was to numerically simulate sand transport in a ribbed cooling duct domain and to predict whether sand particles would deposit when coming into contact with surfaces of the duct. 200,000 particles in the size range of 0.5-175μm were injected into the domain with their motion, impingement, deposition, and impact characteristics measured as they move through the domain. The deposition model was an improvement to previously used models as an improved COR prediction method was used to account for incoming velocity/angle by including elastic, elastic-plastic, plastic deformation and adhesion forces during impact. In conjunction with this COR model, a composition dependent viscosity model was used to predict how temperature variations of the particle, as it collided with a surface, played a role in determining

deposition. To investigate the effects on particle transport, stationary and rotating domains were simulated with different wall temperatures (950, 1000, 1050°C).

Results from the particle transport investigation showed a large increase in deposition in the rotating duct when compared to a stationary duct. This was concluded to be a result of the particles in the rotating cases interacting more directly with the trailing wall, whereas the stationary domain allowed particles to remain in the mean flow where they were able to gain momentum. The variation of wall temperatures caused little to no change in deposition levels. This was concluded to be a result of the high Reynolds number used in the flow. At high Reynolds numbers, the convective effects dominated the flow and particle motion, meaning the particles have a short residence times in the internal cooling circuit not allowing the particles to heat up to the wall temperature.

Future work should consider using a variation of the COR related deposition model. As the modeled COR forms the basis of calculating the probability of deposition, particles with low COR but with considerable residual energy could exhibit a high probability of deposition when in reality they could still escape deposition. This could particularly impact larger particles which might have a low COR but a low probability of depositing on the surface. Instead, a threshold rebound velocity or kinetic energy calculated from the COR could be used to calculate the probability of deposition.

Appendix A

Nomenclature

Bo	Buoyancy number
C_D	Drag coefficent
c_p	specific heat capacity
COR	coefficient of restitution
d^+	normal distance from wall
D_h	hydraulic diameter
DNS	Direct Numerical Simulation
e	rib height
h_c	convective heat transfer coefficient
h_r	radiative heat transfer coefficient
LES	Large-Eddy Simulation
L_{ref}	reference length (D_h)
L_x	periodic domain length (Ch. 3)
$\vec{n}$	unit normal vector
Nu	Nusselt number
Nu_0	Dittus-Boelter Nusselt number
p	pressure
P	pitch distance
Pr	Prandtl number
$q"$	heat flux per unit area
Q_x	flow rate in x-direction
R	gas constant $\left(287 \frac{J}{kg*K}\right)$

$\overrightarrow{r_1}$	distance from axis of rotation to cooling channel inlet
$RANS$	Reynolds Averaged Navier-Stokes
Re	Reynolds number
Ro	Rotation number
St	Stokes number
t	time
$\vec{t}$	unit tangential vector
T	temperature
T_0	non-dimensionalizing temperature scale
TKE	turbulent kinetic energy
$\vec{u}$	Cartesian velocity vector
$\vec{x}$	Cartesian direction vector

Greek

β	mean streamwise pressure gradient (periodic boundary condition)
ε	emissivity coefficient
ω	rotational speed (rad/s)
η	efficiency
γ	mean streamwise temp. gradient periodic boundary condition
μ	molecular viscosity
ρ	density
θ	dimensionless temperature $(T^* - T_{in}^*)/(T_w^* - T_{in}^*)$
κ	thermal conductivity
κ^+	von Karman constant
σ	Stefan-Boltzmann Constant
τ	shear stress

φ	periodic temperature fluctuation
λ	particle time scale
$\vec{\xi}$	logical/computational coordinate vector
Ω_s	periodic heat transfer surface area
ν	Kinematic viscosity

Subscripts/Superscripts

*	dimensional quantity
area	non-dimensional area ($10^{-10}\ mm^2$)
b	bulk
cap	capture
conv	convective
COR	coefficient of restitution
dep	deposit
eq	equivalent
f	fluid
imp	impact
in	inlet value
inj	injected
m	mix-mean
p	particle
rad	radiation
ref	reference value
T	temperature
t	tangential
τ	turbulent quantity

visc	viscous sticking
w	wall

Appendix B

Fully Developed Flow and Heat Transfer Validation

In order to accurately validate the numerical methods presented previously for hydrodynamic, thermodynamic, and particulate motion in a domain, a single pitch ribbed geometry is used to reduce complexity and computational cost. A periodic boundary condition, in the flow direction, is used and by doing so an infinite number of successive ribs is simulated. The geometry consists of two inline ribs, oriented normal to mean flow direction. Four cases are presented here for this geometry. Case 1 consists of a stationary geometry with a Reynolds number of 20,000 and results are presented for both hydrodynamic and heat transfer levels, predictions are compared to experimental work by Rau et al. [37]. Case 2 presents a rotation case ($Ro = 0.34$) of the same geometry and Reynolds number. As a constant property assumption is made here, there is no centrifugal buoyancy force included in numerical prediction of results. Case 3 and 4 are simulations at the same rotation number and Reynolds number but with the inclusion of particles. Investigation of these two cases compares two particle sizes, 10 micron and 50 micron. Results are presented for prediction of particle impingement on all surfaces exposed to the main flow. No heat transfer is considered in cases 3 and 4 and therefore deposition levels are not investigated here. These four cases validate the hydrodynamic and heat transfer results in ribbed geometries with experimental results, as well as particulate transport, which is compared with previous studies.

Computational Domain -

Presented in Figure B.1, the computational domain consisting of a single pitch with inline, orthogonal ribbed duct geometry and corresponding coordinate system. The rib pitch to rib height ratio, (P/e), is 10 and the rib height to hydraulic diameter ratio, (e/D_h), is 0.1. Flow is simulated under a fully developed assumption at a Reynolds number of 20,000. As mentioned previously, a periodic boundary condition is applied in the streamwise direction, represented as the x direction. Details about implementation of a periodic condition were given in Chapter 2.2. All walls exposed to fluid are heated with a constant heat flux condition and have a no-slip boundary condition. Simulation is performed for approximately 20 flow

through time units with the last 20 time units calculating mean and turbulent statistics. In cases 3 and 4, particle-wall collision statistics are also taken during the last 20 time units.

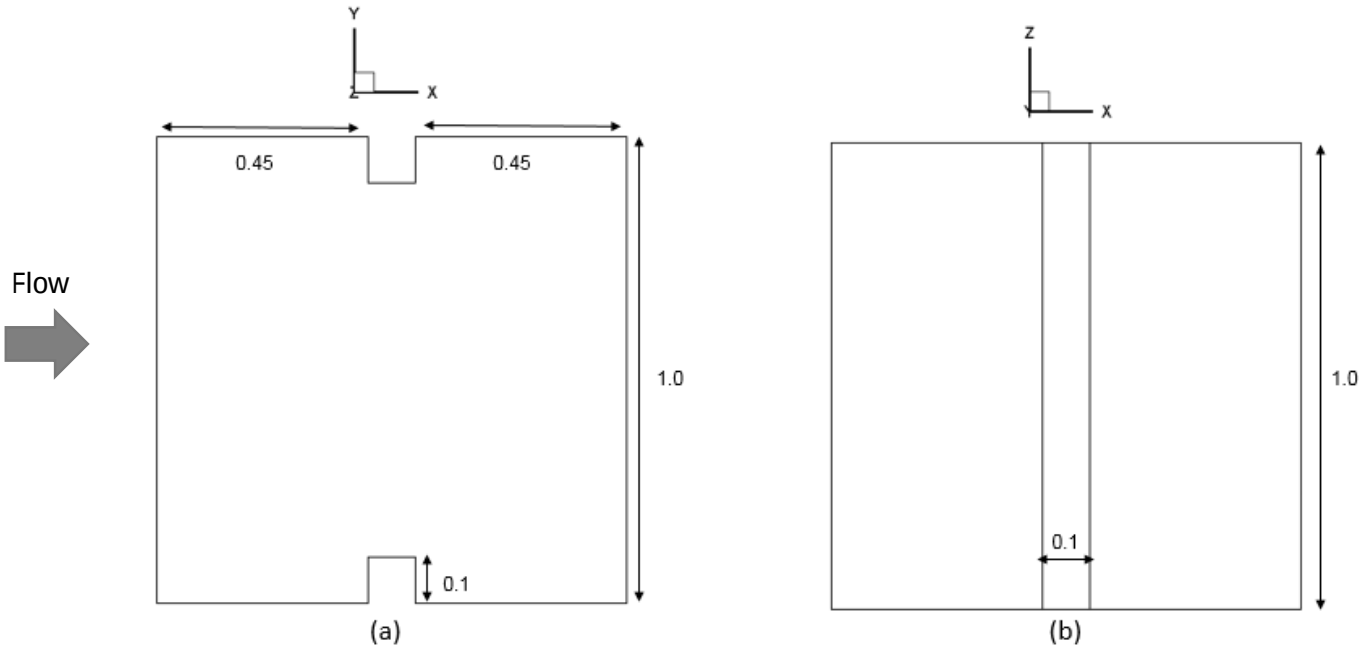

Figure B.1. Computational Domain (a) Front view of domain (b) Cross section of domain, both Z and Y directions are coming out of the page in (a) and (b), respectively.

The geometry is made up of approximately 1.8 million computational cells distributed over 40 blocks. The grid point distance nearest the wall is $2.4\ x\ 10^{-3}$ which gives a y^+ value from 3 to 5. The grid is refined around the rib and wake regime to support the prediction as the flow becomes separated and forms recirculation zones downstream of the rib. Simulation is conducted using wall-resolved LES.

Results and Discussion –

Case 1: Flow and heat transfer validation for stationary ribbed duct

Mean flow streamline results are presented in Figure B.2. Results are presented along the center line or symmetry plane (Z=0.5) and for half of the domain in the Y direction as the domain is symmetric. Flow is moving from left to right. Results show a primary recirculation region downstream of the rib and results show a reattachment point approximately 3.5*e* downstream of the rib.

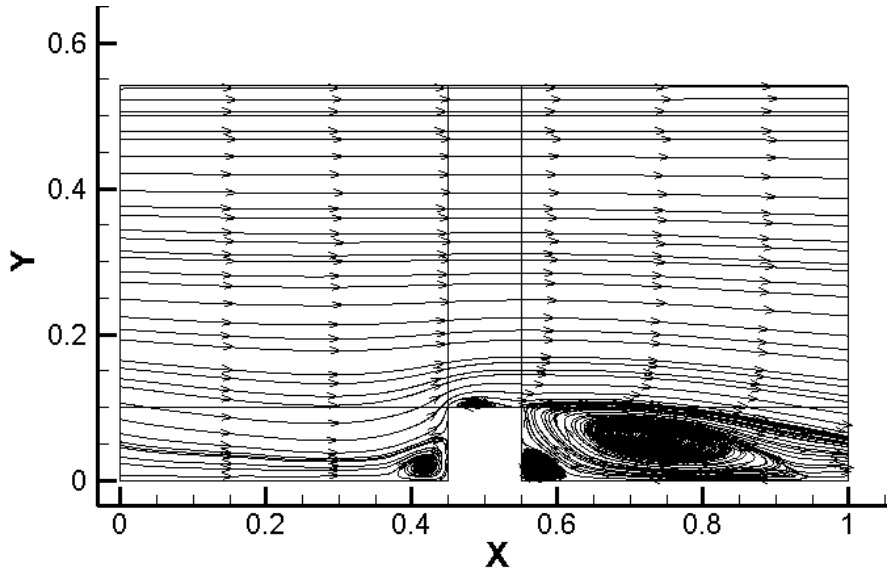

Figure B.2. Mean flow streamline distribution for Ro=0.0 in the symmetry plane (Z=0.5).

First validation of the hydrodynamic and heat transfer prediction is presented for the numerical model for ribbed duct geometries. Results are validated with experimental data from Rau et al. [37], where a Reynolds number of 30,000 is used and a P/e of 9 is used for comparison with the current stationary case. These reference parameters are not exactly replicated but nevertheless provide a good basis for comparisons.

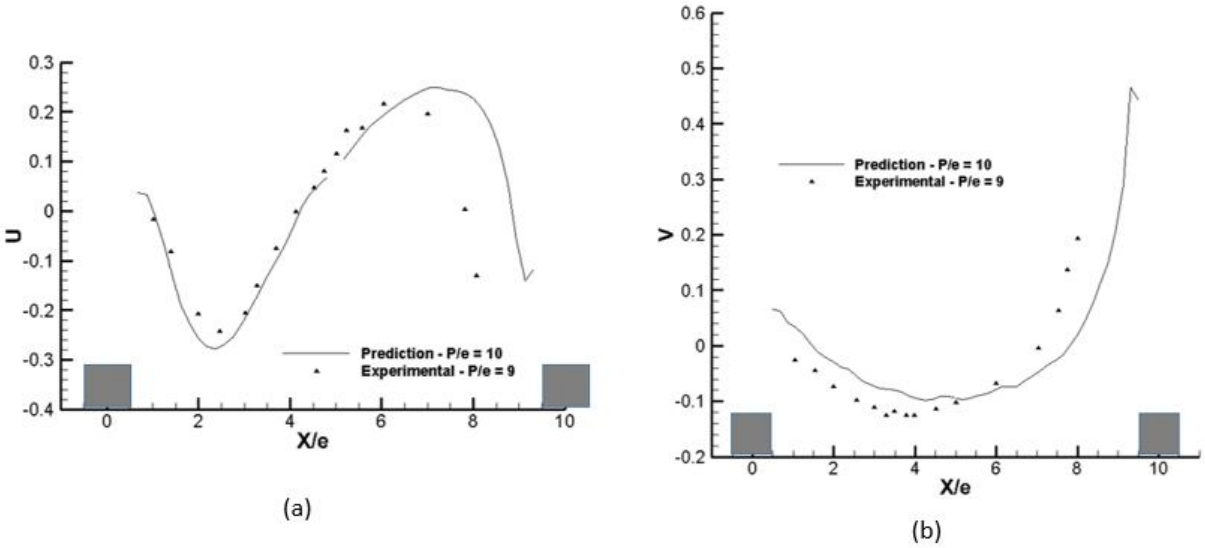

Figure B.3. Mean flow in symmetry plane, comparison to Rau et al. [37] (a) Steamwise velocity at *Y/e* =0.1 and (b) Spanwise velocity at *Y/e* = 1, dark squares represent rib locations.

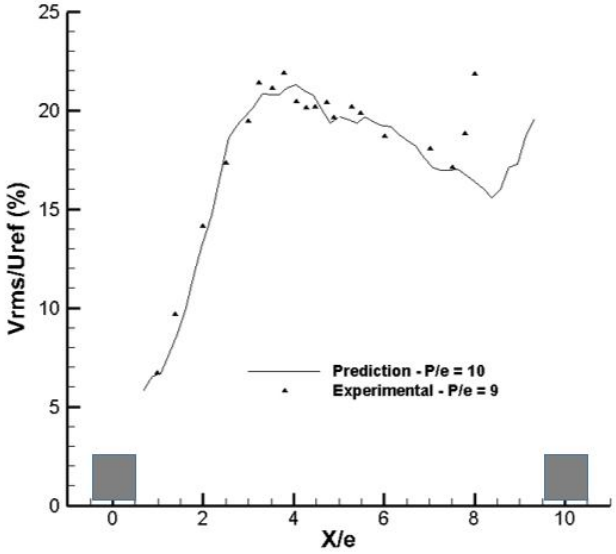

Figure B.4. Turbulent fluctuation as a percentage of the bulk velocity comparison to Rau et al. [37], results shown in the symmetry plane at a *Y/e* of 0.3, the dark squares represent rib placement.

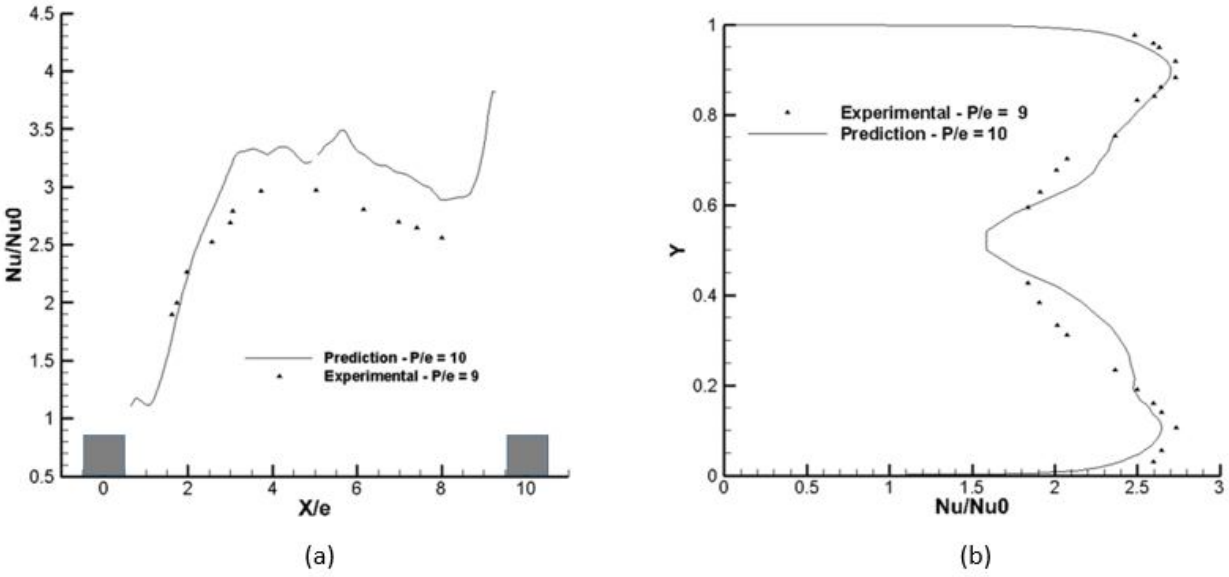

Figure B.5. Nusselt number augmentation ratio to Rau et al. [37], Heat transfer prediction along (a) Centerline of ribbed wall (Y=0), (b) Smooth side wall (Z=0) at *X/e* = 3.5.

Where, Nu_0 is defined as the reference Dittus-Boelter correlation, as given in Chapter 2.4. Detailed discussion of flow structures and heat transfer augmentation in a stationary, periodic, ribbed duct geometry can be found in Tafti [36].

<u>Case 2:</u> Investigation of hydrodynamics and heat transfer levels in a rotating duct

With the model being validated for both the hydrodynamic and heat transfer levels in the stationary domain, rotation predictions are now presented. The geometry is given a rotation (*Ro* = 0.34) around the z-axis in the counter-clockwise direction (reference Figure B.1 for coordinate system), defining the leading wall as the top wall (Y=1) and the trailing wall as the bottom wall (Y=0). Detailed discussion of the effects of Coriolis forces in a pitch of a ribbed duct can be found in Abdel-Wahab [57].

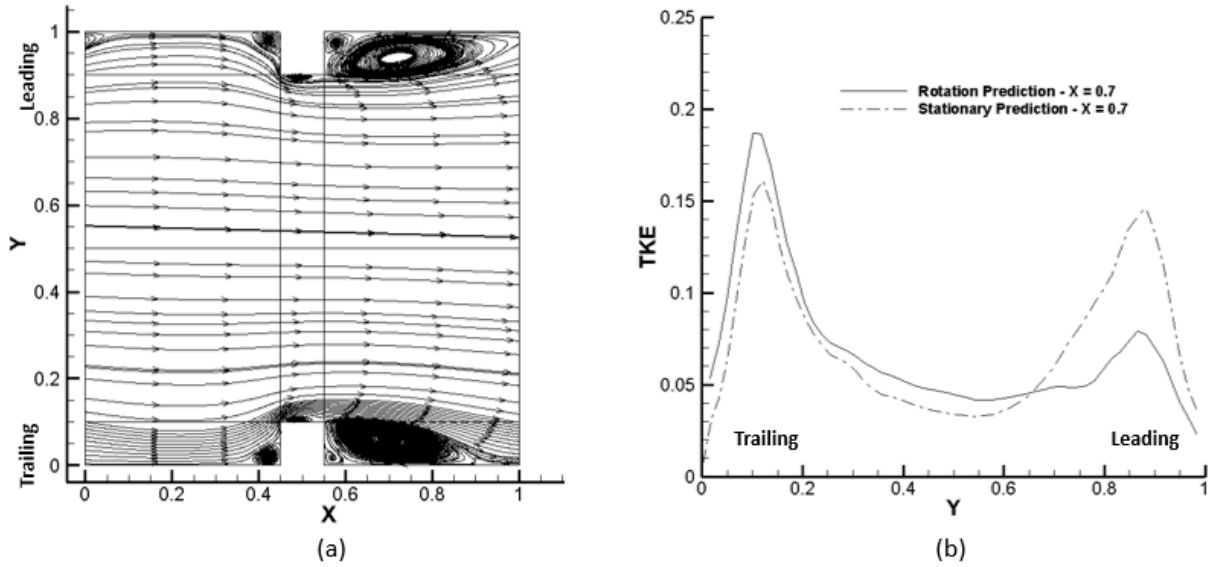

Figure B.6. (a) Mean flow streamlines presented at the symmetry plane (Z=0.5) demonstrate effects of rotation on reattachment point on leading and trailing walls (b) Turbulent kinetic energy [TKE=$(\overline{u'^2} + \overline{v'^2} + \overline{w'^2})/2$] for rotation and stationary, presented at symmetry plane and X=0.7.

The secondary flow that is generated by rotation is now investigated. Results shown in Figure B.7 are for the mean vertical and lateral velocity components at a location *X/D* = 0.5 and are presented by two symmetric halves. Figure B.8 plots the lateral turbulence intensity (w_{rms}).

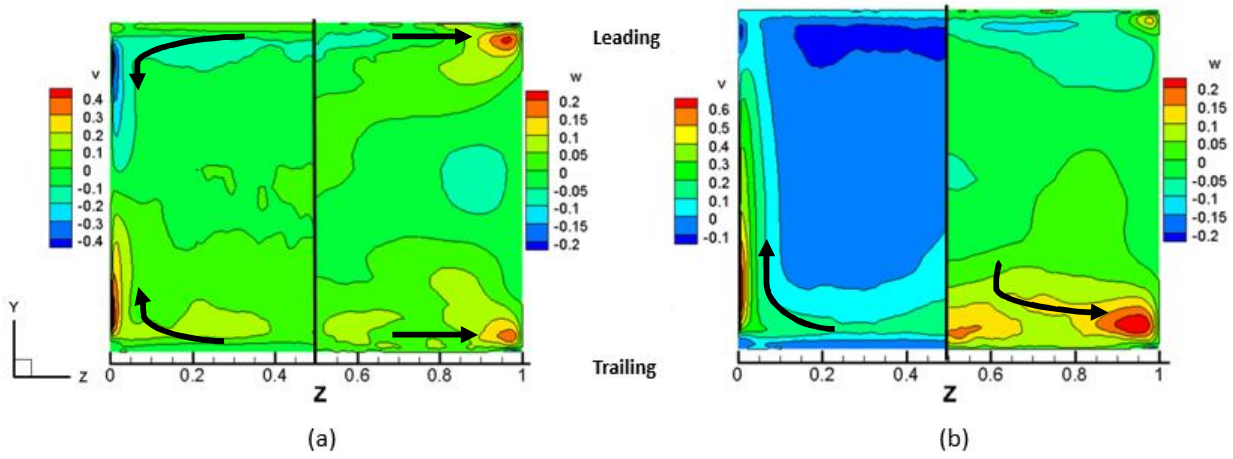

Figure B.7. Mean velocity contours (a) Stationary vertical (left) and lateral velocity profiles (b) Rotating, vertical (left) and lateral velocity profile shown at X=0.5 in symmetry plane. Strong secondary flow prediction in rotating cases, from center to the side wall near trailing wall and from trailing wall to leading wall along side wall.

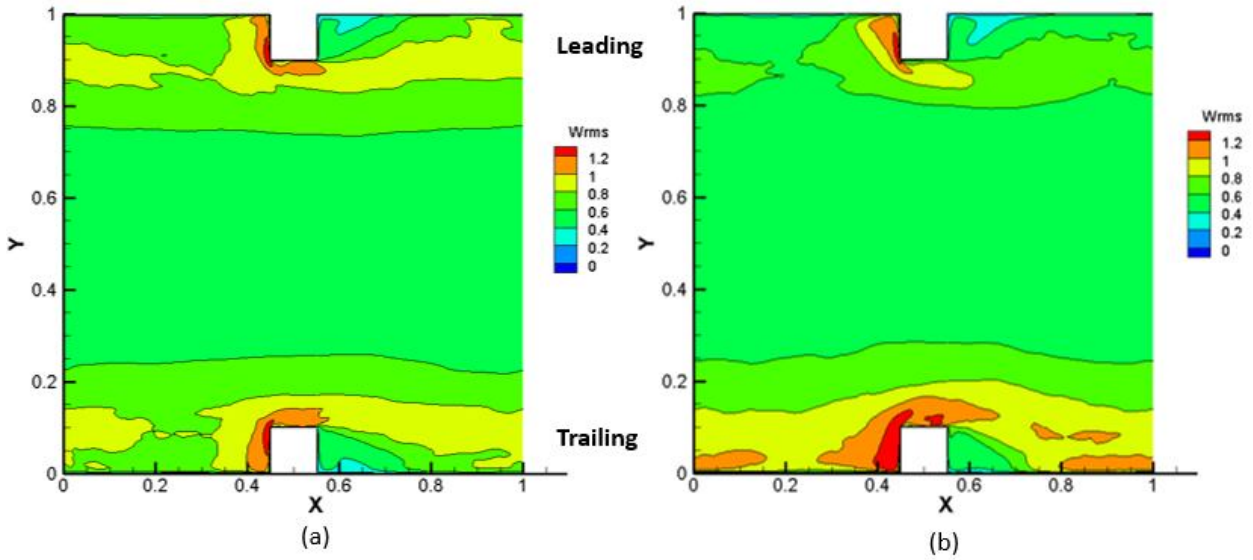

Figure B.8. Lateral turbulence intensity, w_{rms}, contour comparison (a) Stationary results, (b) Rotating results, shown at the symmetry plane. Increase in lateral turbulence intensity for rotating case near trailing wall, transporting flow from center to side walls.

With the hydrodynamic analysis completed for the addition of Coriolis forces to a stationary domain, the heat transfer in the rotating domain is now investigated. Figure B.9 represents Nusselt number augmentation ratios for stationary and rotating cases. The results are presented for the ribbed walls, downstream of the rib (X from 0.55 to 1.0).

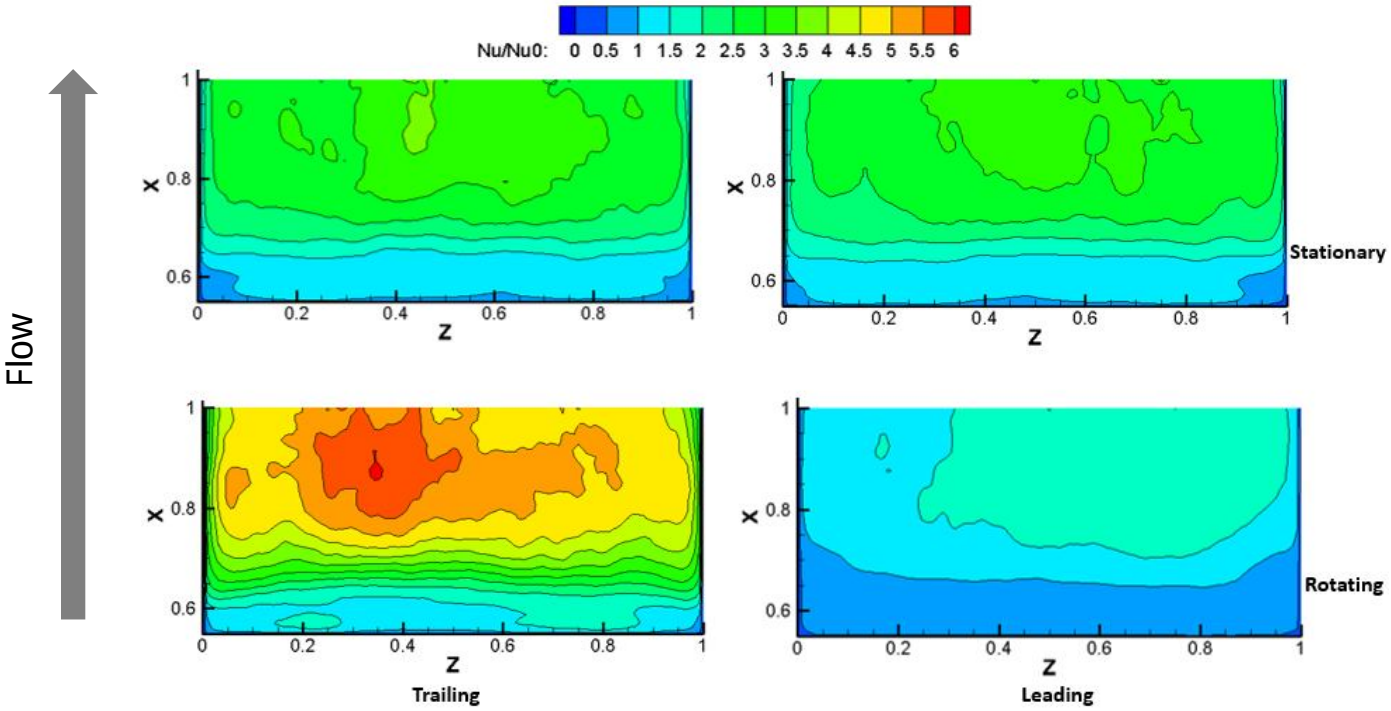

Figure B.9. Nusselt number augmentation ratio of leading and trailing walls in the recirculation zone of the rib (0.55 < X < 1.0), results are presented for both the stationary and rotating cases. Results show heat transfer augmentation and attenuated levels on the trailing and leading sides of the rotating duct, respectively.

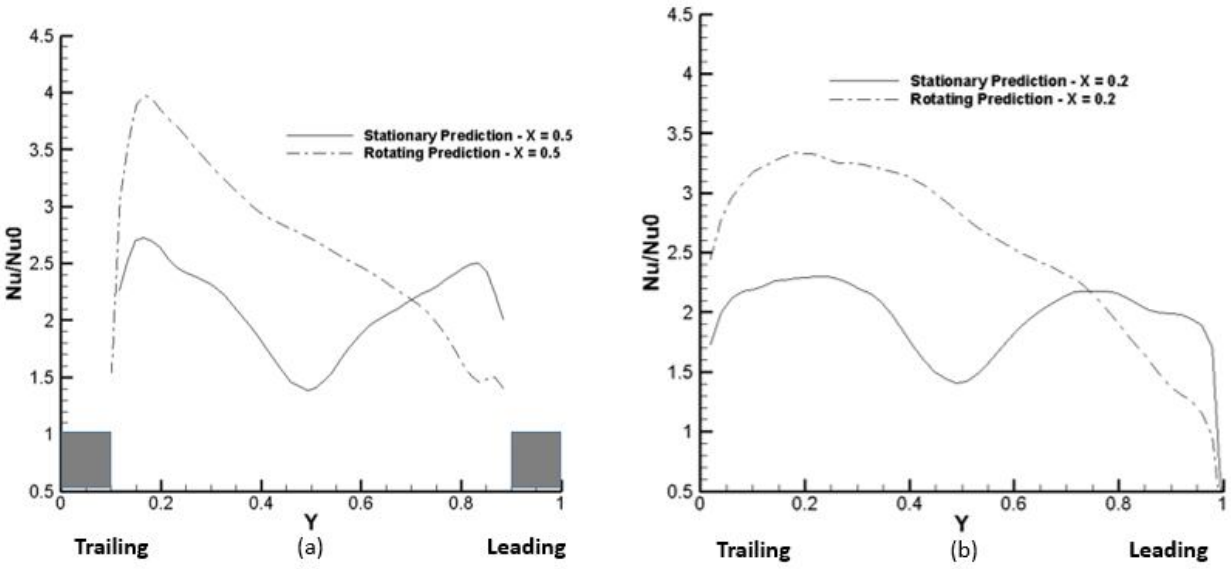

Figure B.10. Nusselt number augmentation ratio for smooth side wall (Z=0) (a) At location X = 0.5 (b) At location X = 0.2, the dark squares represent rib locations. Showing heat transfer augmentation near the trailing wall on the side wall.

To conclude the heat transfer discussion, the rib face will be investigated. Results are presented for the surfaces exposed to the mean flow (front, top, back). The ribs are examined as these locations are where the highest points are heat transfer are obtained in the domain. For comparison purposes the ribs on the leading and trailing side of the rotating geometry will be compared with those of the stationary case.

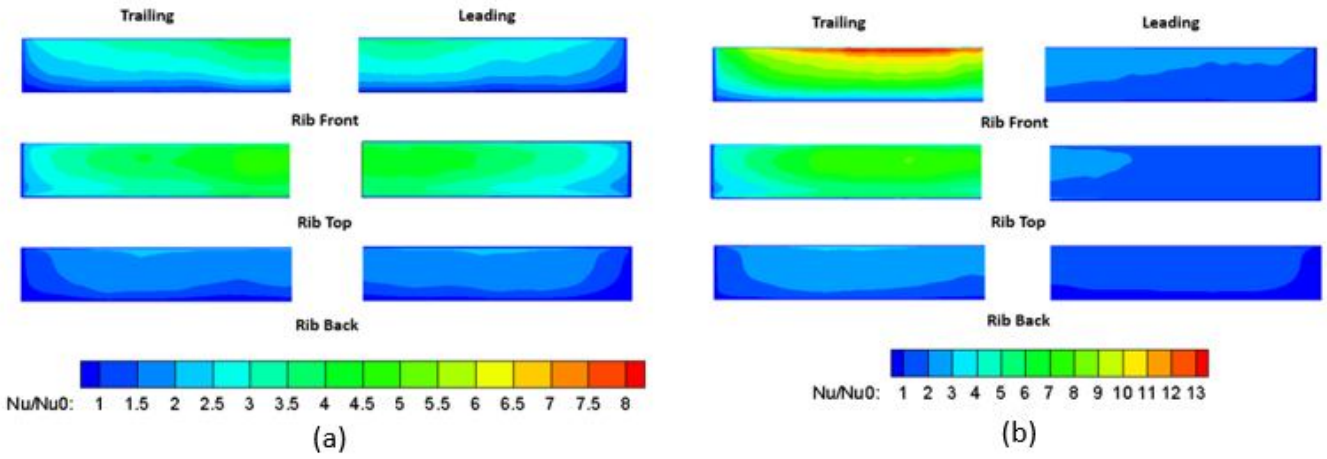

B.11. Nusselt number augmentation ratio for the leading and trailing rib surfaces (a) Stationary geometry (b) Rotating geometry, note legends are not similar for (a) and (b).

<u>Case 3 & 4</u>: Particulate transport and impingement in rotating duct

Case 3 and 4 deal with the addition of particulates into the domain and as the only difference between the two cases is the diameter of particulate used, the presentation of results is combined here. The size of the particle is of importance because the differently sized particles will transport differently based on the particle Stokes number (St_p). The 10μm and 50μm particles having St_p equal to 0.07 and 1.72, respectively. The particle transport is predicted as discussed previously in Chapter 2.5. By establishing how particulates behave in a single pitch ribbed geometry, general prediction trends will be beneficial when examining more complex simulations. Detailed discussion of these results can be found in Shah and Tafti [13].

The instantaneous particulate distribution in the channel, at the end of the simulation, in the vicinity of a wall is presented in Figure B.12. The results represent the effects on particle transport from the particle Stokes number and the secondary vorticity formation due to rotation. Quantitatively, 66% of the 10μm particles and 95% of the 50μm particles are in the wall region. Large concentrations near the smooth side walls are shown qualitatively. Also presented with particle impingement results on the walls of the domain.

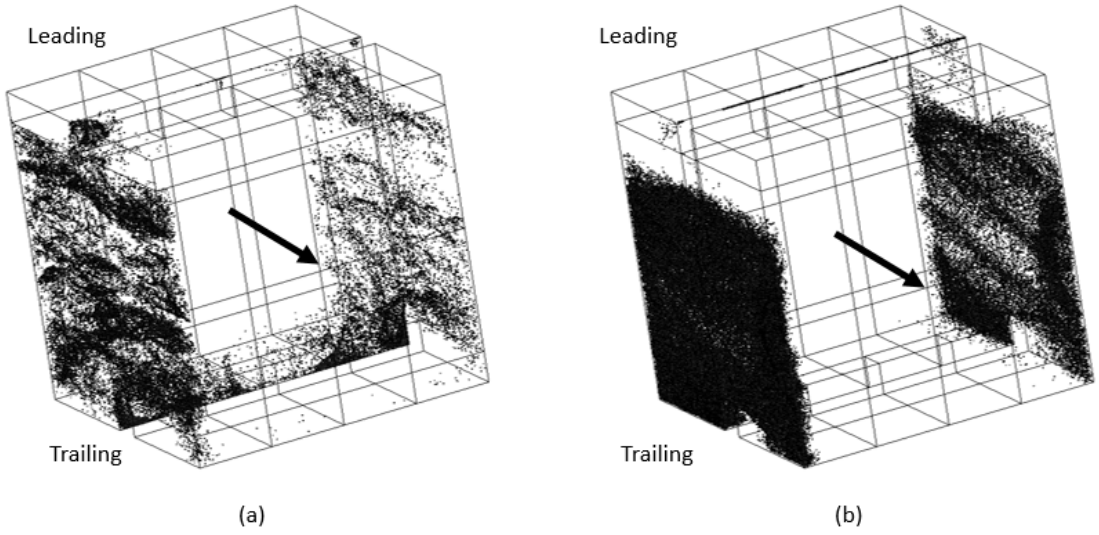

Figure B.12. Instantaneous distribution of particles in vicinity of walls, (a) 10μm, (b) 50μm.

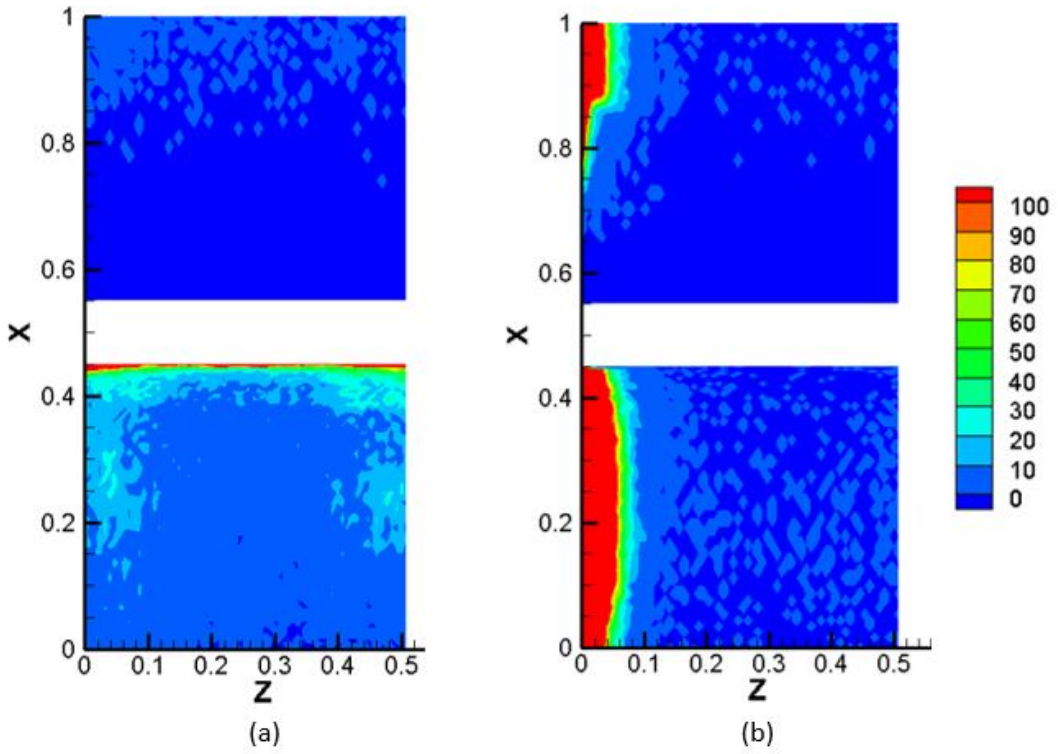

Figure B.13. Particle impingement characteristics on the trailing ribbed wall (Y=0) for (a) 10µm, (b) 50µm, particle sizes for half of symmetry plane. Showing greater 50µm particle impingement near the smooth side wall

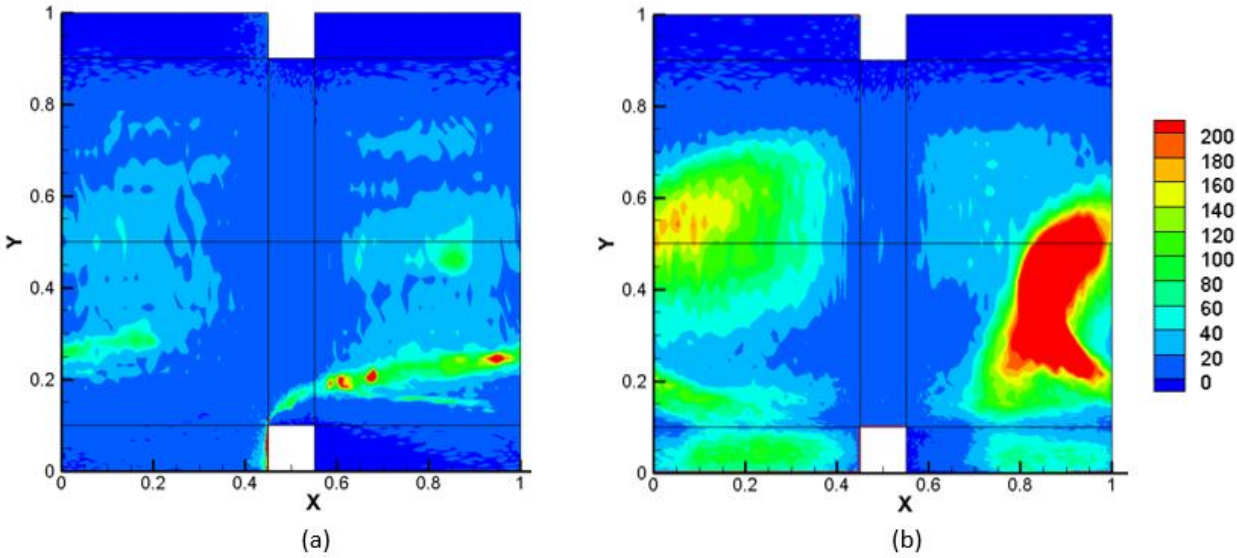

Figure B.14. Particle impingement characteristics on the smooth side wall (Z=0.0) for (a) 10µm, (b) 50µm.

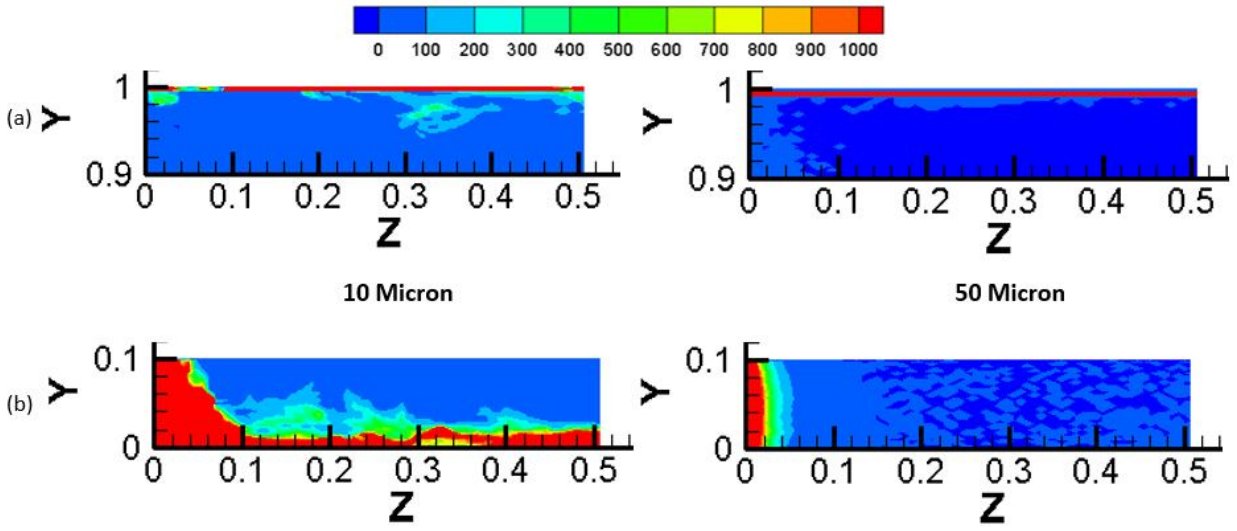

Figure B.15. Particle impingement characteristics on front face (X=0.45) of (a) Leading, (b) Trailing, rib faces for 10 and 50 micron particles.

Appendix C

Additional Validation of Numerical Model for Full U-Bend Geometry

Presented below are additional validation plots for the numerical model used in the simulation of rotating and stationary cases. The results presented are for mean flow and turbulence levels within the U-Bend domain as shown by the locations specified in Figure C.1 in the symmetry plane (Z=0.5). As no experimental data is given for centrifugal buoyancy, the results presented here are with Coriolis forces only. Experimental data from Iacovides et al. [2] is used for validation purposes, with experimental hydrodynamic uncertainty of ± 2% of the mean velocity. As results in both passes and bend of the domain are presented, inner and outer walls are classified instead of using the traditional leading and trailing walls.

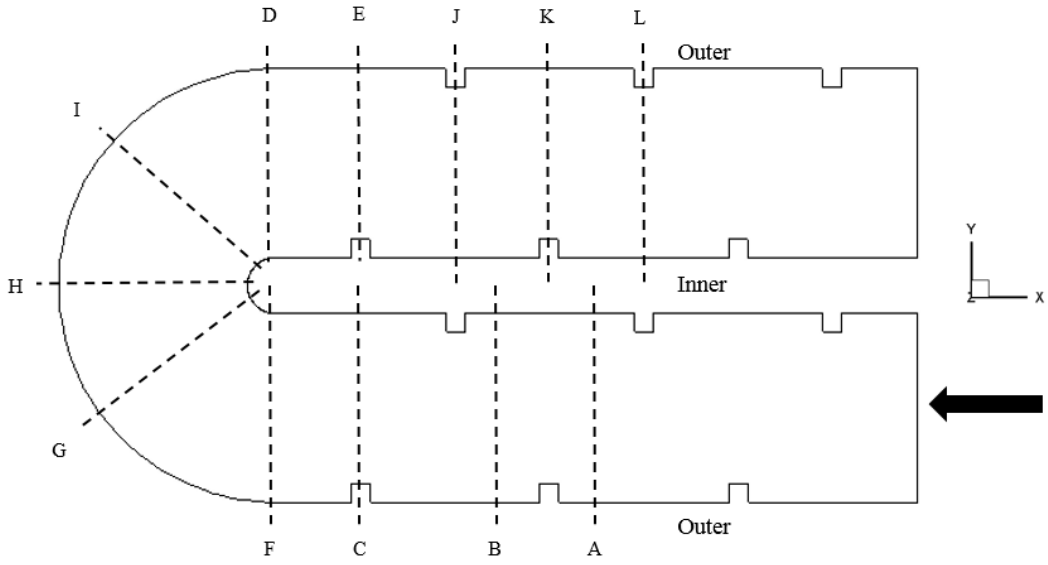

Figure C.1. Reference locations for presentation of results.

Stationary Validation of Results –

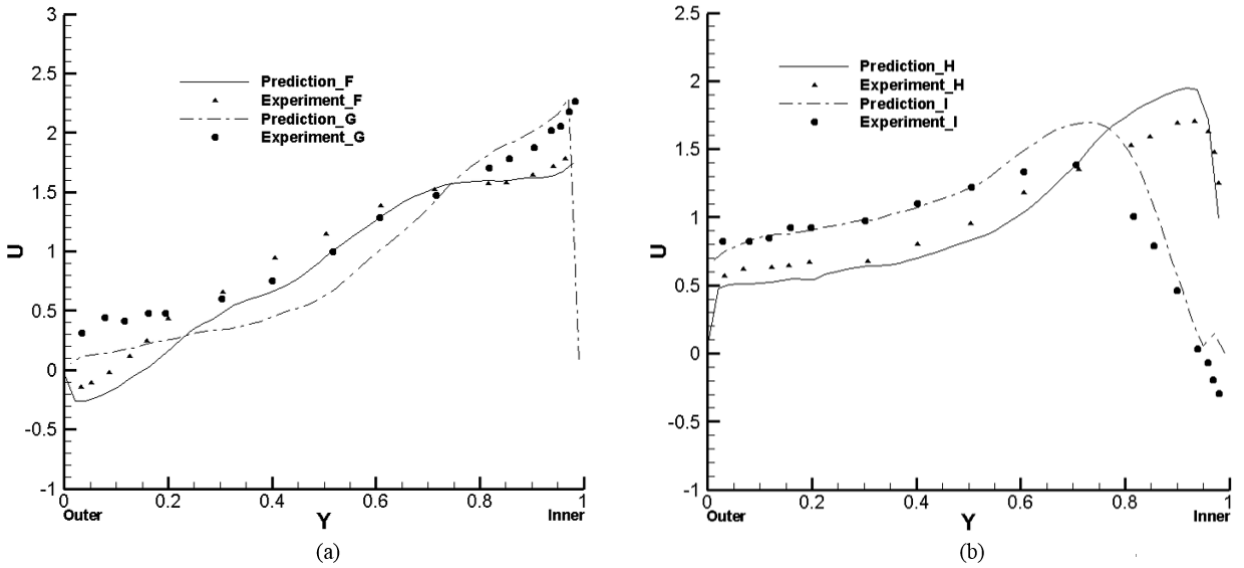

Figure C.2. Mean streamwise flow velocity distribution at locations, (a) F and G (b) H and I, across duct height for Ro=0.0, Bo=0.0.

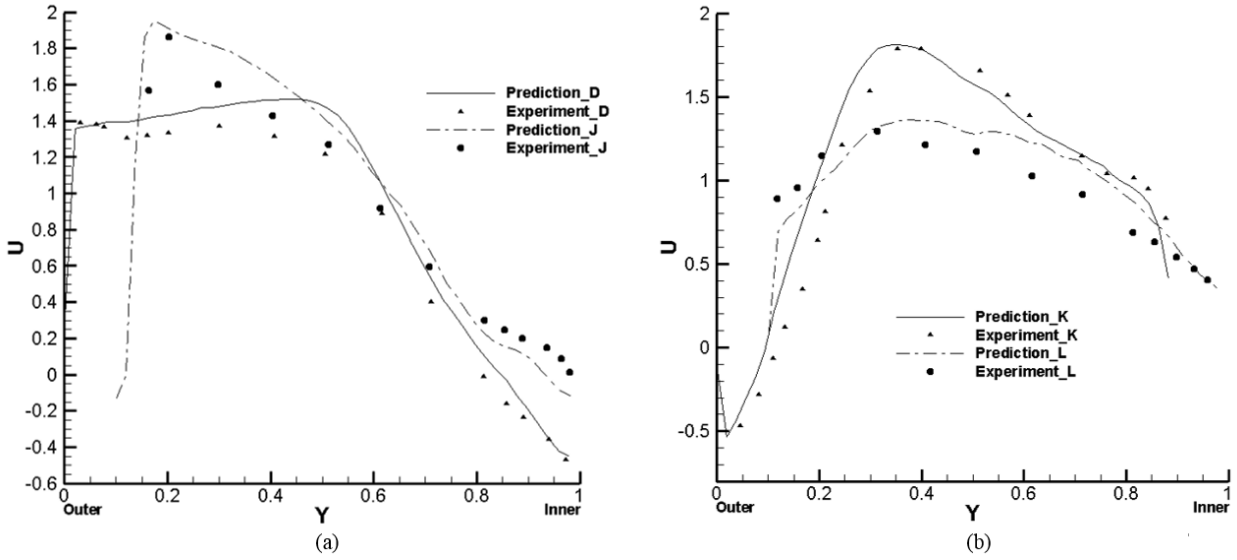

Figure C.3. Mean streamwise flow velocity distribution at locations, (a) D and J (b) K and L, across duct height for Ro=0.0, Bo=0.0.

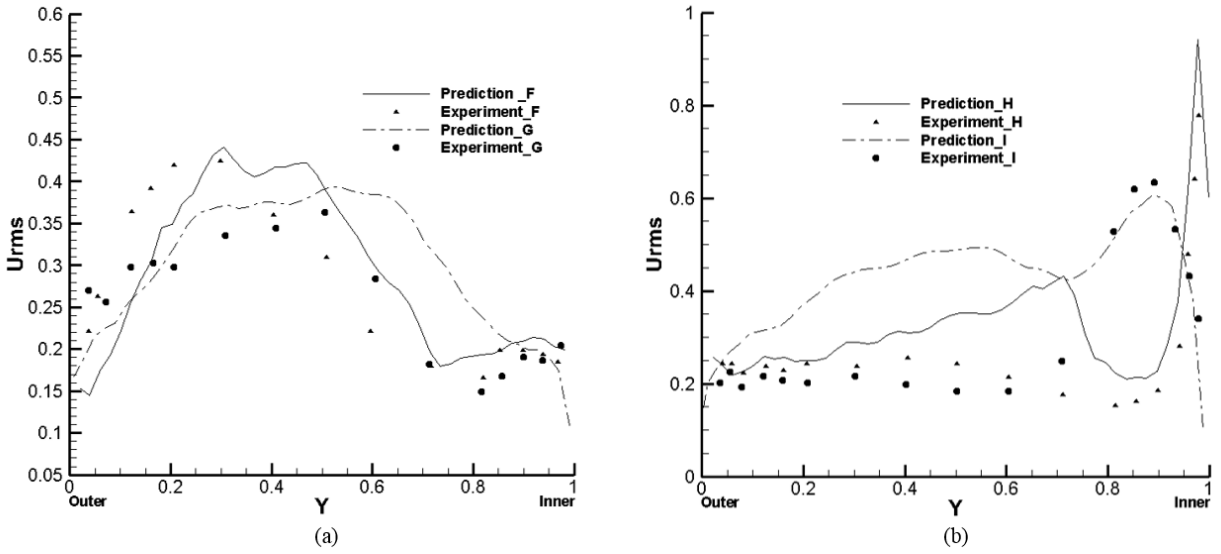

Figure C.4. Turbulence intensity, u_{rms}, variations at locations, (a) F and G (b) H and I, across duct height, for Ro=0.0, Bo=0.0.

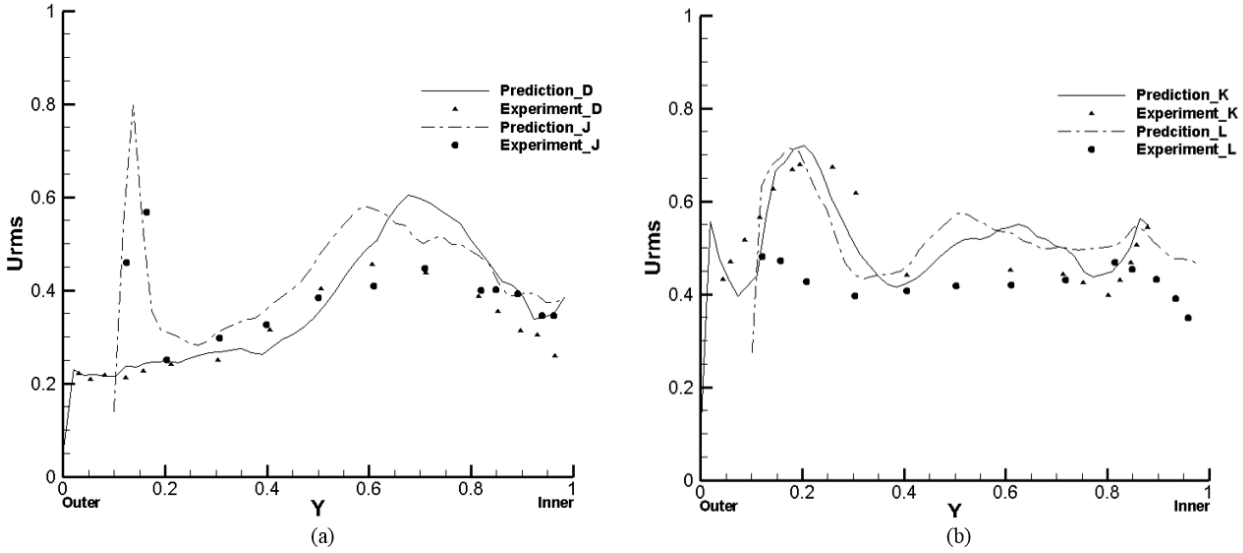

Figure C.5. Turbulence intensity, u_{rms}, variations at locations, (a) D and J (b) K and L, across duct height, for Ro=0.0, Bo=0.0.

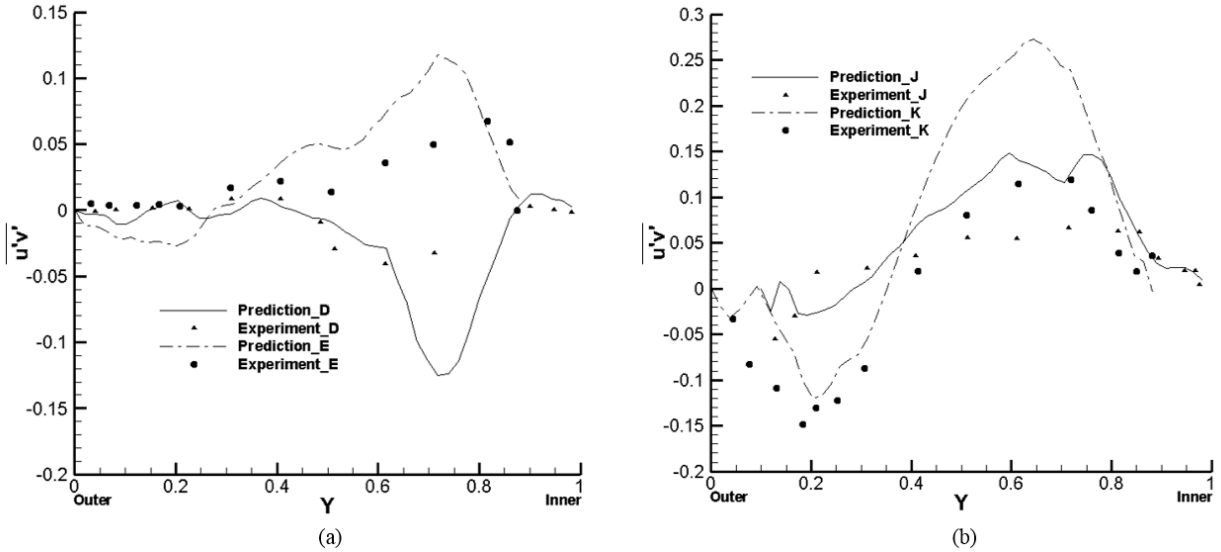

Figure C.6. Turbulent shear stress, $\overline{u'v'}$, variation at locations, (a) D and E (b) J and K, across duct height for Ro=0.0, Bo=0.0.

Rotating Validation of Results –

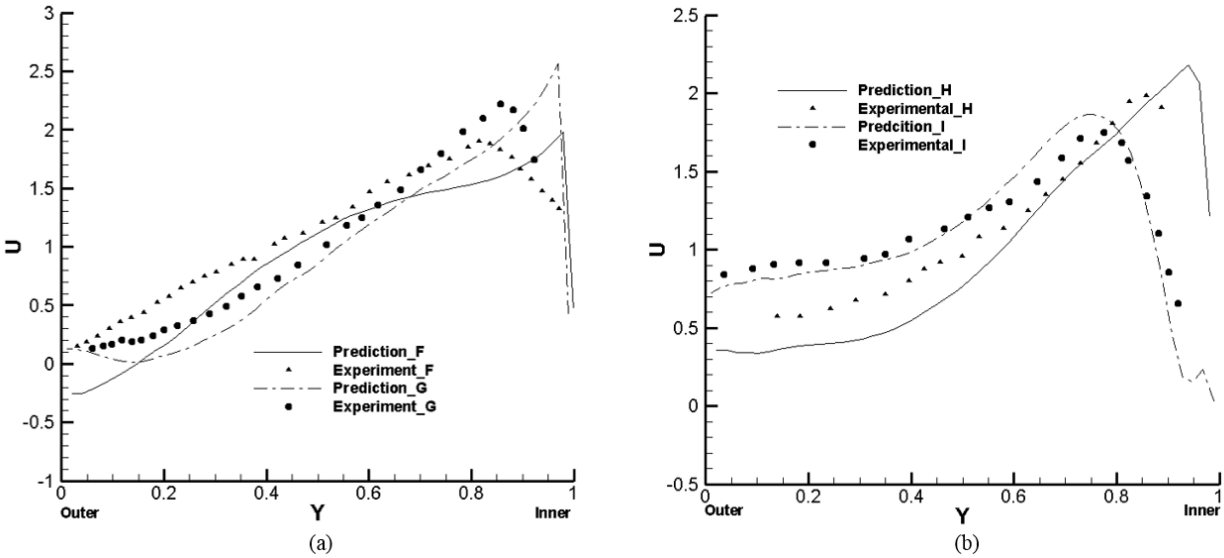

Figure C.7. Mean streamwise flow velocity distributions at locations, (a) F and G (b) H and I, across duct height for Ro=0.2, Bo=0.0.

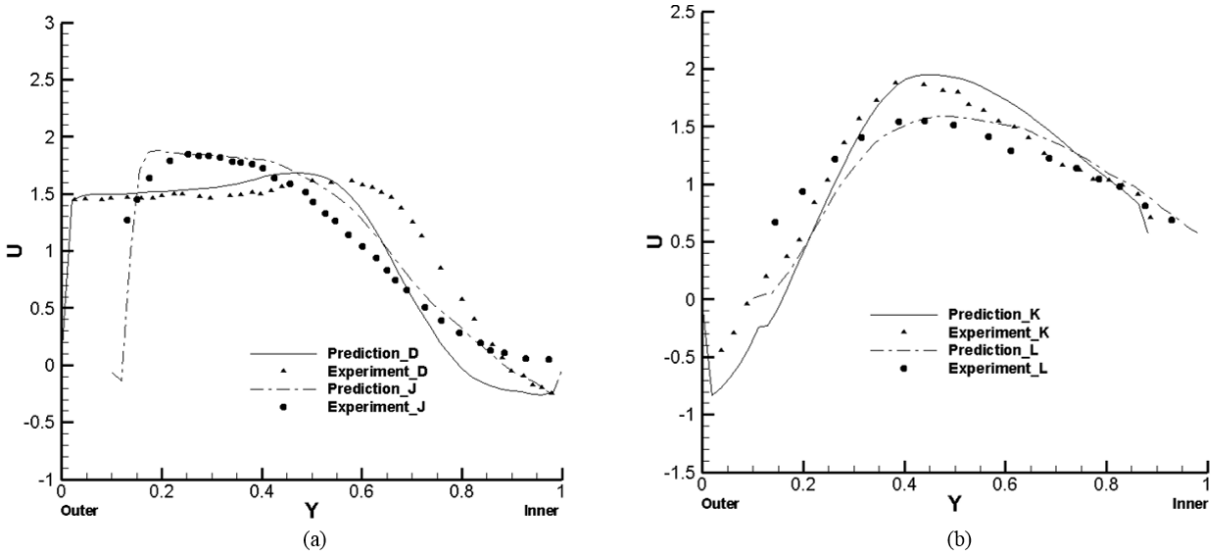

Figure C.8. Mean streamwise flow velocity distributions at locations, (a) D and J (b) K and L, across duct height for Ro=0.2, Bo=0.0.

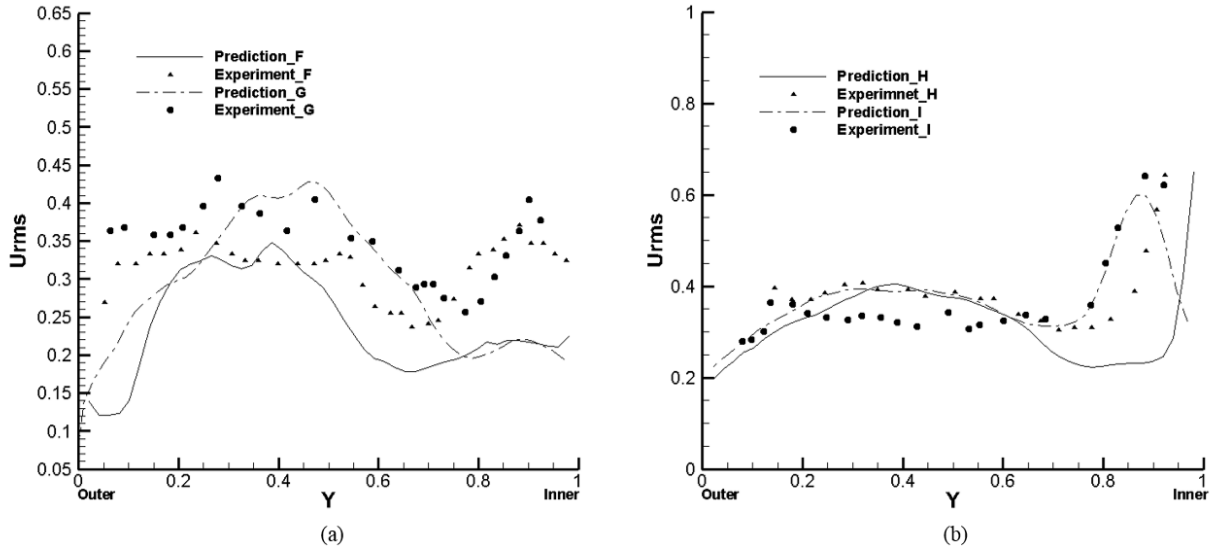

Figure C.9. Turbulence intensity, u_{rms}, variations at locations, (a) F and G (b) H and I, across duct height, for Ro=0.2, Bo=0.0.

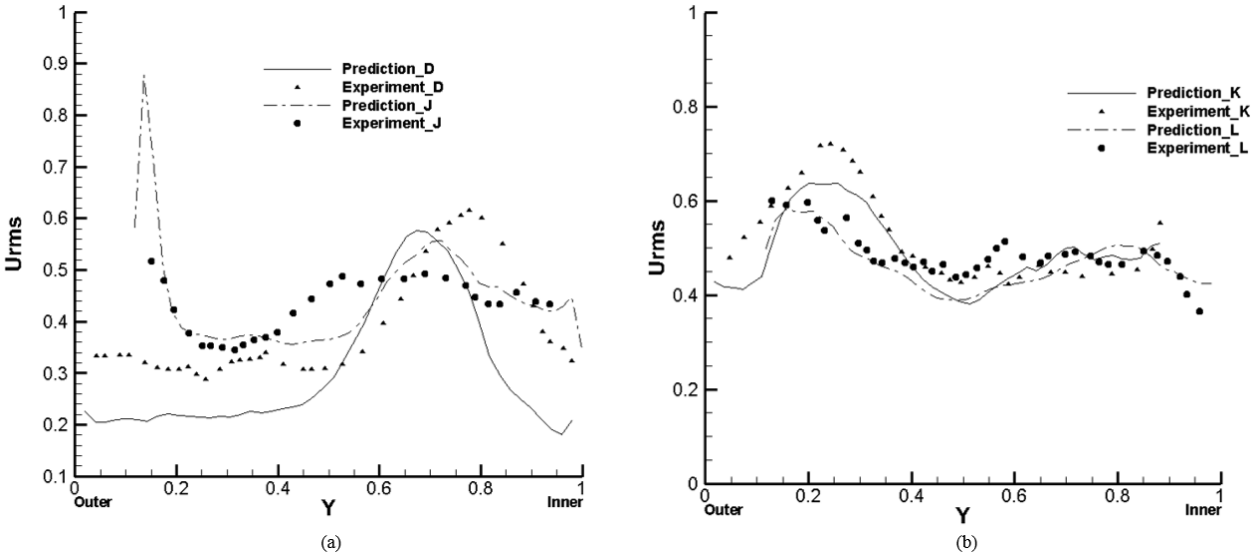

Figure C.10. Turbulence intensity, u_{rms}, variations at locations, (a) D and J (b) K and L, across duct height, for Ro=0.2, Bo=0.0.

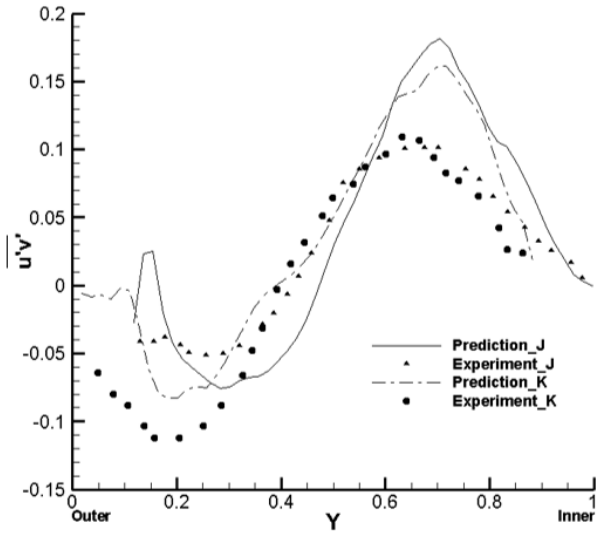

Figure C.11. Turbulent shear stress, $\overline{u'v'}$, variation at locations J and K across duct height for Ro=0.2, Bo=0.0.

Appendix D

Additional Particle-Wall Prediction Results

Presented below are additional prediction contour plots for the particle-wall prediction results from Cases 2, 3 and 5 (rotating 950°C, rotating 1000°C and stationary 950°C, respectively) discussed in Chapter 4. Results presented are for impingement and deposition characteristics and average impact characteristics.

Impact and Deposition Characteristics

The impingement and deposition contours are presented here for surfaces within the ribbed duct. Contour plots of impingement and deposition predictions are normalized by the cell area. For reference to the coordinate system and wall naming convention the reader is referred to Figure D.1. Results are presented here for Cases 2, 3 and 5, for leading and trailing walls, smooth side walls, and end/inner walls within the bend.

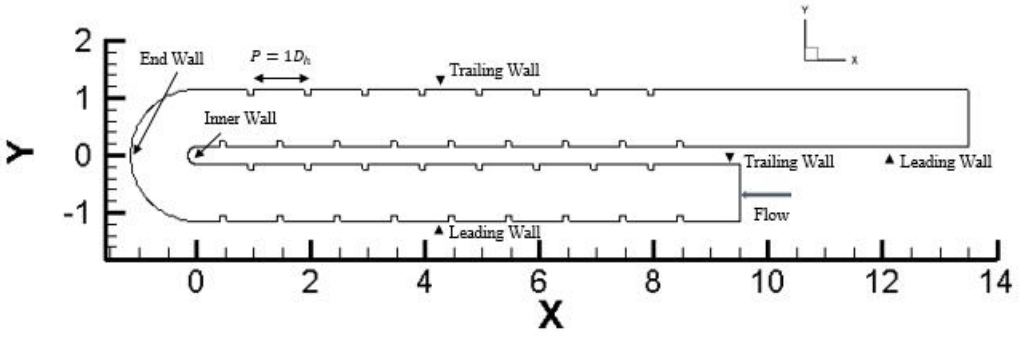

Figure D.1. Computational domain with a top view of two passes, z-direction is coming out of the page.

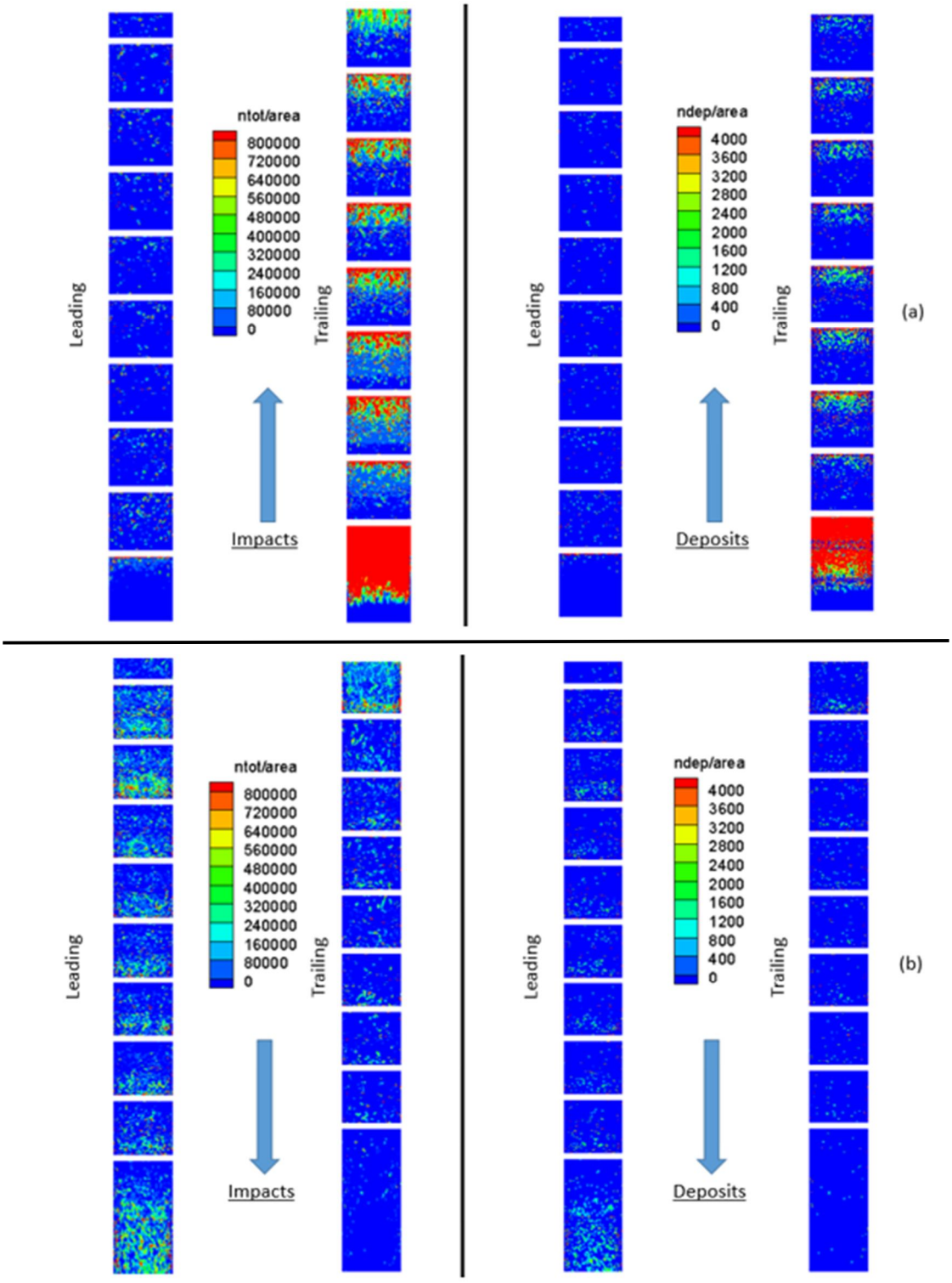

Figure D.2. Contours of particle impingement (left) and deposition (right) for (a) first pass, (b) second pass on the ribbed walls for Ro = 0.2 and a wall temperature of 950°C.

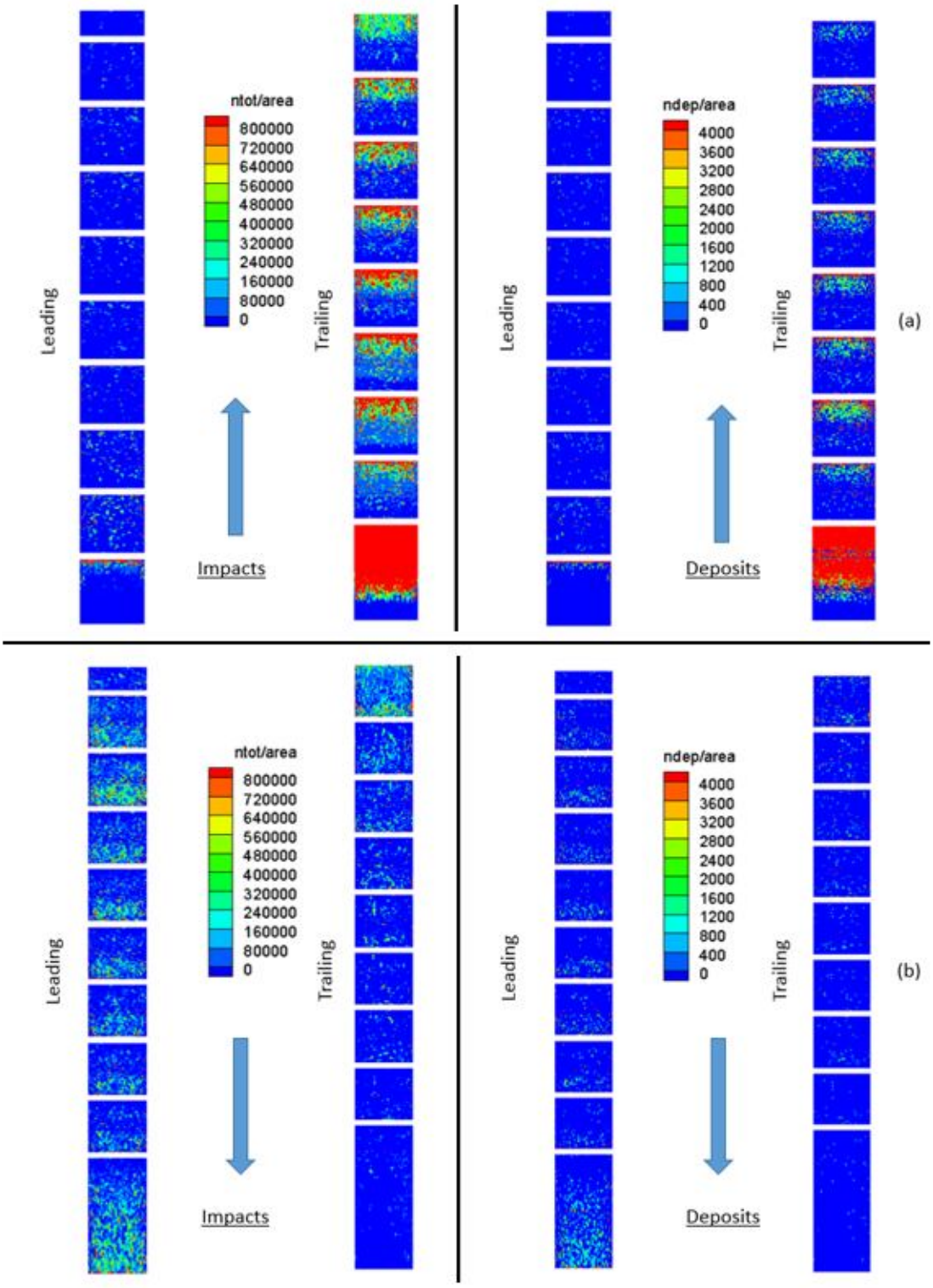

Figure D.3. Contours of particle impingement (left) and deposition (right) for (a) first pass, (b) second pass on the ribbed walls for Ro = 0.2 and a wall temperature of 1000°C.

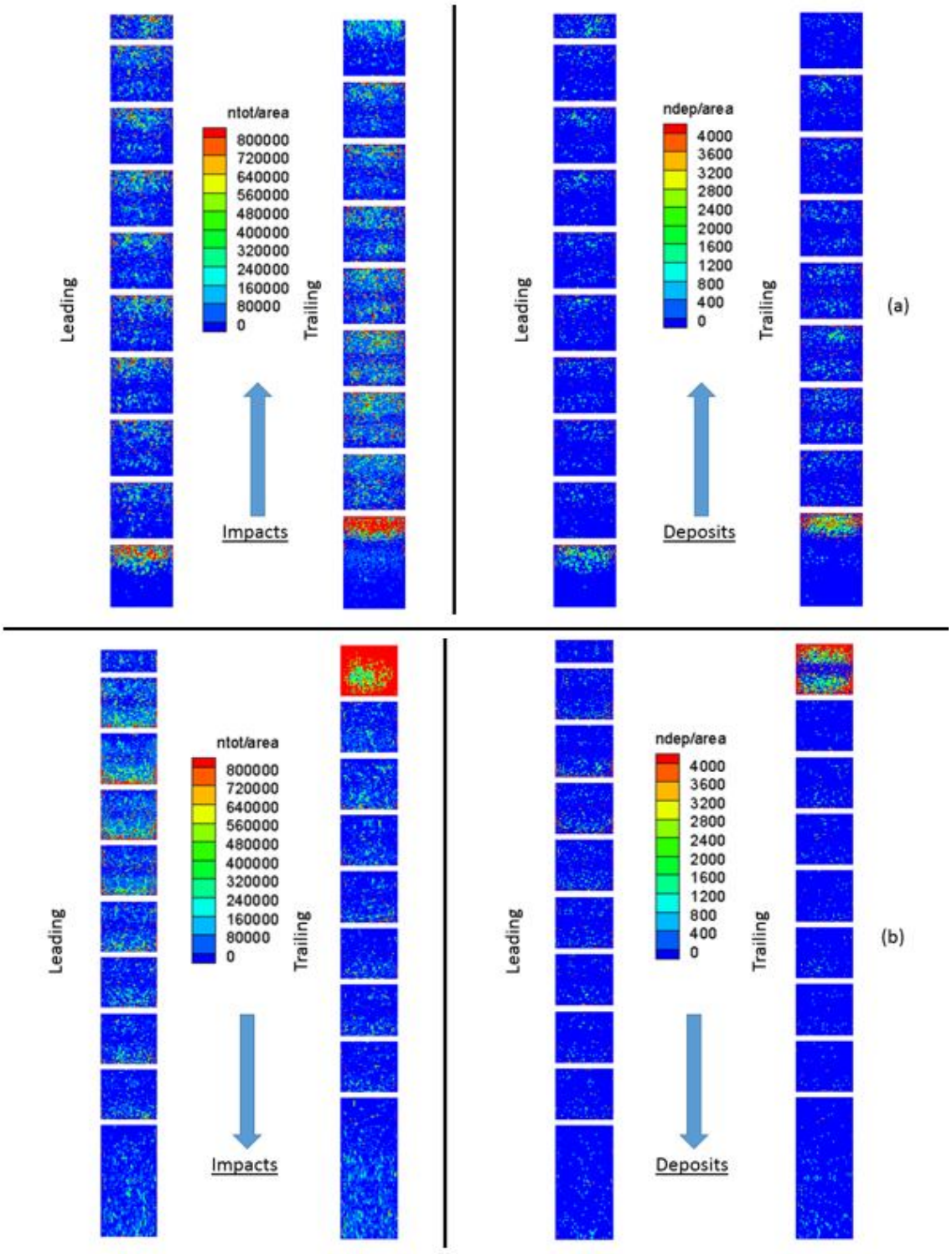

Figure D.4. Contours of particle impingement (left) and deposition (right) for (a) first pass, (b) second pass on the ribbed walls for Ro = 0.0 and a wall temperature of 950°C.

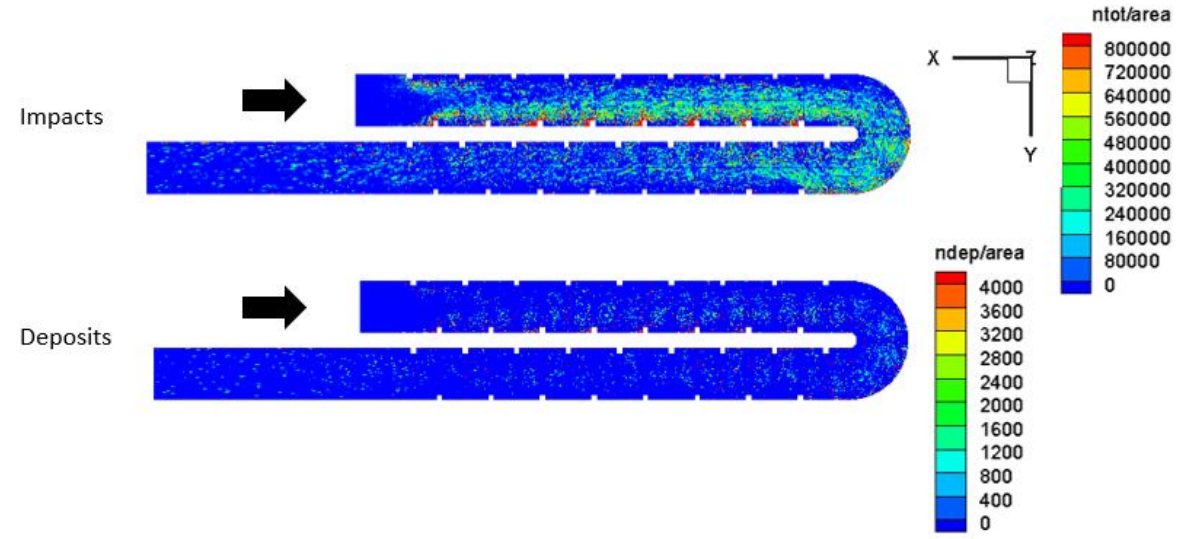

Figure D.5. Contours of particle impingement (top) and deposition (bottom) for smooth side wall (Z = 1.0), with a Ro = 0.2 and a wall temperature of 950°C.

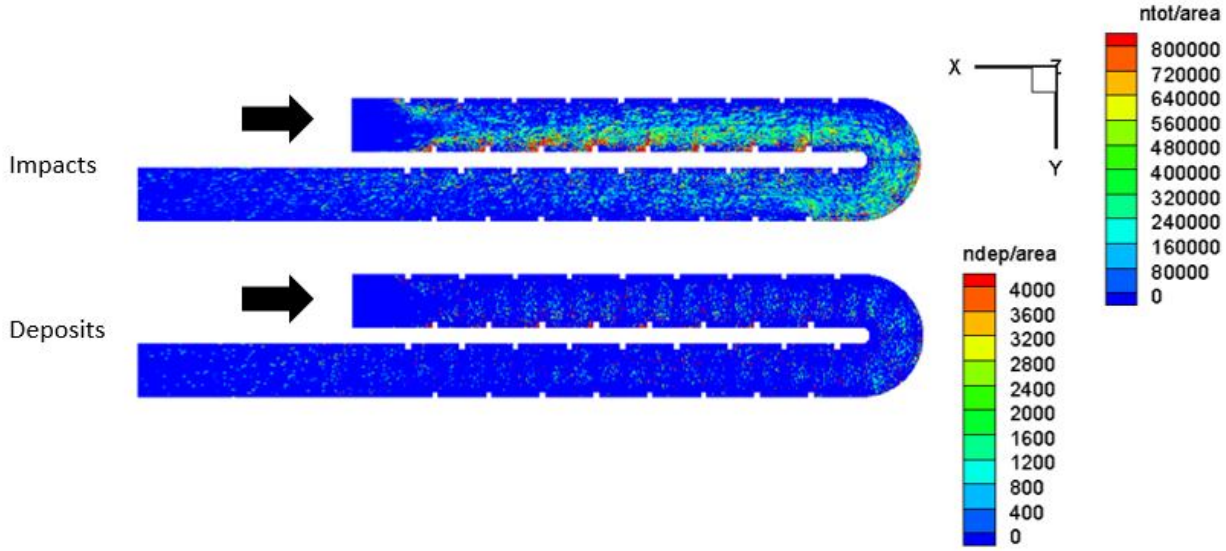

Figure D.6. Contours of particle impingement (top) and deposition (bottom) for smooth side wall (Z = 1.0), with a Ro = 0.2 and a wall temperature of 1000°C.

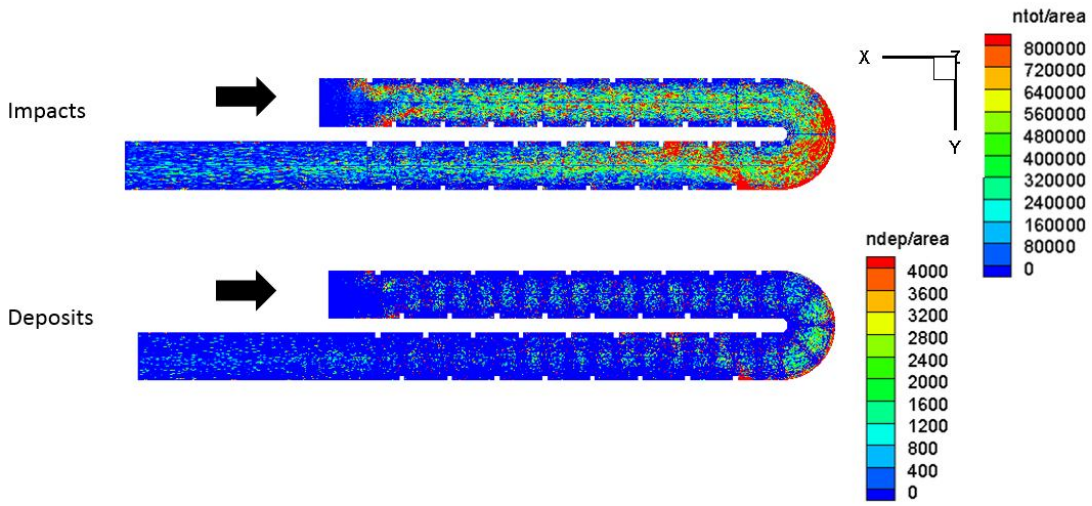

Figure D.7. Contours of particle impingement (top) and deposition (bottom) for smooth side wall (Z = 1.0), with a Ro = 0.0 and a wall temperature of 950°C.

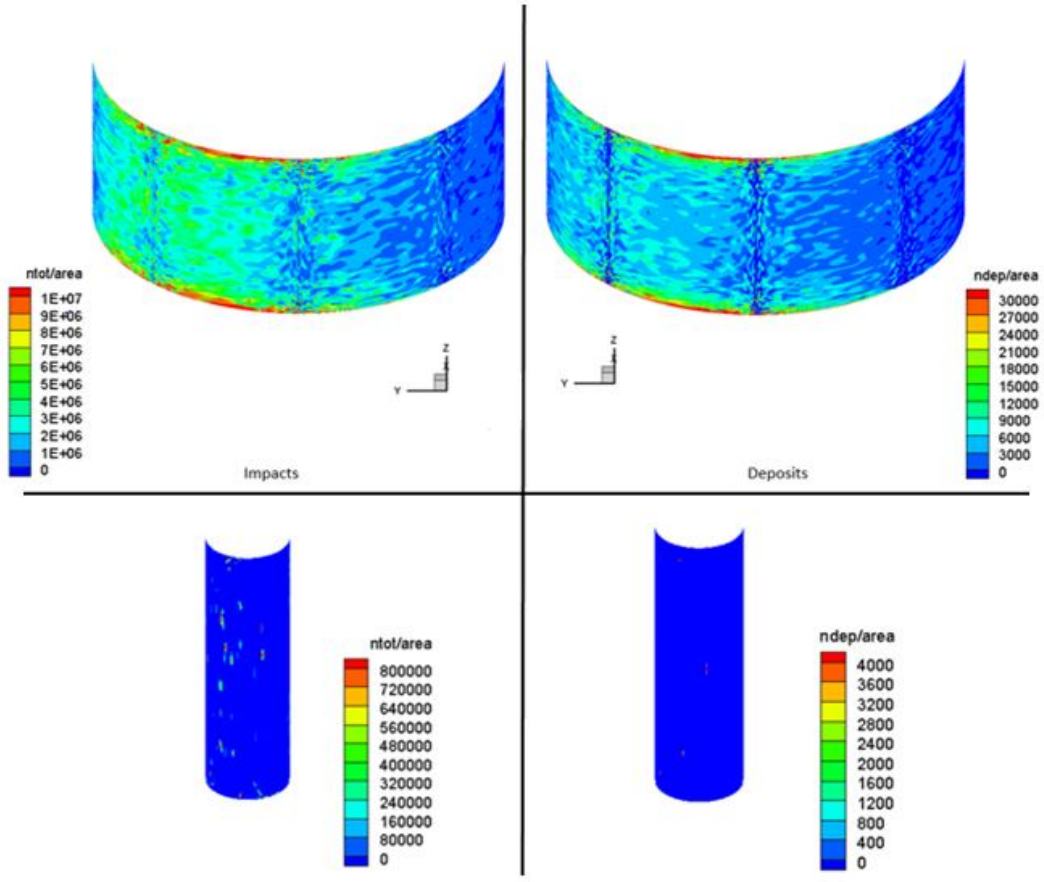

Figure D.8. Contours of particle impingement (left) and deposition (right) for end (top) and inner walls (bottom), with a Ro = 0.2 and a wall temperature of 950°C.

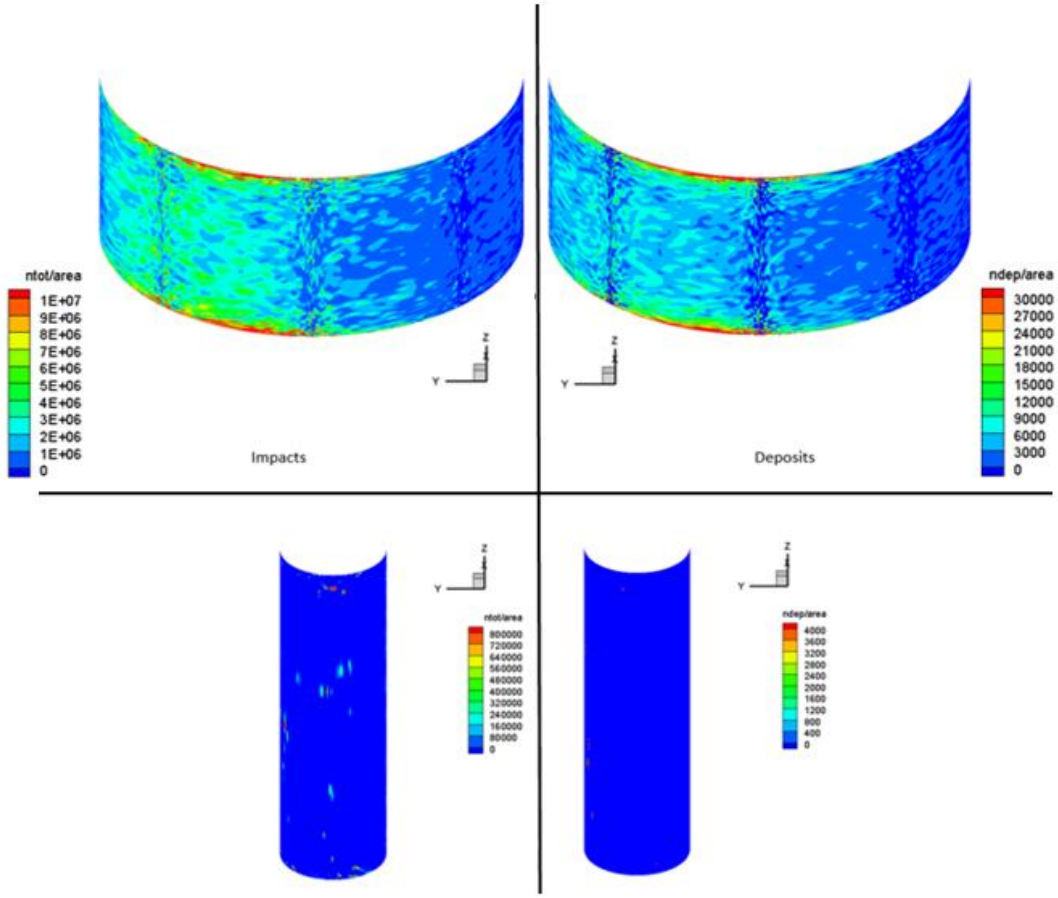

Figure D.9. Contours of particle impingement (left) and deposition (right) for end (top) and inner walls (bottom), with a Ro = 0.2 and a wall temperature of 1000°C.

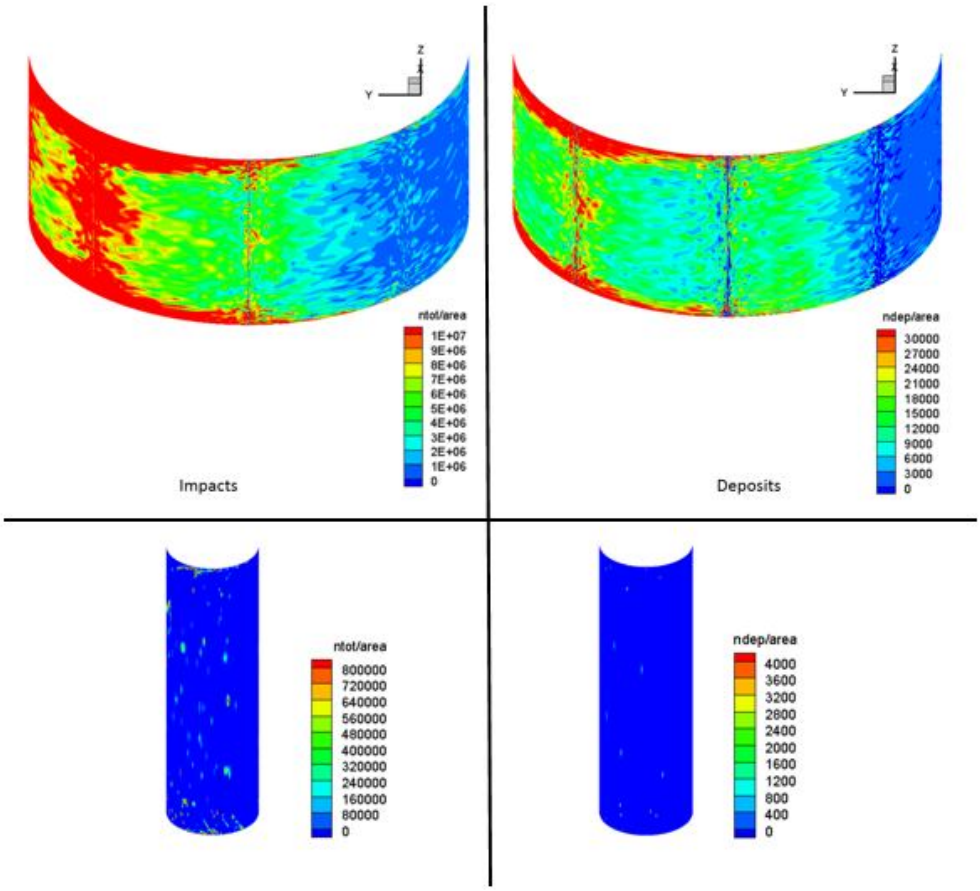

Figure D.10. Contours of particle impingement (left) and deposition (right) for end (top) and inner walls (bottom), with a Ro = 0.0 and a wall temperature of 950°C.

Average Impact Characteristics

The average impact velocity, angle, and temperature are presented here for Cases 2, 3 and 5. The leading and trailing walls, smoooth side walls, and the inner and end walls in the bend are the surfaces for which predictions are presented. The reader is referred to Figured D.1 for reference to coordinate axis and wall labeling. Note dimensional velocity (m/s), angle (°) and temperature (°C) values are presented.

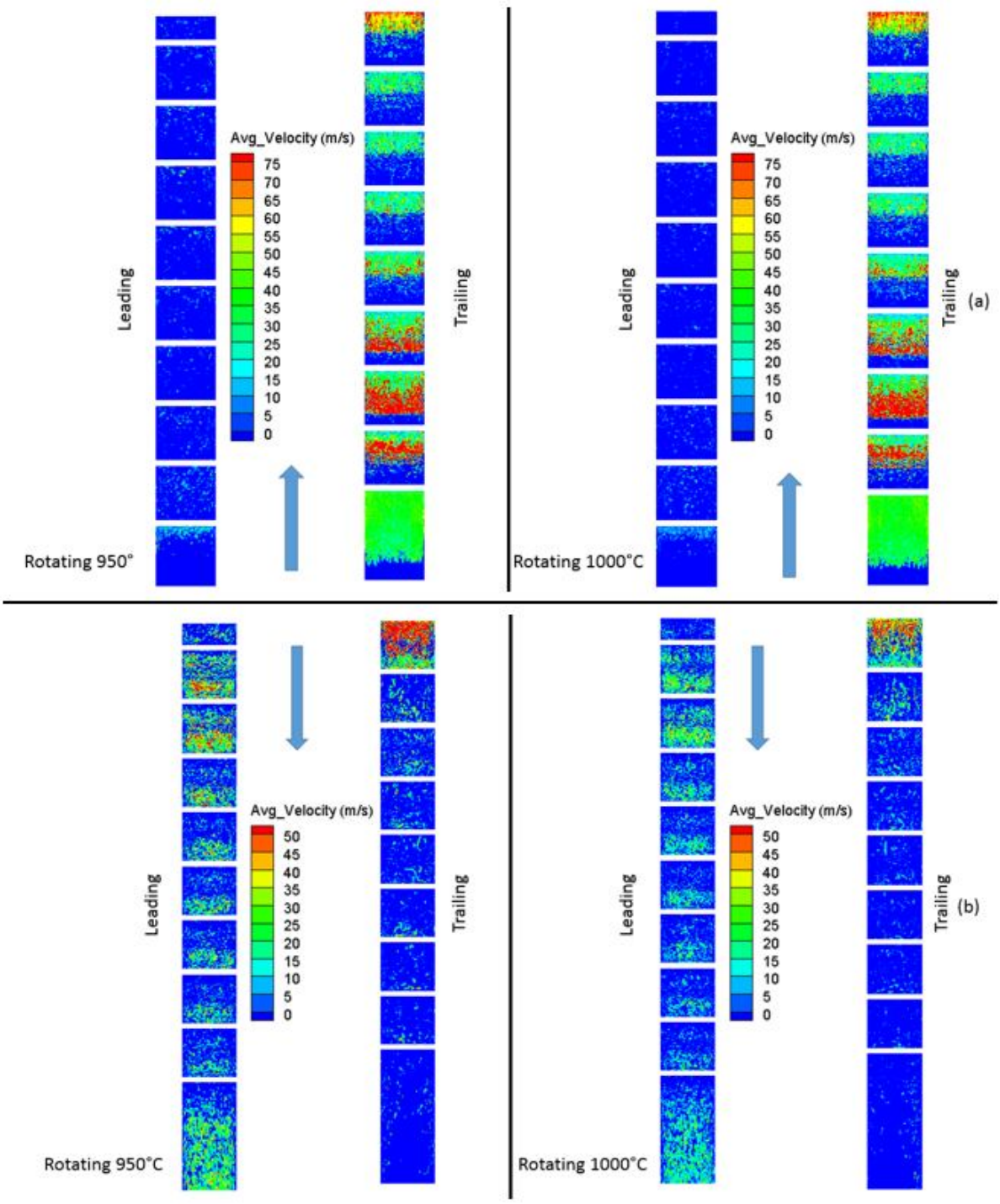

Figure D.11. Contours of average impact velocity (m/s) for TWall - 950°C (left) and TWall - 1000°C (right) on leading and trailing walls of (a) first pass, (b) second pass for Ro = 0.2.

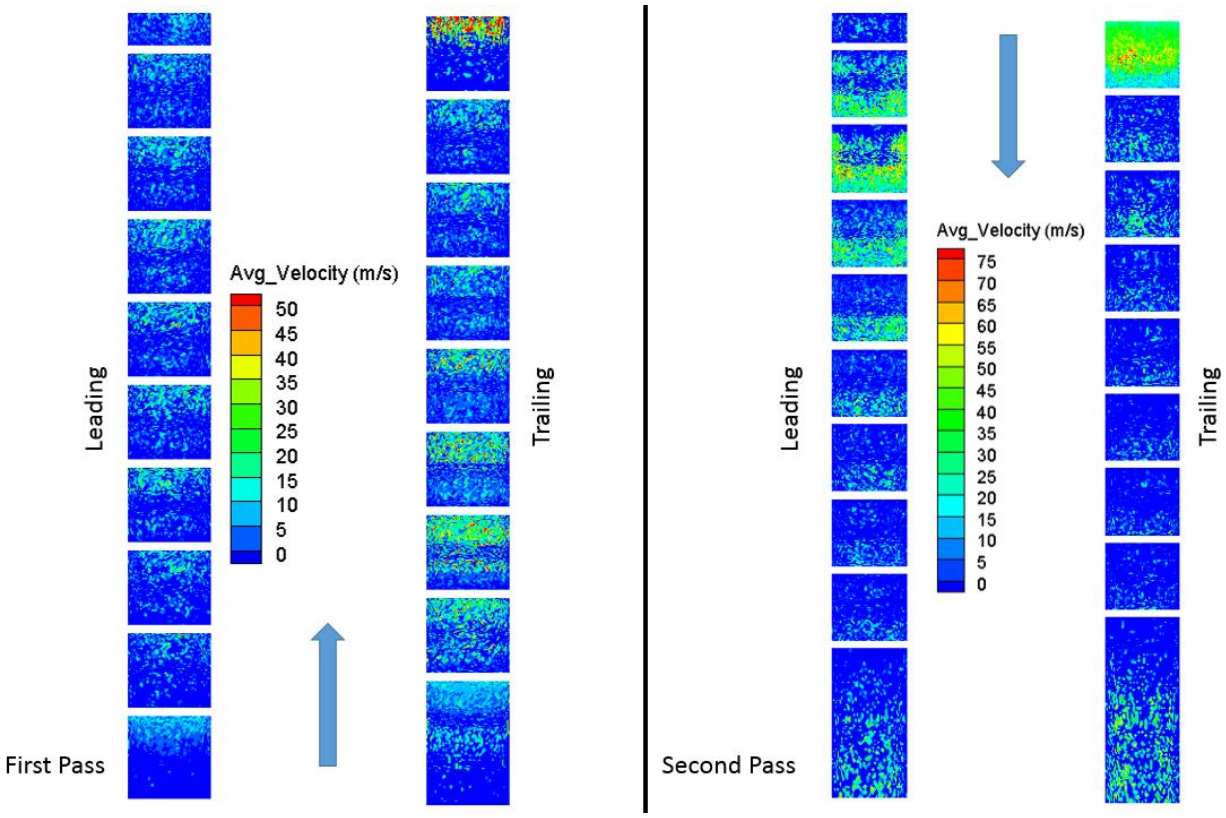

Figure D.12. Contours of average impact velocity (m/s) for stationary 950°C on leading and trailing walls of first pass (left) and second pass (right) for Ro = 0.0.

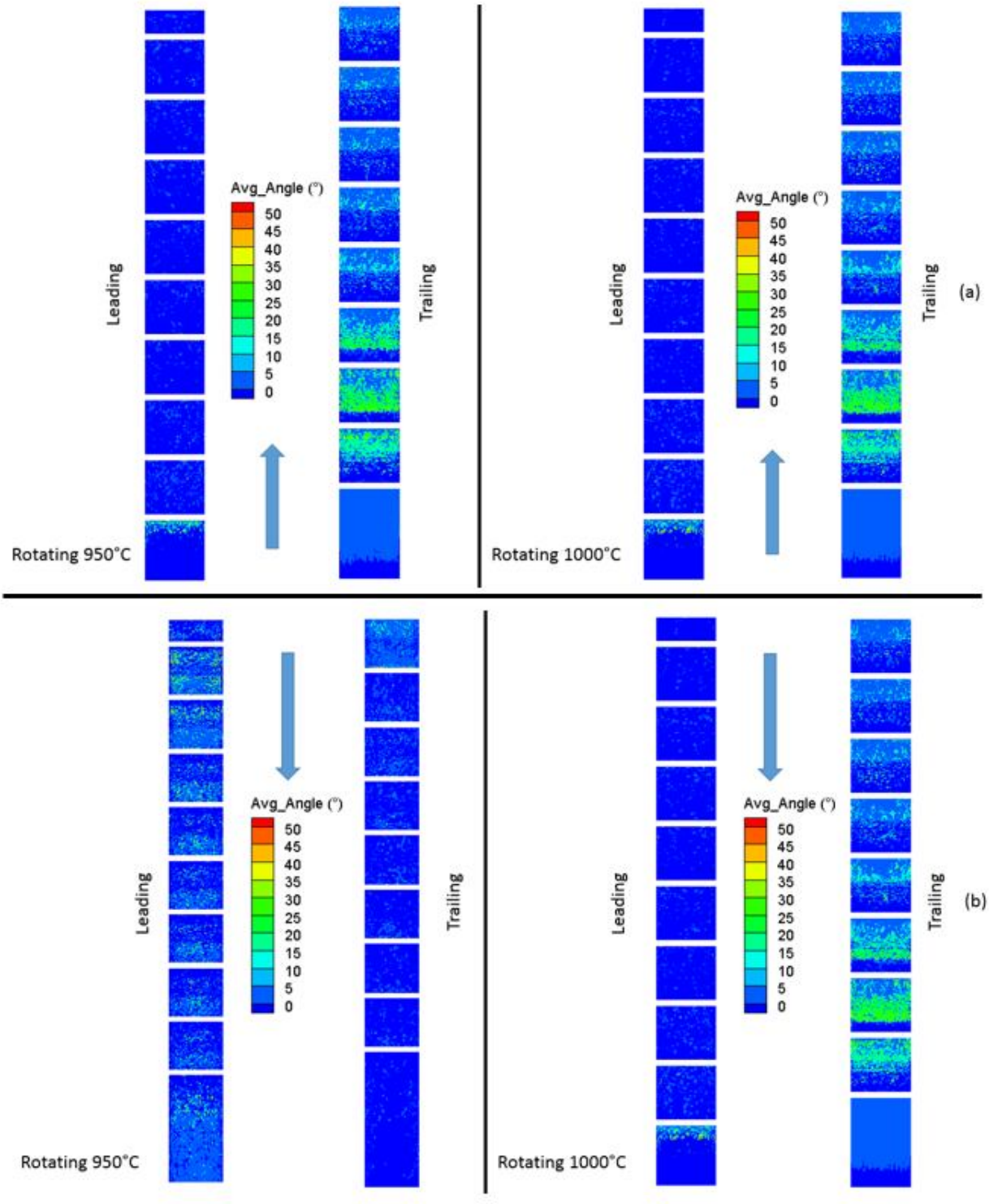

Figure D.13. Contours of average impact angle (°) for TWall - 950°C (left) and TWall - 1000°C (right) on leading and trailing walls of (a) first pass, (b) second pass for Ro = 0.2.

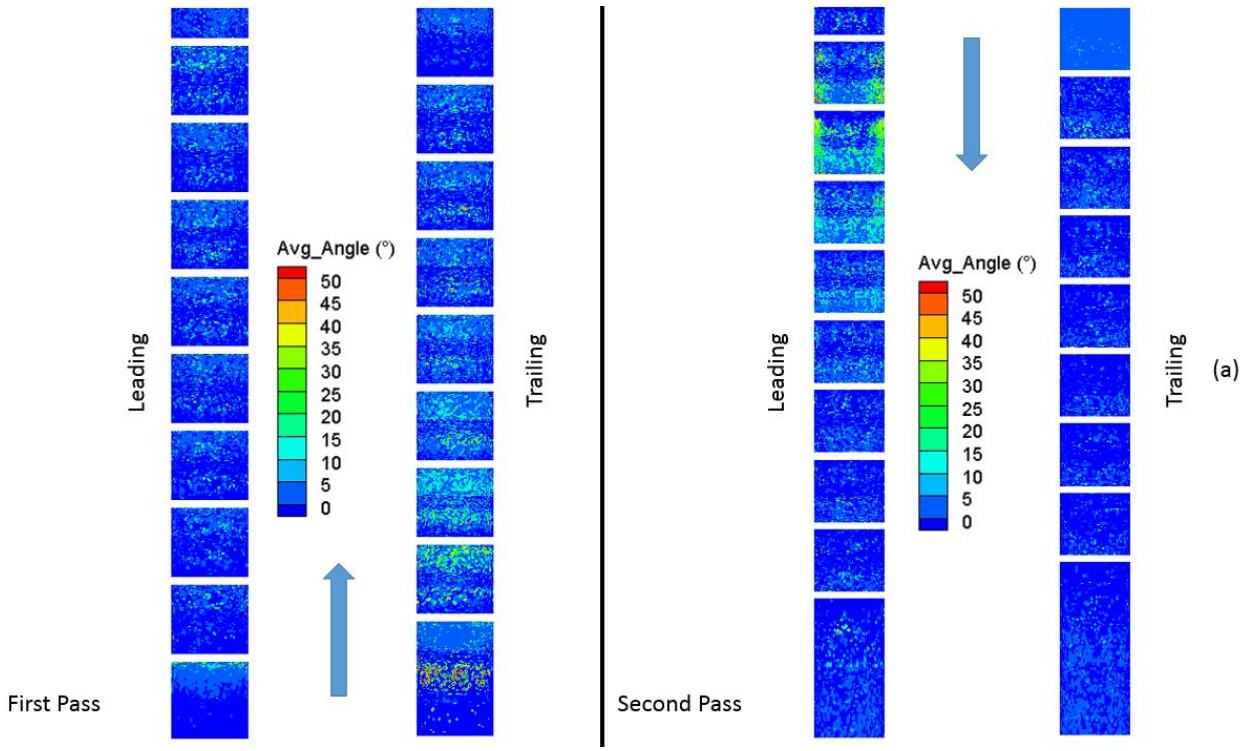

Figure D.14. Contours of average impact angle (°) for stationary 950°C on leading and trailing walls of first pass (left) and second pass (right) for Ro = 0.0.

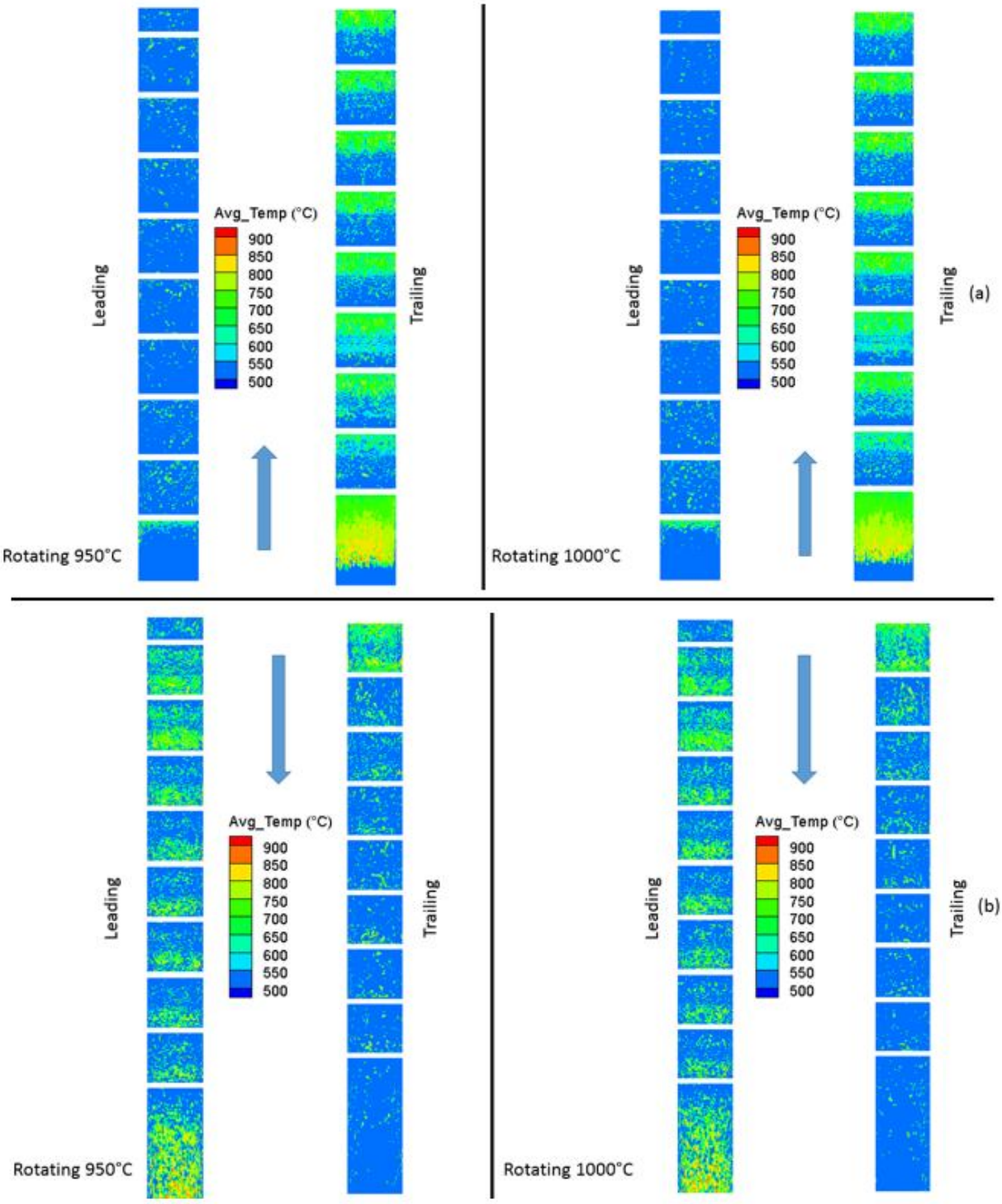

Figure D.15. Contours of average impact temperature (°C) for TWall - 950°C (left) and TWall - 1000°C (right) on leading and trailing walls of (a) first pass, (b) second pass for Ro = 0.2.

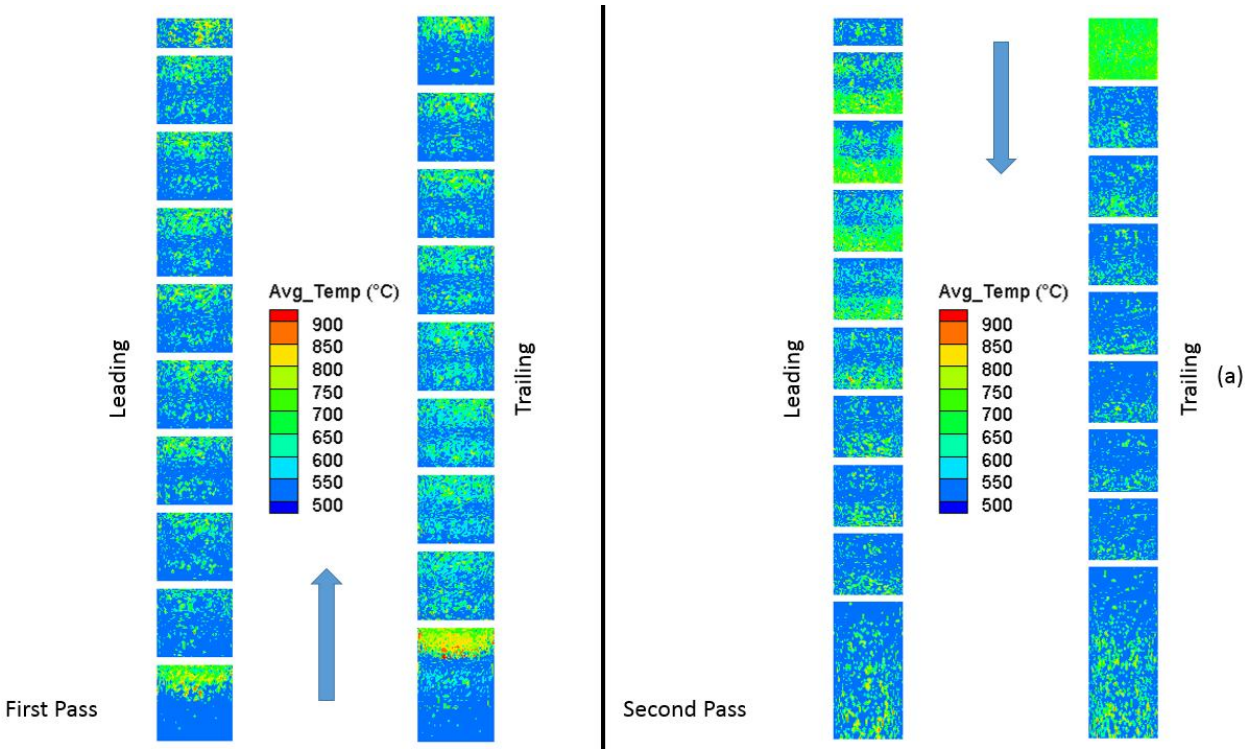

Figure D.16. Contours of average impact temperature (°C) for stationary 950°C on leading and trailing walls of first pass (left) and second pass (right) for Ro = 0.0.

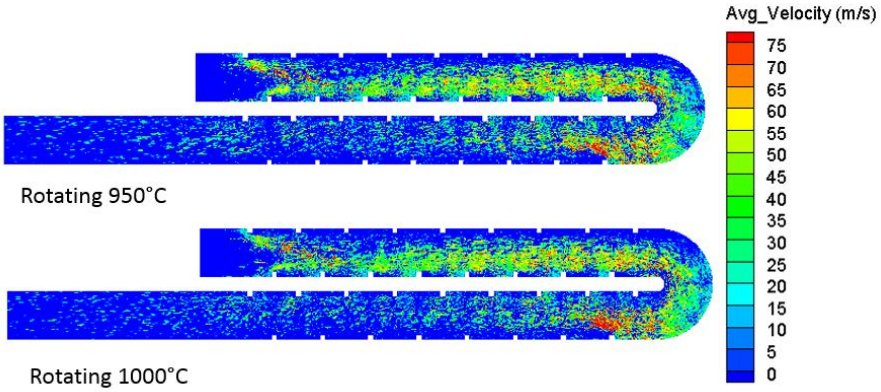

Figure D.17. Contours of average impact velocity for TWall – 950°C (top) and TWall - 1000°C (bottom) for smooth side wall (Z = 1.0), with a Ro = 0.2.

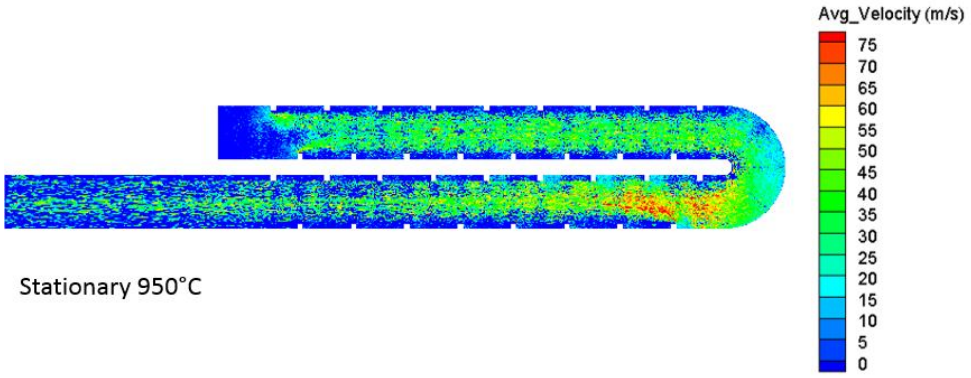

Figure D.18. Contours of average impact velocity (m/s) for stationary 950°C for smooth side wall (Z = 1.0), with a Ro = 0.0.

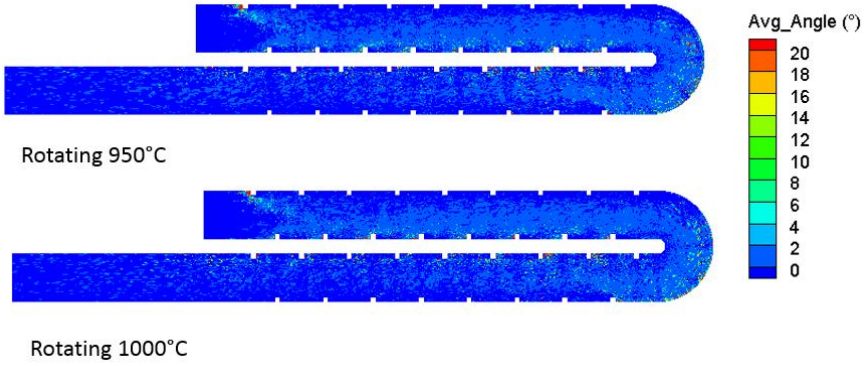

Figure D.19. Contours of average impact angle (°) for TWall – 950°C (top) and TWall - 1000°C (bottom) for smooth side wall (Z = 1.0), with a Ro = 0.2.

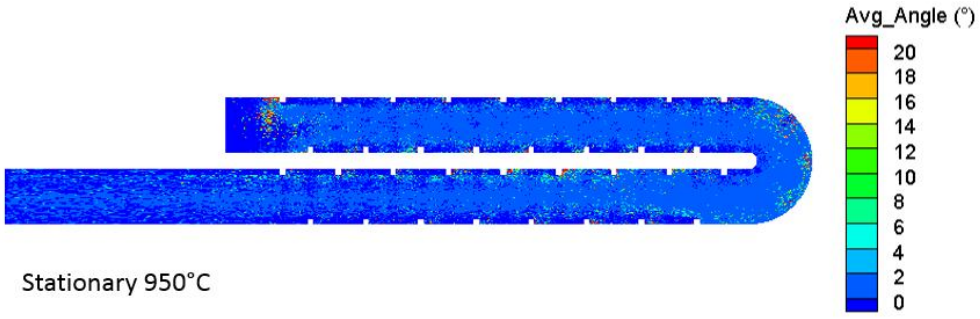

Figure D.20. Contours of average impact angle (°) for stationary 950°C for smooth side wall (Z = 1.0), with a Ro = 0.0.

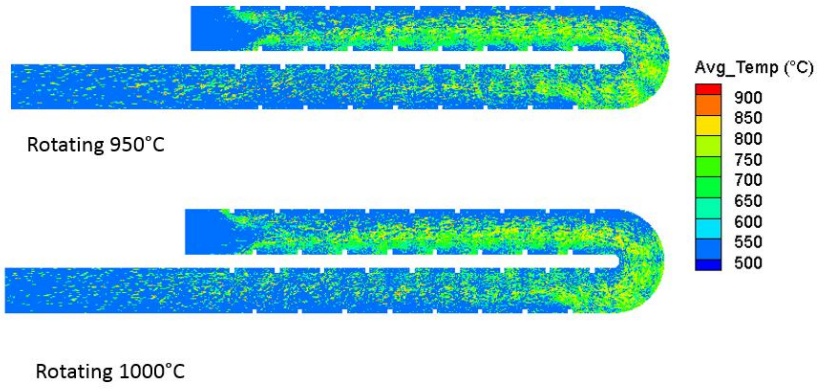

Figure D.21. Contours of average impact temperature (°C) for TWall – 950°C (top) and TWall - 1000°C (bottom) for smooth side wall (Z = 1.0), with a Ro = 0.2.

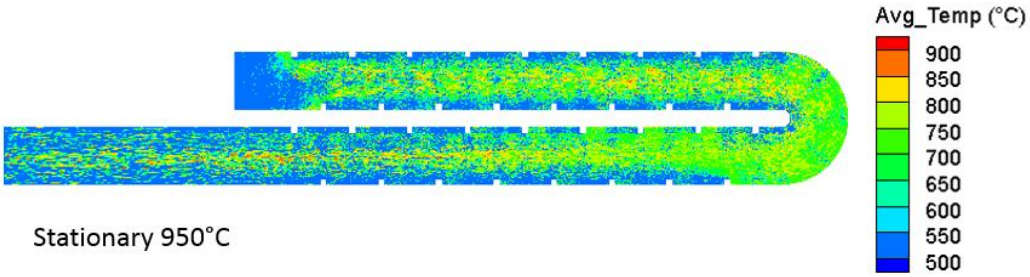

Figure D.22. Contours of average impact temperature (°C) for stationary 950°C for smooth side wall (Z = 1.0), with a Ro = 0.0.

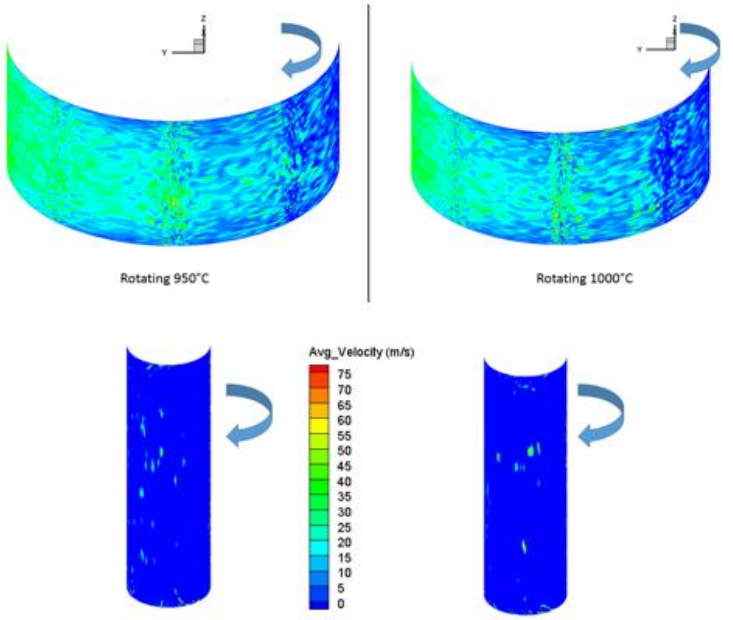

Figure D.23. Contours of average impact velocity (m/s) for TWall – 950°C (left) and TWall – 1000°C (right) for end (top) and inner walls (bottom), with a Ro = 0.2.

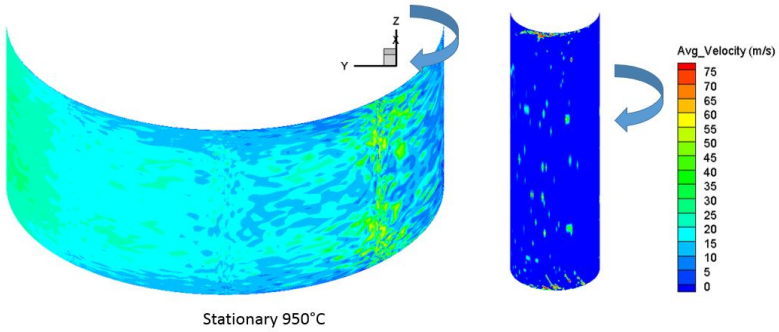

Figure D.24. Coutours of average impacting velocity (m/s) for stationary 950°C for end (left) and inner walls (right), with a Ro=0.0.

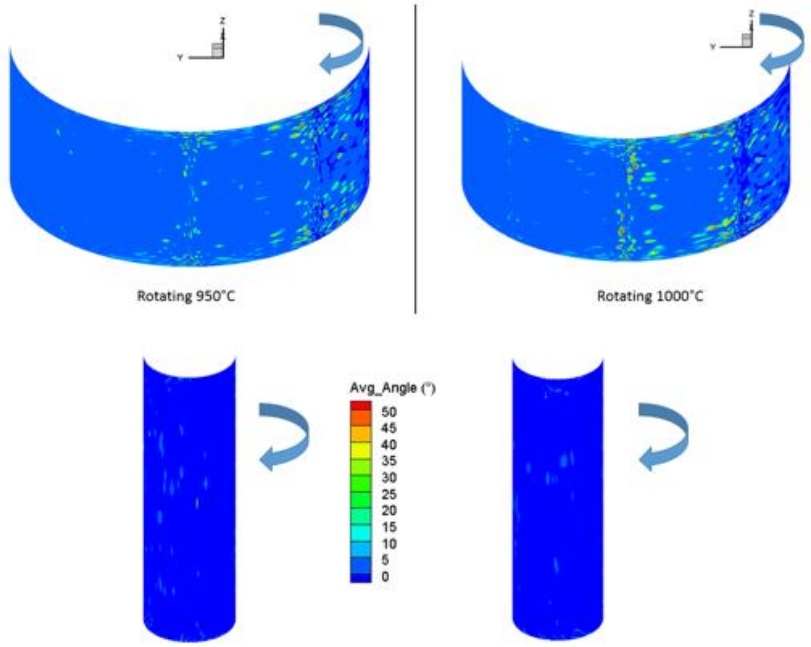

Figure D.25. Contours of average impact angle (°) for TWall – 950°C (left) and TWall – 1000°C (right) for end (top) and inner walls (bottom), with a Ro = 0.2.

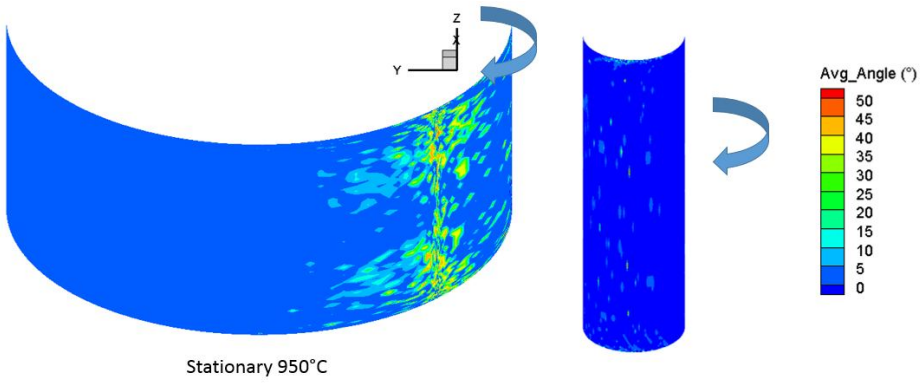

Figure D.26. Coutours of average impacting angle (°) for stationary 950°C for end (left) and inner walls (right), with a Ro=0.0.

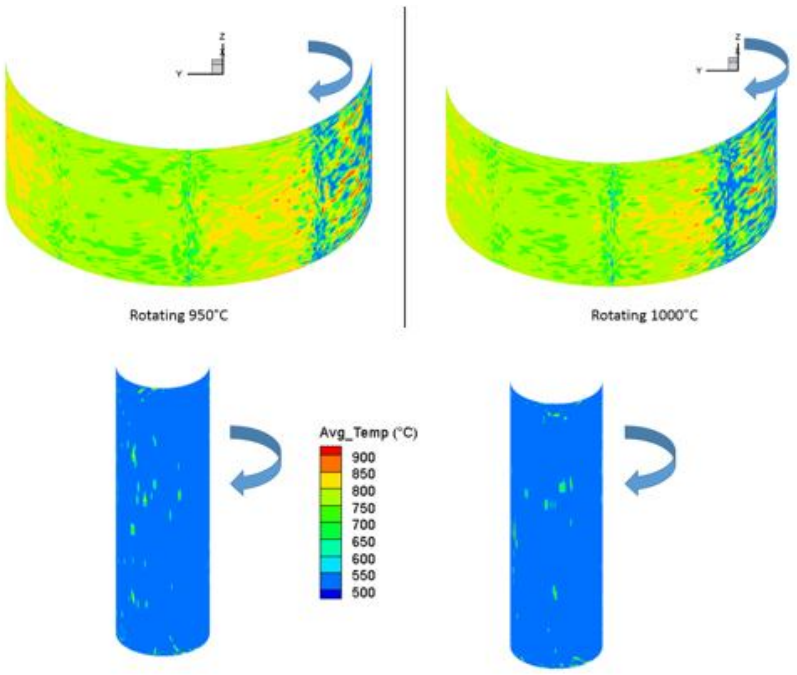

Figure D.27. Contours of average impact temperature (°C) for TWall – 950°C (left) and TWall – 1000°C (right) for end (top) and inner walls (bottom), with a Ro = 0.2.

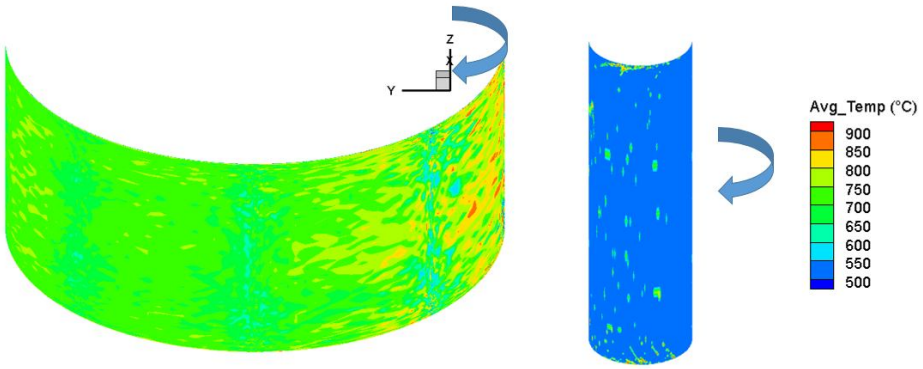

Figure D.28. Coutours of average impacting temperature (°C) for stationary 950°C for end (left) and inner walls (right), with a Ro=0.0.

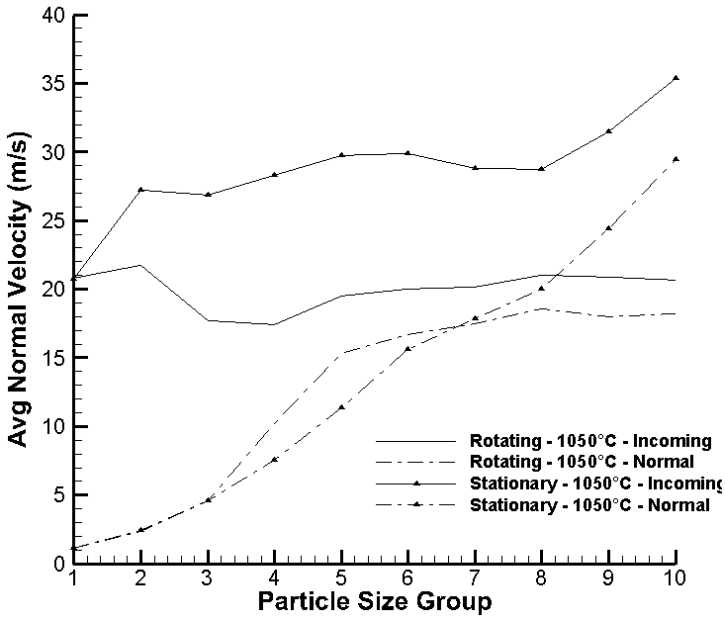

Figure D.29. Average impact normal and incoming velocity (m/s) for deposited particles for rotating and stationary domains.

REFERENCES

1. Han, Je-Chin, Sandip Dutta, and Srinath Ekkad, 2012, *Gas turbine heat transfer and cooling technology*. CRC Press.

2. Iacovides, H., Jackson, D.C., Ji, H., Kelemenis G., Launder, B. E., and Nikas, K., 1996. "LDA study of the flow development through an orthogonally rotating U-bend of strong curvature and rib roughened walls," *Journal of Turbomachinery*, 120(April), pp. 386–391.

3. Iacovides, H., Jackson, D. C., Kelmenis, G., Launder, B., 2000, "The measurement of local wall heat transfer in stationary U-ducts of strong curvature, with smooth and rib-roughened walls," *Journal of Turbomachinery* 122.2, pp.386-392.

4. Tafti, D. K., 2001, "Genidlest: A Scalable Parallel Computational Tool for Simulating Complex Turbulent Flows," *ASME-PUBLICATIONS-FED* 256, pp. 347-356.

5. Tafti, Danesh K, 2011 "Time-accurate techniques for turbulent heat transfer analysis in complex geometries." *Computational Fluid Dynamics and Heat Transfer, R. Amano, and B. Sunden, eds., WIT PRESS, Southampton, UK*, pp. 217-264.

6. Patil, Sunil, and Danesh Tafti, 2012, "Wall modeled large eddy simulations of complex high Reynolds number flows with synthetic inlet turbulence," *International Journal of Heat and Fluid Flow* 33.1, pp. 9-21.

7. Shah, A., 2005 "*Development and application of dispersed two phase capability in a general multi-block Navier-Stokes solver,*" Diss. Thesis, Virginia Polytechnic Institute and State University, Blacksburg, VA.

8. White, Frank M., and Isla Corfield, 2006, *Viscous fluid flow*. Vol. 3. New York: McGraw-Hill.

9. Patankar, S. V., Liu, C. H., & Sparrow, E. M., 1977, "Fully developed flow and heat transfer in ducts having streamwise-periodic variations of cross-sectional area," *Journal of Heat Transfer*, 99(2), pp.180-186.

10. Chapman, Dean Khalil, 1979, "Computational aerodynamics development and outlook." *AIAA journal* 17.12, pp. 1293-1313.

11. Cabot, W., and P. Moin, 2000, "Approximate wall boundary conditions in the large-eddy simulation of high Reynolds number flow." *Flow, Turbulence and Combustion* 63.1-4, pp. 269-291.

12. Kays, William M, 1994, "Turbulent Prandtl number—where are we?." *Journal of Heat Transfer* 116.2, pp. 284-295.

13. Shah, Anant, and Danesh K. Tafti, 2007, "Transport of particulates in an internal cooling ribbed duct," *Journal of Turbomachinery* 129.4, pp. 816-825.

14. Elghobashi, S., and G. C. Truesdell. 1992, "Direct simulation of particle dispersion in a decaying isotropic turbulence," *Journal of Fluid Mechanics* 242, pp. 655-700.

15. Wang, Q., K. D. Squires, M. Chen, and J. B. McLaughlin. 1997, "On the role of the lift force in turbulence simulations of particle deposition." *International Journal of Multiphase Flow* 23, no. 4, pp. 749-763.

16. Kulick, Jonathan D., John R. Fessler, and John K. Eaton, 1994, "Particle response and turbulence modification in fully developed channel flow." *Journal of Fluid Mechanics* 277, pp. 109-134.

17. Kaftori, D., G. Hetsroni, and S. Banerjee, 1995, "Particle behavior in the turbulent boundary layer. I. Motion, deposition, and entrainment." *Physics of Fluids (1994-present)* 7, no. 5, pp. 1095-1106.

18. Wang, Q., and K. D. Squires, 1996, "Large eddy simulation of particle deposition in a vertical turbulent channel flow." *International Journal of Multiphase Flow*22, no. 4, pp. 667-683.

19. Armenio, Vincenzo, Ugo Piomelli, and Virgilio Fiorotto, 1999, "Effect of the subgrid scales on particle motion." *Physics of Fluids (1994-present)* 11, no. 10, pp. 3030-3042.

20. Clift, Roland, John R. Grace, and Martin E. Weber, 2005, *Bubbles, drops, and particles*. Courier Corporation.

21. Crowe, C. T., R. A. Gore, and T. R. Troutt, 1985, "Particle dispersion by coherent structures in free shear flows." *Particulate Science and Technology* 3, no. 3-4, pp. 149-158.

22. Bergman, Theodore L., Frank P. Incropera, and Adrienne S. Lavine, 2011, *Fundamentals of heat and mass transfer*. John Wiley & Sons.

23. Wagner, J. H., B. V. Johnson, and F. C. Kopper, 1991, "Heat transfer in rotating serpentine passages with smooth walls," *Journal of Turbomachinery* 113.3, pp. 321-330.

24. Mayo, I., Arts, T., El-Habib, A., Parres, B., 2015, "Two-Dimensional Heat Transfer Distribution of a Rotating Ribbed Channel at Different Reynolds Numbers," *Journal of Turbomachinery* 137.3, No. 031002.

25. Prakash, C., Zerkle, R., 1995, "Prediction of Turbulent Flow and Heat Transfer in a Ribbed Rectangular Duct With and Without Rotation," *ASME Journal of Turbomachinery* 117, pp. 255-264.

26. Zhao, C.Y., Tao and W.Q., 1997, "A Three Dimensional Investigation of Turbulent Flow and Heat Transfer Around Sharp 180° Turns in Two-Pass Rib-Roughened Channels," *International Communications of Heat and Mass Transfer* 24, pp. 587-596.

27. Lin, Y.L., Shih, T.I.-P., Stephens, M.A. and Chyu, M.K., 2001, "A Numerical Study of Flow and Heat Transfer in a Smooth and Ribbed U-Duct With and Without Rotation," *ASME Journal of Heat Transfer* 123, pp. 219-231.

28. Saidi, A. and Sundén, B., 2001, "On Prediction of Thermal-Hydraulic Characteristics of Square-Sectioned Ribbed Cooling Ducts," *ASME Journal of Turbomachinery* 123.3, pp. 614-620.

29. Iacovides, H., 1998, "Computation of Flow and Heat Transfer through Rotating Ribbed Passages," *International Journal of Heat and Fluid Flow* 19, pp. 393-400.

30. Iacovides, H. and Raisee, M., 2001, “Computation of Flow and Heat Transfer in Two-Dimensional Rib-Roughened Passages, Using Low-Reynolds-Number- Turbulence Models,” *International Journal of Numerical Methods for Heat and Fluid Flow* 11, pp. 138-155.

31. Okita, Y. and Iacovides, H., 2003, “Comparisons of High-Reynolds-Number EVM and DSM Models in the Prediction of Heat and Fluid Flow of Turbine Blade Cooling Passages,” *ASME Journal of Turbomachinery* 425, pp. 585-597.

32. Sleiti, A. K., and J. S. Kapat, 2008, "Effect of Coriolis and centrifugal forces on turbulence and transport at high rotation and density ratios in a rib-roughened channel," *International Journal of Thermal Sciences* 47.5, pp. 609-619.

33. Chen, Hamn-Ching, Yong-Jun Jang, and Je-Chin Han, 2000, "Computation of heat transfer in rotating two-pass square channels by a second-moment closure model," *International Journal of Heat and Mass Transfer* 43.9, pp. 1603-1616.

34. Al-Qahtani, M., Jang, Y.J., Chen, H.C. and Han, J.C., 2002, “Prediction of Flow and Heat Transfer in Rotating Two-Pass Rectangular Channels with 45° Rib Turbulators,” *ASME Journal of Turbomachinery* 124, pp. 242-250.

35. Ooi, A., Iaccarino, G., Durbin, P. A., Behnia, M., 2002, "Reynolds averaged simulation of flow and heat transfer in ribbed ducts," *International Journal of Heat and Fluid Flow* 23.6, pp. 750-757.

36. Tafti, D. K., 2005, "Evaluating the role of subgrid stress modeling in a ribbed duct for the internal cooling of turbine blades," *International Journal of Heat and Fluid Flow* 26.1, pp. 92-104.

37. Rau, G., Cakan, M., Moeller, D., and Arts, T., 1998, "The effect of periodic ribs on the local aerodynamic and heat transfer performance of a straight cooling channel," *Journal of Turbomachinery*, 120(April), pp. 386–375.

38. Watanabe, Kazunori, and Toshihiko Takahashi, 2002, "LES simulation and experimental measurement of fully developed ribbed channel flow and heat transfer," *ASME Turbo Expo 2002: Power for Land, Sea, and Air*. American Society of Mechanical Engineers, No. GT-2002-30203.

39. Murata, Akira, and Sadanari Mochizuki, 2004, "Large eddy simulation of turbulent heat transfer in a rotating two-pass smooth square channel with sharp 180 turns," *International Journal of Heat and Mass Transfer* 47.4, pp. 683-698.

40. Sewall, Evan A., and Tafti, Danesh K., 2008, "Large eddy simulation of flow and heat transfer in the developing flow region of a rotating gas turbine blade internal cooling duct with coriolis and buoyancy forces," *Journal of Turbomachinery* 130.1, No. 011005.

41. Coletti, Filippo, Irene Cresci, and Tony Arts, 2012, "Time-Resolved PIV Measurements of Turbulent Flow in Rotating Rib-Roughened Channel With Coriolis and Buoyancy Forces," *ASME Turbo Expo 2012: Turbine Technical Conference and Exposition*. American Society of Mechanical Engineers, No. GT2012-69406.

42. Tabakoff, W., and Y. Sugiyama, 1980, "Experimental Methods of Determining Particle Restitution Coefficients.”," *On Polyphase Flow and Transport, ASME, Century*.

43. Walsh, W. S., K. A. Thole, and Chris Joe, 2006, "Effects of sand ingestion on the blockage of film-cooling holes." In *ASME Turbo Expo 2006: Power for Land, Sea, and Air*, pp. 81-90.

44. Crosby, J. M., Lewis, S., Bons, J. P., Ai, W., and Fletcher, T. H., 2007, "Effects of Particle Size, gas Temperature and Metal Temperature on High Pressure Turbine Deposition in Land Based Gas Turbines From Various Synfuels," *ASME Turbo Expo 2007: Power for Land, Sea, and Air*, No. GT2007-27531.

45. Bons, J. P., Crosby J., Wammack, J. E., Bently, B. I., and Fletcher, T. H., 2007, "High-Pressure Turbine Deposition in Land-Based Gas Turbines From Various Synfuels," *Journal of Engineering for Gas Turbines and Power* 129.1, pp. 135-143.

46. Wammack, J. E., Crosby, J., Fletcher, D., Bons, J. P., and Fletcher, T. H., 2008, "Evolution of Surface Deposits on a High-Pressure Turbine Blade—Part I: Physical Characteristics." *Journal of Turbomachinery* 130.2, No. 021020.

47. Bons, J. P., Wammack, J. E., Crosby, J., Fletcher, D., and Fletcher T. H., 2008, "Evolution of Surface Deposits on a High-Pressure Turbine Blade—Part II: Convective Heat Transfer," *Journal of Turbomachinery* 130.2, No. 021021.

48. Reagle, C. J., Delimont, J. M., Ng, W. F., Ekkad, S. V., and Rajendran, V. P., 2013, "Measuring the coefficient of restitution of high speed microparticle impacts using a PTV and CFD hybrid technique." *Measurement science and technology* 24.10, No. 105303.

49. Delimont, J. M., Murdock, M. K., Ng, W. F., and Ekkad, S. V., 2014, "Effect of Near Melting Temperatures on Microparticle Sand Rebound Characteristics at Constant Impact Velocity." *ASME Turbo Expo 2014: Turbine Technical Conference and Exposition*. American Society of Mechanical Engineers, No. GT2014-25686

50. Sreedharan, Sai Shrinivas, and Danesh K. Tafti, 2011, "Composition dependent model for the prediction of syngas ash deposition in turbine gas hotpath," *International Journal of Heat and Fluid Flow* 32.1, pp. 201-211.

51. Shrinivas, S. S., and Tafti D. K., 2013, "Effect of blowing ratio on early stage deposition of Syngas ash on a film cooled vane leading edge using large eddy simulations", *ASME J. Turbomachinery* 135(6), No. 061005

52. Ai, Weiguo, and Thomas H. Fletcher, 2012, "Computational analysis of conjugate heat transfer and particulate deposition on a high pressure turbine vane," *Journal of Turbomachinery* 134.4, No. 041020.

53. El-Batsh, Hesham, and Hermann Haselbacher, 2002, "Numerical investigation of the effect of ash particle deposition on the flow field through turbine cascades," In *ASME Turbo Expo 2002: Power for Land, Sea, and Air*, pp. 1035-1043.

54. Singh, Sukhjinder, and Danesh Tafti, 2015, "Prediction of Sand Deposition in a Two-Pass Internal Cooling Duct," *ASME Turbo Expo 2015: Turbine Technical Conference and Exposition*. American Society of Mechanical Engineers, No. GT2015-44103.

55. Singh, S. and Tafti, D. K., 2015 “Particle deposition model for particulate flows at high temperatures in gas turbine components,” *Int. J. Heat Fluid Flow* 52, pp. 72-83.

56. Singh, S. and Tafti, D. K., 2015 “Prediction of Sand Transport and Deposition in a Two-Pass Internal Cooling Duct,” ASME J. of Eng. For Gas Turbines and Power.

57. Yu, Kuahai, and Danesh Tafti, 2016, "Impact model for micrometer-sized sand particles." *Powder Technology* 294, pp.11-21.

58. Senior, C. L., and Srinivasachar, S., 1995, "Viscosity of Ash Particles in Combustion Systems for Prediction of Particle Sticking," Energ Fuel, 9(2), pp. 277-283.

59. Yin, C., Luo, Z., Ni, M., and Cen, K., 1998, "Predicting coal ash fusion temperature with a back-propagation neural network model," Fuel, 77(15), pp. 1777-1782.

60. Abdel-Wahab, Samer, 2003, "Large Eddy Simulation of Flow and Heat Transfer in a Staggered 45º Ribbed Duct and a Rotating 90º Ribbed Duct," PhD diss., Virginia Polytechnic Institute and State University.